

# The radio emitting X-ray binary systems LS 1+61°303 and Cygnus X-3

Marta Peracaula i Bosch

**ADVERTIMENT.** La consulta d'aquesta tesi queda condicionada a l'acceptació de les següents condicions d'ús: La difusió d'aquesta tesi per mitjà del servei TDX ([www.tesisenxarxa.net](http://www.tesisenxarxa.net)) ha estat autoritzada pels titulars dels drets de propietat intel·lectual únicament per a usos privats emmarcats en activitats d'investigació i docència. No s'autoritza la seva reproducció amb finalitats de lucre ni la seva difusió i posada a disposició des d'un lloc aliè al servei TDX. No s'autoritza la presentació del seu contingut en una finestra o marc aliè a TDX (framing). Aquesta reserva de drets afecta tant al resum de presentació de la tesi com als seus continguts. En la utilització o cita de parts de la tesi és obligat indicar el nom de la persona autora.

**ADVERTENCIA.** La consulta de esta tesis queda condicionada a la aceptación de las siguientes condiciones de uso: La difusión de esta tesis por medio del servicio TDR ([www.tesisenred.net](http://www.tesisenred.net)) ha sido autorizada por los titulares de los derechos de propiedad intelectual únicamente para usos privados enmarcados en actividades de investigación y docencia. No se autoriza su reproducción con finalidades de lucro ni su difusión y puesta a disposición desde un sitio ajeno al servicio TDR. No se autoriza la presentación de su contenido en una ventana o marco ajeno a TDR (framing). Esta reserva de derechos afecta tanto al resumen de presentación de la tesis como a sus contenidos. En la utilización o cita de partes de la tesis es obligado indicar el nombre de la persona autora.

**WARNING.** On having consulted this thesis you're accepting the following use conditions: Spreading this thesis by the TDX ([www.tesisenxarxa.net](http://www.tesisenxarxa.net)) service has been authorized by the titular of the intellectual property rights only for private uses placed in investigation and teaching activities. Reproduction with lucrative aims is not authorized neither its spreading and availability from a site foreign to the TDX service. Introducing its content in a window or frame foreign to the TDX service is not authorized (framing). This rights affect to the presentation summary of the thesis as well as to its contents. In the using or citation of parts of the thesis it's obliged to indicate the name of the author.



UNIVERSITAT DE BARCELONA



Departament d'Astronomia i Meteorologia

The Radio Emitting X-ray Binary Systems  
LS I+61°303 and Cygnus X-3

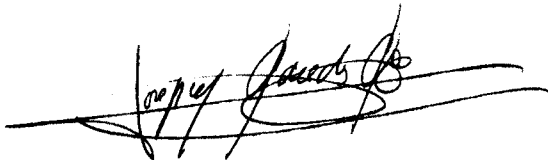
Memòria presentada per  
**Marta Peracaula i Bosch**  
per optar al grau de  
Doctora en Ciències Físiques  
Barcelona, juny del 1997





PROGRAMA DE DOCTORAT D'ASTRONOMIA I METEOROLOGIA  
BIENNI 1992-1994

Memòria presentada per Marta Peracaula i Bosch  
per optar al grau de Doctora en Ciències Físiques

A handwritten signature in black ink, appearing to read 'Josep Maria Paredes Poy', written over a horizontal line.

Josep Maria Paredes Poy  
Director de la tesi



Les estrelles binàries  
de raigs X amb emissió ràdio  
LS I+61°303 i Cygnus X-3

## RESUM

de la tesi presentada per Marta Peracaula i Bosch per a obtenir  
al grau de doctora en Ciències Físiques

### 1- Introducció

Les binàries o estrelles dobles físiques són sistemes formats per dues estrelles lligades gravitatòriament. Avui en dia sabem que aquest és un fenomen molt comú a la Galàxia, on aproximadament la meitat de les estrelles s'han format donant lloc a aquesta mena de sistemes. Històricament, el seu estudi ha proporcionat molta informació sobre la física estel·lar. Per exemple, fins no fa gaire els sistemes binaris eren la millor eina disponible per a la mesura directa de la massa dels estels. Ha estat també gràcies a observacions de sistemes binaris contenint púlsars que s'ha obtingut la verificació de previsions de la teoria de la Relativitat General.

Durant gran part de la seva vida, les components d'un sistema binari orbiten a distàncies comparativament més grans que les dimensions del volum on domina la influència gravitatòria de cadascuna de les components (lòbul de Roche). Durant aquest temps, les estrelles del sistema evolucionen de la mateixa manera que ho farien si es trobessin aïllades. No obstant, les diferents etapes de l'evolució estel·lar per les que, inexorablement, cadascuna de les components haurà de passar segons la seva massa, poden fer que els paràmetres físics del sistema (massa, radi, semieix de l'òrbita, vent estel·lar, etc.) variïn apreciablement. A conseqüència d'aquests canvis, es poden produir situacions en què el radi d'una de les components es faci comparable, o fins i tot l'excedeixi, al tamany característic del seu lòbul de Roche. A partir d'aquí, és possible que s'estableixi una transferència de massa entre les components del sistema. Altrament, aquesta transferència també poder ésser deguda al vent estel·lar. La captura o acreció d'una fracció d'aquesta massa, perduda per la component "donant", per part de la seva companya pot donar lloc a fenòmens capaços de modificar apreciablement les propietats globals del sistema, a l'hora que també pot generar un ampli ventall de fenòmens observacionals que es manifesten en gairebé tot l'espectre electromagnètic.

És molt variada la "fauna" de sistemes binaris interactuants segons sigui el mecanisme concret de transferència de massa i el tipus d'estrelles components. En aquest treball ens ocupem en particular de les anomenades **binàries de raigs X**, de les quals s'en coneixen actualment més d'un centenar. Entre elles, però, centrem la nostra atenció en les que, a més, han estat detectades en ones de ràdio, a les quals ens referirem simplement per brevetat com a ràdio binàries X. Aquesta subclasse de les binàries de raigs X, amb emissió ràdio associada, és certament força heterogènia i fins avui s'en coneixen de l'ordre de 20 casos. A títol d'exemple, aquests inclouen sistemes com Cygnus X-1, el primer candidat a forat negre, LS I+61°303 i Circinus X-1, les dues úniques ràdiofonts del cel clarament periòdiques a part dels púlsars, i Cygnus X-3, famosa per les seves erupcions ràdio on la lluminositat augmenta fins a tres ordres de magnitud en poc més d'un dia. L'interés astrofísic d'aquestes ràdio binàries X es podia entendre, fins no fa gaire, només en que molts dels processos físics que hi tenen lloc són versions a escala reduïda del que succeix en algunes galàxies actives i quàsars. Això ja és de per sí remarcable doncs, donat que totes elles són objectes pertanyents a la nostra Galàxia i per tant relativament propers, les tècniques observacionals de la Interferometria de Base Molt Llarga (*Very Long Baseline Interferometry* o VLBI) ens permeten assolir-hi unes resolucions espacials ( $\sim 1$  AU) impensables en una font extragalàctica. D'altra banda, les escales temporals

d'emissió en ràdio binàries són relativament curtes (mesos o dies) i, en ocasions, fins i tot periòdiques d'acord amb el període orbital del sistema. Això facilita enormement preveure les èpoques d'observació en que hom espera més activitat.

D'altra banda, aquest tipus d'objectes s'han beneficiat considerablement dels darrers avenços en les tècniques observacionals, tant des de terra com des de l'espai, que actualment fan possible realitzar observacions astronòmiques en tots els dominis de l'espectre electromagnètic. Això és particularment interessant quan s'aplica a astres que siguin detectables a la vegada en més d'un aquests dominis, com és el cas de les ràdio binàries X. Aleshores, les observacions multi-espectrals representen una eina molt important per a contrastar l'elaboració de models teòrics capaços de reproduir, de manera unificada, el comportament observat a longituds d'ona molt diferents (ràdio, infraroig, òptic, ultraviolat, raigs X i raigs Gamma).

Més recentment, però, s'hi ha afegit un nou punt d'interés després del descobriment de diverses fonts de raigs X durs ( $> 40$  keV) en la direcció del centre galàctic. Aquests nous objectes presenten una contrapartida ràdio constituïda per una font central compacta i variable de la qual emana un *jet* bipolar. La interpretació més probable és que es tracta de ràdio binàries X on la component compacta és un forat negre amb un disc d'acreció, perpendicularment al qual s'ejecta plasma altament relativista en forma de *jet* col·limat. Una d'elles, GRS1915+105, ha resultat ser la primera ràdiofont coneguda de la Galàxia que ejecta matèria a velocitats aparentment superlumíniques.

### Acreció i ejecció de matèria en binàries de raigs X

En general, les binàries de raigs X són sistemes formats per un estel normal i un objecte compacte i col·lapsat. Aquest darrer és habitualment un estel de neutrons però, en ocasions, pot tractar-se d'un forat negre. El nom de binàries de raigs X es justifica pels processos d'acreció de matèria sobre l'objecte compacte, els quals originen intenses emissions en aquest domini espectral. Segons la massa de l'estel normal, que actua com a donant de matèria, les binàries de raigs X es classifiquen a grans trets en d'alta massa ( $\gtrsim 10 M_{\odot}$ ) o de baixa massa ( $\lesssim 1 M_{\odot}$ ), sense que es coneguin exemples intermitjos. La component normal de les binàries massives

pertany típicament a tipus espectrals primerencs mentre que, en les poc massives, aquesta és de tipus espectral més tardà.

Suposem que la component compacta del sistema binari acreta matèria a un cert ritme  $\dot{M}_{\text{acc}}$ . Aleshores, la lluminositat del sistema  $L_{\text{acc}}$  es pot estimar suposant que tota l'energia cinètica del material acretat s'allibera en forma de radiació:

$$L_{\text{acc}} = \frac{GM_X \dot{M}_{\text{acc}}}{R_X} = 8.4 \times 10^{35} \text{ erg s}^{-1} \left[ \frac{M_X}{M_\odot} \right] \left[ \frac{\dot{M}_{\text{acc}}}{10^{-10} M_\odot} \right] \left[ \frac{R_X}{10 \text{ km}} \right]^{-1}, \quad (1)$$

on  $G$  és la constant de gravitació universal,  $M_X$  és la massa de l'estel compacte i  $R_X$  el seu radi. Una cota mínima a la temperatura d'aquesta radiació es pot estimar suposant que es comporta com un cos negre a temperatura  $T_{\text{bb}} = (L_{\text{acc}}/4\pi R_X^2 \sigma)^{1/4}$ . Per a un estel de neutrons típic, resulta  $T_{\text{bb}} \sim 10^7$  K i, per tant, la major part d'aquesta lluminositat serà emesa en la banda de raigs X d'energia  $\sim 1$  keV o superior.

A grans trets, són dos els mecanismes mitjançant els quals pot tenir lloc aquesta transferència de massa  $\dot{M}_{\text{acc}}$  entre estels. En primer lloc, hi tenim el mecanisme d'acreció per vent estel·lar. Aquest és particularment important en sistemes massius, sobre tot si la primària és un estel primerenc amb un elevat ritme de pèrdua de massa per vent estel·lar (fins a  $\dot{M}_w > 10^{-7} M_\odot \text{ any}^{-1}$  en algunes primàries del tipus espectral Be), del qual una fracció serà acretat per la secundària compacta. En segon lloc hi tenim el mecanisme d'acreció per desbordament del lòbul de Roche de la primària, més comú en les binàries poc massives.

El ritme d'acreció no pot ser, en principi, superior a l'anomenat límit d'Eddington, quan la força sobre el material acretat deguda a la pressió de la radiació emesa es fa superior a la pròpia atracció gravitatòria. Aquest límit ve donat per:

$$\dot{M}_{\text{Edd}} = \frac{4\pi m_p c R_X}{\sigma_T} = 1.5 \times 10^{-8} M_\odot \text{ yr}^{-1} \left[ \frac{R_X}{10 \text{ km}} \right], \quad (2)$$

on  $m_p$  és la massa del protó,  $c$  la velocitat de la llum i  $\sigma_T$  la secció eficaç de Thomson. A partir de l'Eq. (1) la lluminositat corresponent, anomenada Lluminositat d'Eddington, serà

$$L_{\text{Edd}} = \frac{4\pi G M_X m_p c}{\sigma_T} = 1.3 \times 10^{38} \text{ erg s}^{-1} \left[ \frac{M_X}{M_\odot} \right]. \quad (3)$$

Ocasionalment, per exemple durant el pas pel periastre en una òrbita excèntrica o si la primària pateix un episodi intens de pèrdua de massa, pot donar-se el cas que el límit d'Eddington sigui superat ( $\dot{M}_{\text{acc}} > \dot{M}_{\text{Edd}}$ ). Aleshores, el material que estava essent acretat es veu rebutjat violentament per la pressió de radiació dominant, produint-se una ona de xoc que s'expandeix a partir d'una regió central. Això pot provocar l'ejecció i posterior acceleració de partícules relativistes, amb generació de camp magnètics, de forma semblant a com té lloc en un xoc mòbil causat per una explosió de supernova. El núvol de plasma ejectat durant aquest fenomen eruptiu s'anomena habitualment plasmó. La radiació sincrotró dels seus electrons relativistes, sotmesos al camp magnètic del núvol, és la que dona lloc a les erupcions ràdio observades. En alguns casos, la presència i evolució del plasmó es pot seguir observacionalment mitjançant tècniques de VLBI. D'altra banda, els fotons estel·lars de l'estrella primària poden ser dispersats per efecte Compton invers amb aquests electrons relativistes, originant una emissió de raigs X i/o Gamma que s'afegeix a la produïda per acreció. Naturalment, poden existir altres mecanismes que comportin l'acceleració de partícules relativistes en una ràdio binària X, com ara l'acceleració dels electrons en la magnetosfera de l'estel compacte. En aquest sentit, alguns autors han proposat recentment escenaris on la creació del plasmó no té lloc com a conseqüència de l'acreció supercrítica, sino com a resultat d'una transició entre els diferents règims d'acreció de l'estel compacte.

## 2— Campanyes observacionals

Observacions fetes per altres autors de LS I+61°303 així com modelitzacions anteriors, indiquen la presència de radiació sincrotró de plasmó en expansió. Això va suggerir les bases teòriques del model a emprar així com altres observacions que s'havien de fer necessàriament per entendre millor el comportament de l'objecte. Per tant es van realitzar diferents sèries d'observacions per part de l'equip així com es van adquirir d'altres de bases de dades públiques.

Les diferents observacions que hem usat són:

- 1- *Observacions coordinades de raig-X i dues freqüències radio durant un cicle orbital de LS I+61°303*

Realitzades durant l'Agost-Setembre del 1992 mitjançant el satèl·lit ROSAT (raigs-X) i el *Very Large Array*, VLA (cm). Fins aquell moment hi havia molt poques observacions de la LS I+61°303 en raigs-X i cap d'elles havia estat mostrejada regularment durant un llarg període de temps. Per tant, l'observació durant un cicle complet en cm i raigs-X permetria investigar en major profunditat les propietats de la font en raig-X (especialment la possible existència de variabilitat) i la seva relació amb l'emissió ràdio.

- 2- *Observacions simultànies en ràdio i raigs- $\gamma$*

Obtingudes per Kniffen et al. el 1993 i 1994, i Tavani et al. (1996) el 1994 i 1995. Les vàrem utilitzar per a comprovar que el nostre model es consistent amb la relació de lluminositats entre l'emissió d'alta energia i la ràdio emissió.

- 3- *Observacions coordinades en mm, submm i cm*

Les prenguérem simultàniament amb el JCMT (mm i submm) i el VLA (cm) l'Octubre de 1994 amb el propòsit d'investigar la possible existència d'una caiguda espectral a altes freqüències, tal i com predèia el nostre model.

També duguérem a terme una campanya de l'Octubre de 1994 a l'Abril de 1995 de la font a cm -mitjançant l'antena de 70m en el MDSCC a Robledo de Chavela (Madrid)- i submm - amb l'observatori Nobeyama Millimeter Array (NMA) al Japó.

Juntament amb LS I+61°303 vam observar Cygnus X-3 i SS433 en totes dues sessions coordinades VLA-JCMT i Madrid-Nobeyama.

- 4- *Corbes de llum ràdio a diferents freqüències durant un cicle orbital de LS I+61°303*

Observacions simultànies a 6 diferents longituds d'ona centimètrica van ser fetes amb el VLA durant Juny-Juliol de 1994 (Paredes et al, 1996). Aquesta és l'observació amb el cobriment més ampli en freqüència fet mai d'una erupció



ràdio d'aquesta font i ens proporciona una informació sumament útil sobre el comportament de l'espectre ràdio.

5- *Diverses observacions de corbes de llum ràdio a una única longitud d'ona*

Tretes de la bibliografia, obtingudes per altres col.laboradors, i majorment obtingudes per nosaltres amb l'antena DSS63 al Space Communications Complex INTA-NASA (Madrid, Spain).

Aquest treball es basa en l'anàlisi de les observacions que acabem de presentar. Hem dividit la memòria del treball en **tres grans parts**. En la **primera part** s'inclouen els capítols en què hem desenvolupat **models teòrics** per a l'emissió ràdio i d'altres energies en aquests tipus de sistemes i els hem aplicat als resultats observacionals. En la **segona part** ens hem dedicat a obtenir **imatges de l'estructura ràdio** de les fonts observades a diferents escales espacials i a interpretar-ne els resultats. Finalment en la **tercera part** fem una anàlisi de la **variabilitat** d'aquestes fonts i una **búsqueda dels períodes** a diferents escales temporals que poden presentar. Tot seguit resumim els resultats obtinguts en cadascuna de les parts.



# PART I

## PROCESSOS ALTAMENT ENERGÈTICS EN RÀDIO BINÀRIES X

### 3- Modelització d'episodis eruptius en ràdio binàries X: aspectes ràdio, X, Gamma

La Física dels processos eruptius i d'acceleració de partícules relativistes en ràdio binàries X, que hem descrit qualitativament, és molt complexa i encara poc coneguda. No obstant això, en el seu estudi és particularment útil i fructífera la modelització de l'emissió ràdio associada. A partir d'unes hipòtesis relativament senzilles sobre la geometria i el camp magnètic, és possible determinar diversos paràmetres físics de la regió emissora, així com estimar l'eficiència dels processos d'acceleració pel que fa a la quantitat de partícules relativistes necessàries per explicar l'emissió ràdio observada. Tota aquesta informació pot servir com a punt de partida per a models més sofisticats.

Quan en una ràdio binària X té lloc un episodi d'ejecció d'un plasmó d'electrons relativistes, aquest dóna lloc a una erupció en el nivell d'emissió del sistema que és particularment notòria en les bandes ràdio, X i, fins i tot, Gamma. Com tot seguit es veurà, les corbes de llum observades a diferents longituds d'ona dependran de l'evolució temporal de la població d'electrons relativistes, així com dels paràmetres físics propis del plasmó.

#### Càlcul de corbes de llum ràdio

Considerem en principi que el núvol de plasma es pot aproximar per una esfera

homogènia de radi  $r$ , expandint-se a velocitat constant  $v$  a partir d'un radi inicial  $r_0$  segons

$$r = r_0 + vt. \quad (4)$$

Altres geometries més complexes, com cilíndrica o tipus jet, també poden ésser considerades, però el cas és que no canvien qualitativament la física del problema. El mateix succeeix quan hom considera el cas d'un plasmó inhomogeni. Pel que fa al camp magnètic, suposarem que el seu valor promig dins del plasmó és un cert  $B$  constant i que la seva variació temporal té lloc conservant el flux magnètic, de forma que  $B \propto r^{-2}$ .

Al llarg de l'expansió del plasmó, els mecanismes d'acceleració aniran injectant electrons relativistes dins aquest. A la vegada, aquests electrons estaran sotmesos a pèrdues energètiques per diferents processos. Per tant, la injecció contínua de partícules accelerades juntament amb el seu ritme de pèrdues energètiques determinaran, en cada instant, quina és la funció de distribució  $N(E, t)$  del plasmó. Aquesta funció és la que indica el nombre total d'electrons existents per interval unitat d'energia, i es pot obtenir resolent la següent equació de continuïtat:

$$\frac{\partial N(E, t)}{\partial t} + \frac{\partial}{\partial E} \left( N(E, t) \frac{dE}{dt} \right) = Q(E, t). \quad (5)$$

En l'entorn de les ràdio binàries X, l'expressió adequada de les pèrdues energètiques  $dE/dt$  és:

$$\frac{dE}{dt} = -\frac{v}{r} E - a_S B^2 E^2 - a_C U_R E^2, \quad (6)$$

on  $a_S$  i  $a_C$  són constants i  $U_R$  és la densitat d'energia dels fotons estel·lars a la posició del plasmó. En aquesta equació, el primer terme dona compte de les pèrdues per expansió del plasmó, considerada adiabàtica, el segon terme de les degudes a la radiació sincrotró i el tercer terme correspon a les causades per l'efecte Compton invers. Altres tipus de pèrdues, com ara la radiació lliure-lliure o les pèrdues per ionització no acostumen a ser rellevants en el cas que ens ocupa.

Tal com s'observa en l'espectre d'energia dels raigs còsmics, els mecanismes coneguts d'acceleració de partícules relativistes (de Fermi, per xocs, etc.) tendeixen a generar distribucions de tipus potencial ( $\propto E^{-p}$ ), amb un exponent proper a un cert valor universal  $p \simeq 2.5$ . Per tant, és raonable pendre un terme font  $Q(E, t)$ , representatiu dels electrons injectats per unitat de temps i d'energia, com una llei de potència del tipus

$$Q(E, t) = Q_0(t)E^{-p}, \quad (7)$$

on l'amplitud  $Q_0(t)$  i l'exponent  $p$  dependran de l'eficiència, a determinar, dels mecanismes d'acceleració.

La solució conjunta de les Eqs.(5) i (6), que en part s'ha de realitzar numèricament, permet conèixer en tot instant la funció de distribució  $N(E, t)$ . Amb aquesta funció es poden calcular els corresponents coeficients d'emissió  $\epsilon_\nu^S$  i absorció  $\kappa_\nu^S$  sincrotró a partir de les seves expressions standard (Pacholczyk, 1970), basades en la teoria de radiació de càrregues accelerades. Amb aquests coeficients podem passar a plantejar l'equació del transport radiatiu per a la intensitat específica  $I_\nu$

$$\frac{dI_\nu}{ds} = -\kappa_\nu^S I_\nu + \epsilon_\nu^S. \quad (8)$$

La seva solució, que sovint caldrà obtenir també numèricament, s'ha d'adaptar a la geometria del problema, esfèrica en el nostre cas. Un cop coneguda  $I_\nu$  per a totes les visuals corresponents als elements de superfície en que hom divideix el plasmó, la densitat de flux ràdio observada  $S_\nu$  s'obté per integració de la intensitat específica a tot l'angle sòlid del plasmó:

$$S_\nu(t) = \int_{\Omega_s} I_\nu d\Omega_s \quad (9)$$

Tot aquest procediment s'ha de dur a terme per a cada instant de temps i per a cada freqüència ràdio d'interés. D'aquesta manera es poden obtenir l'evolució temporal dels espectres i corbes de llum ràdio a comparar amb les observacions.

Mencionarem també que, si bé aquí ens hem ocupat de plasmons esfèrics, en altres objectes el plasma relativista pot ejectar-se contínuament i amb un cert grau de colimació, donant lloc a l'existència de ràdio jets. Aquesta situació pot donar-se quan es forma un disc d'acreció al voltant de la component compacta del sistema

binari. El plasma pot aleshores emanar en forma de jet en les dues direccions perpendiculars al disc. En aquesta situació, és necessari introduir alguns canvis pel que fa a la manera com varien magnituds físiques, com ara les dependències del camp magnètic i l'energia dels electrons relativistes. Un model de tipus jet ha estat aplicat per exemple al cas de Cygnus X-3 (Martí et al., 1992).

### Càlcul de corbes de llum X i Gamma

Són diferents mecanismes els que, actuant dins una ràdio binària X, poden contribuir a la seva corba de llum en el domini d'altres energies (X i/o Gamma). En primer lloc tenim la contribució deguda a l'acreció en sí, que ja hem estimat a partir de l'Eq. (1). No obstant, aquests fotons són emesos en regions molt properes a l'objecte compacte i, per tant, són susceptibles d'ésser reprocessats cap a energies més baixes abans d'abandonar definitivament el sistema, la qual cosa dificulta considerablement el càlcul. D'altra banda, segons Taylor et al. (1995) també és d'esperar en alguns casos emissió X per bremsstrahlung tèrmic en els xocs del vent estel·lar de la primària, causats per l'expansió del plasmó relativista. Finalment, un altra possibilitat és l'emissió de fotons d'alta energia per efecte Compton invers dels fotons òptics estel·lars sobre els electrons relativistes.

En aquest apartat concentrarem la nostra atenció en l'estimació de la lluminositat  $L_{IC}$  esperada per efecte Compton invers, doncs aquest mecanisme és particularment eficient en les binàries massives, com les que modelarem més endavant, en les quals la primària té una lluminositat de fotons òptics i ultraviolats molt elevada. D'aquesta manera i simultàniament amb el càlcul de l'apartat anterior, la lluminositat  $L_{IC}$  vindrà donada per la integració del terme de pèrdues Compton de la Eq.(6) a tota la funció de distribució  $N(E, t)$ :

$$L_{IC}(t) = \frac{a_C U_{R0} t_0}{\rho^2} \int E^2 N(E, t) dE \quad (10)$$

Els fotons deguts a l'efecte Compton invers poden arribar a tenir una energia fins a  $4\gamma^2$  vegades més elevada que la dels fotons estel·lars òptics originals, on  $\gamma$  és l'energia dels electrons relativistes en unitats de  $m_e c^2$ . Així doncs si, per exemple,

l'estel primari irradia el plasmò amb fotons de  $\sim 10$  eV i desitgem obtenir raigs Gamma de  $\sim 100$  MeV, ens caldran electrons relativistes amb  $\gamma \sim 10^3$ , corresponent a energies de  $\sim 10^{-3}$  erg.

Un altre conseqüència important de les pèrdues per efecte Compton invers pot ser l'existència un tall en les altes freqüències de l'espectre ràdio de la binària. Això es deu al fet que, durant les primers etapes de l'expansió del plasmó, els electrons relativistes es generen a una distància relativament curta de la primària i, per tant, estaran sotmesos a un intens camp de radiació que fa que les pèrdues Compton siguin fortament dominants. Seguint el raonament de Taylor et al. (1995), la densitat d'energia d'aquesta radiació es pot estimar aproximadament com

$$U_{R0} = \frac{L_*}{4\pi r_0^2 c}, \quad (11)$$

éssent  $L_*$  la lluminositat de l'estel primari del sistema. Això implica que el temps de vida de l'electró en front de pèrdues Compton pot escriure's com:

$$t_{IC} \equiv \frac{E}{(dE/dt)_{IC}} = \frac{4\pi r_0^2 c}{a_C L_* E}. \quad (12)$$

Per tant, només si la velocitat d'expansió del plasmó es tal que  $v > r_0/t_{IC}$ , l'electró conseguirà abandonar les proximitats de la primària abans de perdre tota la seva energia, éssent possible que després encara pugui emetre fotons ràdio sincrotró. Això ens introdueix una energia límit  $E_b$  per sobre de la qual els electrons relativistes no contribuiran apreciablement a l'emissió ràdio. Aquest límit ve donat per

$$E_b = \frac{4\pi c v r_0}{a_C L_*}. \quad (13)$$

La seva existència permet entendre per què l'emissió en dominis espectrals tant separats com ràdio i X o Gamma pot estar íntimament relacionada. D'altra banda, donat que l'emissió sincrotró d'un electró amb energia  $E$  és important al voltant de l'anomenada freqüència crítica  $\nu_c \propto BE^2$ , l'existència d'un tall en la distribució d'energies dels electrons, a causa de les pèrdues Compton, implica a més que l'espectre ràdio de la binària ha de presentar també un tall a la freqüència corresponent a aque-

sta energia.

## Models ajustats

Hem calculat l'emissió ràdio d'origen sincrotró amb un model que considera un núvol esfèric de partícules relativistes expandint-se adiabàticament amb velocitat uniforme. Les partícules són injectades de manera contínua durant un període finit de temps amb una distribució d'energia amb llei de potència. Juntament a les pèrdues d'energia sincrotró i adiabàtica de les partícules relativistes, hem considerat les pèrdues produïdes per scattering Compton invers en la proximitat de l'estrella primària. Com que les pèrdues d'energia degudes al scattering Compton invers d'un electró depenen directament del quadrat de la seva energia, la presència d'aquest procés porta a un ràpid canvi del pendent de l'espectre ràdio per sobre d'una determinada freqüència. Aquesta freqüència de canvi de pendent depèn fortament de la proximitat de l'estrella primària i del tamany de la regió emissora, i per tant, la determinació d'aquesta freqüència o un límit inferior d'ella pot servir per restringir les dimensions i posició del plasmó.

En la figura 3.7, presentem el model ajustat a l'espectre determinat amb les observacions del VLA i JCMT obtingudes a l'octubre de 1994. Els paràmetres usats per fer el càlcul han estat trets d'anteriors modelitzacions d'aquestes fonts així com d'algunes propietats conegudes (Paredes et al. 1991, Taylor et al. 1992, Seaquist et al. 1982, Martí 1993). Les observacions ràdio van estar realitzades al voltant de la fase 0.8. La fase corresponent al pic de l'erupció està situada d'una manera general entre les fases 0.4 a 0.9 (Paredes et al. 1990). Per tant, l'època en que s'ha ajustat l'espectre ha estat al voltant del pic d'emissió. El tamany de la regió és aproximadament 2.2 AU pel primer dia i al voltant de 2.6 AU pel segon.



# PART II

## IMATGES RÀDIO

### 4- Imatges de LS I+61°303 a escala de mil.lèssimes de segon d'arc

De les observacions de VLBI (interferometria de molt llarga base) realitzades el 8 de juny de 1992 i els dies 9 i 13 de setembre de 1993 cal remarcar tres resultats importants:

a) En dues ocasions totalment independents, s'han obtingut evidències observacionals de velocitats d'expansió  $\sim 0.01c-0.1c$ . Aquests valors són més petits però comparables als observats a partir de mesures ràdio d'altres binàries de raigs X (i normalment relacionats amb velocitats d'expansió o ejecció de plasmons) tals com SS433 i Cyg X-3. A més a més, aquests valors són aproximadament un o dos ordres de magnitud superiors als obtinguts per Taylor et al. (1992) i Massi et al. (1993) durant episodis d'emissió molt intensa en LS I+61°303. Una possible explicació d'aquesta diferència pot venir donada pel fet que aquests autors van usar arguments indirectes per fer les seves estimacions de velocitat, assumint que el material que ells observaven havia estat ejeccat uns quants dies abans. Assumien ells també que l'expansió havia mantingut una velocitat constant durant aquests dies. Per tant, les baixes velocitats que ells obtenien podrien ser un promig d'unes velocitats inicialment més altes que disminuïen posteriorment, de manera similar al comportament de les petites erupcions que ja hem estudiat aquí. També és possible que el material observat per ells estigués associat amb ejeccions d'erupcions més petites que tingueren lloc després de les dates que ells van estimar com a inici de l'erupció principal.

Les velocitats d'expansió de  $3000 \text{ km s}^{-1}$  i  $18000 \text{ km s}^{-1}$  mesurades directament a partir de les nostres observacions de VLBI són consistents amb el model d'acreció supercrítica proposat per Taylor & Gregory, el qual prediu que els electrons han de

more's enfora del sistema amb velocitats superiors a  $1000 \text{ km s}^{-1}$  per tal d'evitar les pèrdues catastròfiques per Compton invers dels fotons òptics provinent de la propera primària.

b) En les observacions en que LS I+61°303 estava en un estat quiescent o quasi, hi ha al voltant de 10 a 15 mJy no localitzats en escales de mil·lèsimes de segon d'arc però que apareixen en escales intermitges entre les observades pel interferòmetre VLB (pocs mas) i el VLA ( $\sim 0.1''$ ). Per tant, aixó representa una evidència indirecta de estructura ràdio al nivell menor o igual de  $0.1''$ . Creiem que observacions de LS I+61°303 amb un instrument amb aquesta resolució (exemple, MERLIN) són necessaries per observar d'una manera directa aquesta estructura.

Per contra, durant la sessió activa (primera part de Run II) tota l'emissió detectada a escales VLBI semblava coincidir amb la densitat de flux mesurada pels instruments de baixa resolució VLA i antena d'Effelsberg.

c) La detecció d'emissió ràdio en fulguracions (flaring) compactes en LS I+61°303 en èpoques en que de manera clara no es troba prop d'un pic intens d'emissió indica que entre erupcions l'emissió ràdio d'aquesta font pot tenir un origen diferent que quan hi ha les grans erupcions, és a dir, l'emissió quiescent ràdio de LS I+61°303 pot no està relacionada d'una manera senzilla amb el decaïment lent de la radiació de les grans erupcions. Aixó és consistent amb un escenari en què les fulguracions ràdio entre erupcions estan associades amb el solapament de sèries de petits acon-teixements.

D'altra banda, a partir de la forma de la corba observada al Run II a la fase 0.66, sospitem que durant l'estat actiu estavem observant una altra de les mini-fulguracions que es superposen al perfil de les corbes de llum ràdio de LS I+61°303. Si és aquest el cas, no hem detectat velocitats d'expansió que poguessin ser associades a mini-fulguracions particulars. Hem vist, per contra, que durant la mini-fulguració observada en l'estat quiescent del Run II s'ha observat una ràpida velocitat (0.06c). Aquesta comparació podria indicar que la velocitat estructural observada durant aquesta mini-erupció del Run II no està associada al mateix fet que causa la fulguració ràpida, i que possiblement la velocitat obtinguda a partir dels cinc sectors de dades del 8 de juny de 1992 és deguda a haver observat una part de la baixada d'emissió d'una erupció intensa o potser el principi d'una altra. Per tant, pensem

que les velocitats altes no estan associades a mini-fulguracions en sí mateix sino a intenses erupcions ràdio periòdiques.

## 5— Búsqueda d'estructura extensa associada a LS I+61°303 a partir de dades VLA

Pel que fa a l'anàlisi de les imatges profundes obtingudes amb el VLA per tal d'estudiar la possible estructura extensa associada a LS I+61°303 cal dir que s'han obtinguts resultats interessants. L'anàlisi de varies sessions d'observació amb el VLA han mostrat diversos grumolls d'emissió ràdio extensa en una zona de pocs minuts d'arc al voltant de LS I+61°303. Entre aquestes fonts extenses, l'única que podria estar associada físicament a LS I+61°303 és la que apareix amb la lletra D a la figura 6.3. De tota manera, l'associació és dubtosa, però les dades que disposem fins ara tampoc permeten rebutjar aquesta associació d'una manera clara. La interpretació més factible és que totes aquestes estructures corresponen a emissió lliure-lliure de radiofonts associades bàsicament a les regions HII veïnes. Aixó implica que cap estructura ràdio extensa o tipus jet, en l'escala del minut d'arc, és present al voltant de LS I+61°303 almenys fins a un valor límit de brillantor de  $0.43 \mu\text{Jy}/\text{segon d'arc}$  al quadrat. A partir de dades del VLA en configuració A, un límit superior similar de  $0.9 \text{ mJy}/\text{segon d'arc}$  al quadrat ha estat obtingut per estructures ràdio extenses en escales angulars de segon d'arc.

La falta aparent d'estructures ràdio extenses en LS I+61°303 podria tenir dues explicacions completament diferents. La primera seria que jets i ràdio emissió extensa existeixen en LS I+61°303 però estan per sota del nivell de detecció o s'extenen en escales angulars encara no explorades. La segona seria que el mecanisme d'erupció de LS I+61°303 és tal que l'emissió ràdio està restringida prop del sistema binari i l'ejecció dels electrons ràdio emissors fora del volum orbital no és rellevant. L'obtenció de mapes amb molta sensibilitat amb resolució intermitja entre VLA i VLBI (exemple, MERLIN) ajudaria a aclarir la situació. De fet, les observacions VLBI de LS I+61°303 (Cap. 4) suggereixen que al voltant del 20 per cent de la densitat de flux total no esta continguda en estructures de mil.lèssimes de segon d'arc. Per tant, és bastant factible que aquesta densitat de flux desapareguda estigui

distribuida en escales menors o similars a 0'1, encara per explorar.

Com un sub-producte de les nostres observacions, hem detectat també 9 ràdio fonts compactes desconegudes fins ara en el camp de LS I+61°303 amb densitats de flux a 6 cm entre 0.2-1.2 mJy. Una d'elles sembla ser la contrapartida ràdio de l'estrella SAO12383, mentre que les altres probablement són objectes extragalàctics.

## 6— Emissió extensa en Cygnus X-3

També hem estudiat l'emissió extensa de Cyg X-3. El mapa que hem obtingut està representat a la figura 7.3. És significatiu que l'angle de posició ( $35^\circ$ ) dels jets aparents és molt semblant al que formen les estructures allargassades que es veuen als mapes de VLBI obtinguts recentment per Schalinski et al. (1995). També cal indicar que l'angle de posició és quasi el mateix que apareix al mapa fet amb MERLIN per Newell et al. (1997) i que mostra molt clarament una component extensa a escala de sub-segon d'arc. Aquestes coincidències donen suport a la nostra detecció, suggerint que els jets ràdio del nostre mapa i els de Strom et al. (1989) poden ser una manifestació directa de l'acumulació de partícules energètiques produïdes per l'activitat eruptiva de l'objecte central. L'angle d'obertura de 10 graus estimat a partir de la figura 7.3 indicaria que l'amplària dels lòbuls ràdio de Cyg X-3 no estaria provocada per un feix intrínsecament ample. L'alternativa seria un feix estret que canvia sovint la seva direcció, tal com s'ha observat a SS433, encara que és difícil reconciliar-ho amb el relativament estret rang d'angles de posició vistos en VLBI i MERLIN.

En qualsevol cas, que sobre això s'haurà de tornar a parlar una vegada s'hagi confirmat els jets ràdio de segons d'arc amb una millor relació senyal-soroll.

# PART III

## ESTUDI DE VARIACIONS I BÚSQUEDA DE PERIODICITATS

### 7— Variabilitat ràdio a curt termini en LS I+61°303

A la figura 10.1 es pot veure que la densitat de flux de LS I+61°303 canvia de manera clara durant escales de temps al voltant de 1 h o menys. Per tal de veure si aquestes petites fulguracions presenten periodicitat, hem tret el comportament general de les dades restant a cada punt el promig de la densitat de flux dels punts propers dins d'una finestra d'una hora de longitud. La corba de llum ràdio resultant es mostra a la figura 10.2. Aquí la presència de les microfulguracions és més evident. La seva amplitud és de 4 mJy, equivalent al 4 per cent de la densitat de flux total.

Hem usat la corba de llum ràdio rectificada per fer la búsqueda de períodes en el rang d'un minut a poques hores. Els mètodes emprats en aquesta búsqueda són CLEAN, PDM i autocorrelació. A partir dels periodogrames obtinguts, mostrats a la figura 10.3, podem veure que tots tres mètodes indiquen la presència d'un possible període de 1.4 hores. A la figura 10.4 presentem la corba de llum ràdio promig obtinguda plegant totes les dades amb el període de 1.4 hores. L'amplitud promig de la micro-fulguració és 2 mJy.

Com a resultat d'aquesta anàlisi pensem que hem detectat microfulguracions ràdio amb una amplitud de  $\sim 4$  mJy i un període de  $\sim 1.4$  hores en LS I+61°303.

### 8— Búsqueda de periodicitat raig X en LS I+61°303

La variabilitat en raigs X observada per ROSAT en una escala temporal d'alguns dies suggeriria d'una manera clara la possibilitat que LS I+61°303 presentés erupcions

periòdiques en raig X connectades amb l'emissió ràdio. A fi d'estudiar aquesta possibilitat, es va fer ús de les dades subministrades per l'instrument All Sky Monitor (ASM) a bord del satèl·lit Rossi X-Ray Timing Explorer (RXTE). Les dades ASM de LS I+61°303 inclouen 10 mesos d'observació diària.

Es van utilitzar per fer l'anàlisi de periodicitats els mètodes PDM i CLEAN. A la figura 11.1, mostrem el resultat obtingut al aplicar PDM en el rang 5–45 dies. El mínim més significatiu correspon al període de 26.7 dies, amb un error estimat de 0.2 dies. Aquest resultat es confirma de manera independent emprant CLEAN, la qual cosa dóna fiabilitat al valor obtingut.

Cal remarcar que el període de raigs X de 26.7 dies que hem trobat és consistent amb el període ràdio de 26.71 dies que hem determinat al capítol 8. També el període de raig X que hem trobat aquí és consistent, tenint en compte els errors, amb el període ràdio de 26.496 dies determinat per Taylor & Gregory (1984). No queda clar a hores d'ara si les darreres determinacions del període ràdio i de raig X de 26.7 dies representa un augment real del període lligat al període orbital.

La corba de llum de raig-X, posada en fase i promitjada a intervals de 0.1 fase, està representada a la figura 11.2. També s'ha representat, a efectes de comparació, una corba ràdio promig. La forma de la corba de raig-X és diferent de la que presenta la de ràdio. La de raig-X presenta un estat actiu més extens i la part de més emissió es solapa amb les fases de més emissió ràdio. Aquest fet es pot interpretar com efecte Compton invers, el qual sembla jugar un paper important en la producció de raig-X.

## 9— Búsqueda de periodicitat ràdio en Cygnus X-3

És coneguda la variació periòdica de l'emissió de raigs X de Cyg X-3 de 4.8 hores. Sembla ser que una periodicitat similar s'ha trobat per altres autors a la banda ràdio, encara que no ha estat confirmat. A fi d'estudiar la possible periodicitat de Cyg X-3 a escala d'hores, vam desenvolupar un programa observacional amb l'antena de 70 m de Madrid Deep Space Communication Complex (INTA-NASA) a 3.6 cm. Es van

realitzar un total de 16 sessions d'observació. Els resultats observacionals obtinguts es mostren a les figures 12.1 i 12.2. L'error estimat de cada punt és menor del 10 per cent.

Per determinar alguna possible periodicitat s'ha emprat els mètodes CLEAN i PDM. En tots dos mètodes s'obté un període de 21 hora. Els periodogrames corresponents a CLEAN i PDM estan representats a la figura 12.3 i 12.4 respectivament. En aquestes figures també és evident el primer harmònic (10.5 hores).

En la figura 12.5 es mostra la corba de llum ràdio obtinguda després de posar en fase totes les dades amb període 20.9 hores. La fase zero s'ha triat de manera que correspongui al mínim que s'observa en la corba de raig X. A aquestes dades s'ha ajustat per mínims quadrats una funció senoidal més una constant. La representació de la corba ajustada també es mostra a la figura 12.5. Tal com es pot veure a les figures 12.3 i 12.4, no s'ha trobat cap període significatiu en el rang 4.8-5.1 h, i per tant no es pot confirmar el període de 4.8 h suggerit per Molnar et al. (1984).

L'anàlisi de les nostres dades sembla indicar que les fulguracions ràdio de baixa intensitat, amb una durada de poques hores, estan afectades per una modulació de 20.9 hores amb una amplitud de  $\sim 120$  mJy. Aquest període de 21 hora requereix més observacions per la seva confirmació.





# Index

<b>1</b>	<b>General introduction</b>	<b>1</b>
1.1	Introduction to Radio Emitting X-Ray Binary Systems . . . . .	1
1.2	Objectives . . . . .	3

**PART I**  
**HIGHLY ENERGETIC PROCESSES**  
**IN REXRB EMISSION**

<b>2</b>	<b>Modeling the Radio and X-ray Emission of REXRBs</b>	<b>11</b>
2.1	Introduction to the Synchrotron Radiation . . . . .	11
2.2	Total energy losses . . . . .	13
2.3	Application to a group of relativistic particles . . . . .	18
2.3.1	Solution of the homogeneous continuity equation . . . . .	22
2.3.2	Particular solution of the continuity equation . . . . .	26
2.3.3	Source Function: case of an spherical plasmon . . . . .	29
2.4	Applications to a source in a REXRB scenario . . . . .	32

<b>3</b>	<b>LS I+61°303 as a radio, X-ray and <math>\gamma</math>-ray source</b>	<b>49</b>
3.1	Introduction . . . . .	49
3.2	Simultaneous Radio and X-ray observations . . . . .	51
3.2.1	Radio Observations . . . . .	51
3.2.2	X-ray Observations . . . . .	52
3.2.3	Analysis: Radio versus X-ray Variations . . . . .	55
3.2.4	Model fits of the radio light curves . . . . .	57
3.2.5	Inverse-Compton Emission . . . . .	58
3.3	Multiwavelength centimetric observations . . . . .	60
3.4	Simultaneous cm-mm observations . . . . .	61

## PART II

### RADIO IMAGES

<b>4</b>	<b>Imaging the milli-arcsecond radio structure of LS I+61°303</b>	<b>67</b>
4.1	Introduction . . . . .	67
4.2	Observations . . . . .	69
4.3	A mini-flare structural evolution: <i>Run I</i> results . . . . .	71
4.3.1	<i>Run I</i> data analysis . . . . .	71
4.3.2	Rapid expansion during the mini-outburst . . . . .	78
4.3.3	The flux on intermediate scales . . . . .	80
4.3.4	Discussion: single or double structure? . . . . .	81

---

4.4	Outburst decay structural evolution: <i>Run II</i> results . . . . .	85
4.4.1	<i>Run II</i> data analysis . . . . .	85
4.4.2	Discussion: Expansion velocity during the decay of a radio outburst . . . . .	90
4.5	Conclusions from <i>Run I</i> and <i>Run II</i> results . . . . .	91
<b>5</b>	<b>Search for LS I+61°303 associated extended radio emission</b>	<b>97</b>
5.1	Introduction . . . . .	97
5.2	VLA observations . . . . .	98
5.3	Search for arcsecond extended radio emission . . . . .	101
5.4	Search for arcminute extended radio emission . . . . .	103
5.4.1	Deep images performance . . . . .	103
5.4.2	Arcminute extended radio sources in the field . . . . .	104
5.4.3	The nature of the extended radio sources detected . . . . .	105
5.4.4	Long temporal structural stability . . . . .	107
5.5	Spectral index analysis . . . . .	109
5.6	Other compact radio sources in the LS I+61°303 vicinity . . . . .	111
5.7	Extended radio emission from independent low resolution data . . . . .	112
5.8	Conclusions . . . . .	113
<b>6</b>	<b>Extended emission in Cygnus X-3</b>	<b>117</b>
6.1	Introduction . . . . .	117
6.1.1	Cygnus X-3 sub-arcsecond radio emission . . . . .	117

6.1.2	Cygnus X-3 arcsecond radio emission . . . . .	118
6.1.3	Objectives . . . . .	119
6.2	VLA observations and results . . . . .	120
6.3	Discussion . . . . .	120

### PART III

## SEARCH FOR PERIODIC BEHAVIOUR IN THE RADIO AND X-RAY LIGHT CURVES

<b>7</b>	<b>Brief introduction to periodicity analysis methods</b>	<b>129</b>
7.1	Fourier Analysis . . . . .	130
7.2	CLEAN algorithm . . . . .	132
7.3	Phase dispersion minimization method . . . . .	133
7.4	Period improving from cross correlation in the phase space . . . . .	135
<b>8</b>	<b>The LS I+61°303 periodic strong radio outbursts</b>	<b>139</b>
8.1	Introduction . . . . .	139
8.2	Periodicity analysis of the LS I+61°303 radio outburst . . . . .	144
<b>9</b>	<b>Short term radio variability of LS I+61°303</b>	<b>149</b>
9.1	Introduction . . . . .	149
9.2	Observations and data reduction . . . . .	150
9.3	Micro-flares variability analysis results . . . . .	151

---

9.4 Discussion of micro-flares . . . . .	155
<b>10 Search for X-ray periodicity in LS I+61°303</b>	<b>161</b>
10.1 Introduction . . . . .	161
10.2 X-ray period search using ASM/RXTE data . . . . .	162
10.3 Discussion . . . . .	164
10.4 Conclusions . . . . .	167
<b>11 Search for radio periodicity in Cygnus X-3</b>	<b>171</b>
11.1 Introduction . . . . .	171
11.2 Observations . . . . .	173
11.3 Data reduction . . . . .	174
11.3.1 CLEAN algorithm . . . . .	174
11.3.2 Phase dispersion minimization method . . . . .	175
11.4 Results . . . . .	176



# Chapter 1

## General introduction

### 1.1 Introduction to Radio Emitting X-Ray Binary Systems

A stellar X-ray binary system is composed by a compact object and a non-degenerated star gravitationally attached to each other. The compact object (either a black hole or a neutron star) is accreting matter from the companion (usually a star in the main sequence).

Up to this moment, about 200 X-ray binary systems have been detected by means of various X-ray and optical surveys. They are known to be among the brightest sources of X-ray photons seen the sky, and such release of energy is directly related to the mass transfer process going on in the system. About a 10% of the gravitational energy of the flowing material is converted in X-ray luminosity. Processes, like the interaction of the transferred particles with the compact object magnetic field, heating and viscosity effects in the accretion disk, thermonuclear flashes, instabilities in the flow, etc, can give rise to large amounts of high energy photons.

The emission properties of a particular X-ray binary are basically determined by the spectral type of the massdonating star, the mass of the compact object and the geometry of the flow.

X-ray binary systems have been classified into the following two basic categories,

depending on the mass of the non-degenerated (or companion) star:

- low-mass X-ray binaries (LMXBs): The companion star belongs to the older type stellar population, later than type A, and it can even be a very evolved object like a white dwarf. Its mass is near or lower than  $1 M_{\odot}$ . The evolution of this star has drove it to the point where its external atmosphere layers have grown to fill its Roche lobe and it is transferring material, through the inner Lagrangian point, into the gravitational potential well of the compact object. Because of the angular momentum of the transferred material, the particles cannot fall straight onto the primary, but go into an orbit around it, forming in this way an *accretion disk* where high energy radiation is released from. Orbital periods are known for 26 LMXBs. Examples of LMXBs are Scorpius X-1 and Hercules X-1.
- High Mass X-ray Binaries (HMXBs): The companion is a main sequence early-type (OB) star. These are massive objects ( $M \gtrsim 10 M_{\odot}$ ) with strong mass losses through powerful stellar winds that provide the material transferred onto the compact star in the systems. They are found in the plane of the galaxy and associated with spiral arms –characteristic of young stars and early-type associations–. The UV and optical luminosity of the early type star is usually greater than that of the X-ray source.

Some of the material transferred can also travel to the compact object via Roche lobe overflow, as it is the case of the so called standard HMXBs, in which the spectral type of the companion is B2 or earlier. Regular X-ray eclipses are seen in them, showing orbital periods in the range from 2 to 10 days.

Another important subclass of HMXBs are those which the companion happens to be a rapidly rotating  $B_e$  star with an associated circumstellar envelope, being that the source of the material transferred. The absence of X-ray eclipses in these systems indicates the companion underfills its Roche lobe. Examples of HMXBs are LS I+61°303, Cygnus X-3, Centaurus X-3 and Cygnus X-1.

From the about 200 hundred X-ray binary systems known up to this moment, about 25 have been detected to emit in radio wavelengths. We have particularised our



research to these subclass, which are referred as **radio emitting X-ray binaries**, and shortened as **REXRBs**.

The fact that this subclass of X-ray binaries displays non-thermal radio emission means that a mechanism for accelerating relativistic particles is working in the system. Such particles radiate synchrotron emission, through radiowavelengths, when interacting with the compact object magnetic field.

Part of the astrophysical interest of REXRBs lies in the fact that they are galactic examples of high energy processes going on in accretion disk environments. Few of them have been observed to eject material, to expand at relativistic velocities or to display radio jets with similar characteristics to those seen in quasars and active galaxies (like, for example, superluminal motions). As in the extragalactic sources, the engine driving the jets in REXRBs are supposed to be extremely compact objects interacting with accreted material. Therefore, they can be considered galactic scale examples of extragalactic relativistic jet-like objects. One of the advantages of this is that, on the contrary to the extragalactic case, the proximity of REXRBs allows to achieve high spatial resolutions when studying their morphology with interferometric techniques. In addition, in the temporal scale of structural and luminosity variations are much shorter than the extragalactic homology. We can say that things happen in REXRBs environments at an ‘almost human’ time scale. The similarity of their powering devices with those of quasars and active galaxies is reaching such acceptance levels by the radioastronomy community, that the term ‘**galactic micro-quasars**’, seldomly used four years ago when the author started this work, is now commonly mentioned when referring to some known REXRBs.

## 1.2 Objectives

The purpose of this work has been the study of Radio Emitting X-Ray Binaries (**REXRBs**) both from the observational and theoretical approaches.

We have mainly concentrated in the analysis of their properties inferred from their emission in **radio** and **X-ray** wavelengths. Our observational contribution has been done specially at different centimetric and millimetric wavelengths, although contrast with other bands of the electromagnetic spectrum has been always considered.

From the about 25 REXRBs detected, we have directly observed and analyzed the sources LS I+61°303 and Cygnus X-3, both radiostars known for they highly variable radio emission events.

The most remarkable characteristic of LS I+61°303 is the recurrent display of radio outbursts that show complex light curve profiles with a period similar to 26.5 days. It is noticeable that, with the exception of pulsars, LS I+61°303 and Circinus X-1, are the only two known periodic radio sources. Cygnus X-3 is also well known for the exhibition of strong radio flares. The system spends most of the time in quiescent state, at a level of few hundreds of mJy. It normally exhibits variability in time scales of hours suspected of having periodical or quasi periodical trends. When an outburst occurs the source reaches peak flux densities of tens of Jy at centimetric wavelengths, which converts it during some days in one of the brightest radio source of the sky. Cygnus X-3 strong flares are irregularly spaced with a mean recurrence interval of  $\sim 120$  days.

The flaring events are believed to involve the ejection and acceleration of ionized plasma clouds (plasmons) responsible for the radio emission via synchrotron radiation.

The reasons for selecting this two sources as the objects to use in our study are mainly related to their flaring behaviour, and they can be summarized in the following points:

- Due to their outbursting properties they are intrinsically interesting as independent sources among the REXRBs.
- The sudden release of relativistic particles that provokes the flaring radio emission can help to better understand the origin of such particles and conditions of the system at the epochs of the outburst occurrence. That can be extrapolated to non-flaring radio emitters.
- In concrete, the periodical behaviour of LS I+61°303 (the only REXRB of such characteristic in the northern hemisphere) allows to predict the phases when the source is in active state. Such predictability facilitates the scheduling of observations, depending on whether we are interested to perform the experiment in quiescence or in active state. It also permits to coordinate different instruments for multiple energy band monitoring of the source, normally preferred when it is in a high emission state.

- The periodical behaviour itself is also very interesting. It is presumably related to the orbital motion of the system, and onset of outburst are suspected to occur near the periastron passage. Such behaviour can indicate a very eccentric orbit for the binary system LS I+61°303. The confirmation of such issues can provide clues for physical parameters also for more steady radio emitting REXRBs, as well as for non radio emitting X-ray binaries.
- The observation of the temporal and spectral evolution of a radio flaring event, as well as the source structure at different spatial scales during it, can provide us with useful information of the mass of the particles involved, the energetic evolution of such radiating particles, the velocities acquired by the possible radio emitting bulk and its expansion rates, and the scenario in which the source is embedded (geometry and strength of the magnetic field, surrounding non relativistic material, etc).
- And finally, the study of these two objects is a continuation of the work performed by members of the research group where the author is integrated. They disposed of previous observations of these objects, as well as experience in radio single dish, and array observations and wide knowledge of this REXRBs and the different physical models that could describe them.

This report is structured in 11 chapters, being the bulk of them (with the exception of the present one) distributed in three main differentiated parts. Each part is a compilation of the work performed to study the next different aspects of REXRBs and in particular of our selected objects:

**Part I – Highly energetic processes in REXRBs emission:** In **Chapter 2** we develop a theoretical model of the radio and X-ray emission arisen from a plasmon of relativistic particles within a REXRB scenario. In **Chapter 3** we apply this model to observations of LS I+61°303 and Cygnus X-3.

**Part II – Radio images:** We analyze sub-arcsecond, arcsecond and arcminute images we have performed from different observation campaigns of LS I+61°303 and Cygnus X-3. They are described in **Chapters 4, 5 and 6**.

**Part III – Search for periodic behaviour in the radio and X-ray light curves:** After a brief description of statistical methods to look for a periodic signal from a data set, in **Chapter 7** we apply them to analyze the long and short time

scales of the variable behaviour of the target sources. **Chapter 8** is devoted to look for the instabilities in the  $\sim 26.5$  days radio period of LS I+61°303, and **Chapter 9** to analyze its 'micro-flares' repetitive behaviour at certain phases. **Chapter 10** is as well devoted to periodicities of LS I+61°303, but in this case in the X-ray domain, and, finally, **Chapter 11** analyzes the hour scale fluctuations observed in Cygnus X-3.

# Bibliografy

- [1] “Exploring the X-ray Universe”, 1995, Charles P.A., Seward F.D., Cambridge University Press
- [2] Martí J., 1993, “Radio emitting X-ray binaries”. PhD Thesis. Universitat de Barcelona.
- [3] Mirabel I.F., Rodríguez L.F., 1994, Nat 371, 46
- [4] “Relativistic jets from galactic sources”, 1997, Spencer R.E., Newell S.J. (eds) (Vistas in Astronomy Vol. 41, No 1)
- [5] Seaquist E.R., “Radio emission from stars”, 1993, in Rep. Prog. Phys. 56, 1145
- [6] “X-ray binaries”, 1995, Lewin, W.H.G., Van Paradijs J., Van den Heuvel E. (eds). Cambridge University Press



Part I  
HIGHLY ENERGETIC PROCESSES  
IN REXRB EMISSION





## Chapter 2

# Modeling the Radio and X-ray Emission of REXRBs

### 2.1 Introduction to the Synchrotron Radiation

The motion of a relativistic charged particle through a magnetic field  $\vec{\mathcal{B}}$  and an electrostatic field  $\vec{\mathcal{E}}$  can be described by the Lorentz equations of relativistic dynamics:

$$\frac{d}{dt}[\gamma m \vec{v}] = \frac{q}{c} \vec{v} \wedge \vec{\mathcal{B}} + q \vec{\mathcal{E}} \quad (2.1.1)$$

$$\frac{d}{dt}[\gamma m c^2] = q \vec{v} \cdot \vec{\mathcal{E}} \quad (2.1.2)$$

where  $c$  is the speed of the electromagnetic waves in a vacuum.  $m$ , the particle's mass,  $q$  the particle's electrical charge,  $\vec{v}$ , its velocity, and  $\gamma$  is defined as

$$\begin{aligned} \gamma &= \frac{1}{\sqrt{1 - \beta^2}} \\ \beta &= \frac{v}{c}. \end{aligned} \quad (2.1.3)$$

Therefore, the particle's energy is  $E = \gamma m c^2$ .

For a null electric field  $\vec{\mathcal{E}}$ , we can infer, from (2.1.2), that the modulus of the velocity is constant, and from (2.1.1) we see that the particle follows a helicoidal path (hence, it has angular acceleration) with the axis parallel to the magnetic field  $\vec{\mathcal{B}}$  and a velocity  $v \sin \theta$  (where  $\theta$  is the angle defined by  $\vec{v}$  and  $\vec{\mathcal{B}}$ ).

According to Maxwell's electromagnetism equations, a moving, accelerated, electrical charge creates electric and magnetic radiation fields which can be described by the Lienard-Wiechert potentials (particular solutions of Maxwell's equations). Developing these equations (done for example in Westfold 1959 and Pacholczyk 1970) it can be demonstrated that these fields create a Poynting vector –and therefore *an energy flux from the particle*–, in the same direction as  $\vec{v}$ . Another consequence is that the closer  $v$  is to  $c$ , the closer to  $\psi \simeq 2/\gamma$  (i.e. narrower) is the beam through which this radiation is emitted. Since the angle  $\psi$  is centered in the direction of the particle's instantaneous velocity, at relativistic velocities the direction in which the major part of the energy is emitted coincides with the direction of  $\vec{v}$ .

Developing the expression of the total power emitted by the particle in Fourier series of monochromatic waves (with  $\omega = 2\pi\nu$ ), the radiated power per unit frequency can be written as

$$p_\nu = \frac{\sqrt{3}q^3}{mc^2} \mathcal{B} \sin \theta F\left(\frac{\nu}{\nu_c}\right) \quad (2.1.4)$$

where

$$\nu_c = c_1 \mathcal{B} \sin \theta E^2; \quad c_1 = \frac{3q}{4\pi m^3 c^5} \quad (2.1.5)$$

$$F(x) = x \int_x^\infty K_{5/3}(z) dz; \quad (K_{5/3} \text{ Bessel Function}) \quad (2.1.6)$$

$F(x)$  has a maximum at  $x = 0.29$  and it can be seen, from its shape, that most of the energy is radiated around the so-called characteristic, or critical, frequency  $\nu_c$  defined in (2.1.5).

Let's examine the typical wavelengths corresponding to  $\nu_c$  for synchrotron emission from X-Ray Binary Systems:

If, for example, the particle is a relativistic electron with  $\gamma = 10$  and the magnetic field at a reasonable distance from the compact object's surface, is  $\mathcal{B} = 1G$ , from the first relation of (2.1.5) we obtain  $\nu_c = 5$  GHz. This means the electron energy will be released basically in the radio band frequencies.

As we will see later,  $\nu_c$  plays an important role in our radio emission model since

we use it as an observable to relate the maximum frequency at which a signal is detected to the electron energy distribution function and, therefore, to the parameters describing the physics of the sources.

The total power radiated by the particle is given by integrating over all frequencies the expression  $p_\nu$  in (2.1.4):

$$\left[ \frac{dE}{dt} \right]_{\text{sync}} = \int_0^\infty p_\nu d\nu = c_2 \mathcal{B}^2 \sin^2 \theta E^2 \quad (2.1.7)$$

where  $c_2 = \frac{2q^4}{3m^4 c^7}$ .

Equation (2.1.7) tells us that, for a single particle, the energy loss due to synchrotron emission is directly proportional to the square of its energy and to the square of the magnetic field in which it is embedded. Consequently, the more energetic the particle is the larger is its energy loss and the shorter its “lifetime” as a relativistic radiating body. The losses are also inversely proportional to the fourth power of the particle mass, so the lighter it is the greater the power it emits. Since the synchrotron radiation emitted by protons and other nuclei with electrical charge  $Z$  is a factor  $(m_p/Zm_e)^4 \simeq 10^9 - 10^{13}$  smaller than that emitted by electrons, from now on when we refer to a cloud of relativistic matter in a magnetic field, we will use the terms “particles” and “electrons” interchangeably when referring to synchrotron emitters.

## 2.2 Total energy losses of a relativistic electron in a REXRB scenario.

We must now consider the scenario where the relativistic electrons are in an environment relevant to this work. For the REXRBs the synchrotron emission is thought to come from a cloud of relativistic electrons (called also ‘plasmon’) embedded in a magnetic field and expanding adiabatically at a constant velocity  $v_{exp}$ . The electrons can be affected by the ambient radiation field originating from the primary star and also by the synchrotron emission itself. The interaction of these photons with the electrons is mainly due to the inverse Compton effect, i.e. the dispersion or scatter-

ing of a photon by the particle in which the first gains energy and the second loses it. Therefore, in this scenario the energy losses of an electron will be due to not only synchrotron emission but also to its inverse Compton losses and to the adiabatic expansion of the plasmon. This total energy decay can be expressed in the following simple form:

$$\left[ \frac{dE}{dt} \right]_{Tot} = \left[ \frac{dE}{dt} \right]_{Sync} + \left[ \frac{dE}{dt} \right]_{IC} + \left[ \frac{dE}{dt} \right]_{Ad}. \quad (2.2.1)$$

Let's analyze each term of the previous equation:

a) Synchrotron term:

We know from (2.1.7) that the synchrotron contribution to (2.2.1) depends on the square of the magnetic field. To obtain the time dependence of  $\mathcal{B}$ , a conservation law of the magnetic flux through the surface of the region (i.e.  $\vec{\mathcal{B}} \cdot \vec{\mathcal{S}} = constant$ ) is assumed. Then, considering a spherical region with radius  $\mathcal{R}(t)$ , the magnetic field decreases as  $\mathcal{R}(t)^{-2}$ :

$$\mathcal{B} = \mathcal{B}_0 \frac{\mathcal{R}_0^2}{\mathcal{R}(t)^2}. \quad (2.2.2)$$

By definition  $\mathcal{B}_0$  and  $\mathcal{R}_0$  are respectively the magnetic field and the radius of the region at a certain time  $t_0$ . This expression represents the progressive weakening of the magnetic field as the cloud expands.

Consequently, the synchrotron losses (2.1.7) can be expressed as a function of the radius of the plasmon;

$$\left[ \frac{dE}{dt} \right]_{Sync} = -a_s \mathcal{B}_0^2 \frac{\mathcal{R}_0^4}{\mathcal{R}(t)^4} E^2. \quad (2.2.3)$$

Taking as  $\sin^2\theta$  its mean value  $\langle \sin^2\theta \rangle = 2/3$  (an approximation that will be valid when we deal with a distribution of many particles), and since we are assuming that the particle is an electron  $m = m_e$ ,  $q = e$  then,  $a_s = 1.58 \cdot 10^{-3} \text{ erg}^{-1} \text{ gauss}^{-2}$ .

b) Inverse Compton term:

The inverse Compton variations also depend on the square of the particle's energy as described by the relation (Pacholczyk 1970):

$$\left[ \frac{dE}{dt} \right]_{IC} = -a_c u_{rad} E^2 \quad (2.2.4)$$

where, taking c.g.s. units,  $a_c = 3.97 \cdot 10^{-2} \text{ cm}^3 \text{ s}^{-1} \text{ erg}^{-2}$ .

For the moment we will only take into account the inverse Compton scattering due to the interaction of the electrons with the ultraviolet photons coming from the primary. We can add the effect of the self-inverse Compton scattering later on in the radiative transport equation.

If  $L_{uv}$  is the total ultraviolet luminosity of the primary star, the radiation field at a distance  $x$  from the primary can be well approximated by the expression:

$$u_{rad} = \frac{L_{uv}}{4\pi c x^2} \quad (2.2.5)$$

where the factor  $x^2$  accounts for the geometrical dilution of the radiation field.

Therefore,

$$\left[ \frac{dE}{dt} \right]_{IC} = -a_c \frac{L_{uv}}{4\pi c} \frac{E^2}{x^2} \quad (2.2.6)$$

In the expression for inverse Compton losses, the geometry of the plasmon will play an important role through the distribution of the distances  $x$  of the group of particles from the primary.

c) Adiabatic expansion term:

The rapid expansion velocities sometimes seen or derived for the radio counterparts of REXRBs also lead to important losses of kinetic energy of the particles. Assuming this expansion is an adiabatic process (there is no heat exchange with the surrounding medium, normally considered to be a vacuum), then, according to the second law of thermodynamics we have:

$$dE = -PdV \quad (2.2.7)$$

where  $dE$  is the internal energy variation of the source,  $P$  is the internal pressure and  $dV$  is the volume variation. Since we are considering a relativistic gas  $P$  is given by:

$$P = \frac{1}{3} \frac{E}{V} \quad (2.2.8)$$

In our case we assume that the emitting region is spherically symmetrical, hence the integrated volume will be  $V = \frac{4}{3}\pi\mathcal{R}^3$ . Differentiating and substituting in (2.2.8), the relation  $dE = -\frac{E}{\mathcal{R}}d\mathcal{R}$  is found. With this geometry the uniform expansion velocity is  $v_{exp} = \frac{d\mathcal{R}}{dt}$  and hence, from derivation with respect time, the energy losses due to adiabatic expansion can be expressed as:

$$\left[\frac{dE}{dt}\right]_{Ad} = -\frac{v_{exp}}{\mathcal{R}(t)} E. \quad (2.2.9)$$

Therefore, the decrease of energy of a particle due to the adiabatic expansion is directly proportional to its total energy.

We can conclude that the energy losses due to each of the three effects considered are closely related to the geometry of the particle region through its size  $\mathcal{R}(t)$  and the distribution of the particles with respect to the primary position  $x$ . Furthermore, for all the mechanisms, the decay is highly dependent on the energy of the electrons, and the magnitude of its losses grows with it. The extremely energetic particles will have a much more rapid evolution than the ones with lower energy. This fact will be reflected in the emission frequencies (since the characteristic frequency is proportional to the energy to the square). Therefore, we should be able to calculate the period of time for which we can detect emission at a given radio frequency from a distribution of relativistic particles, and at what rate the relativistic electrons need to be supplied in the REXRB vicinity to be consistent with the observed facts.

The time dependence for the terms forming  $\left[\frac{dE}{dt}\right]_{Tot}$  appears in  $\mathcal{R}(t)$  and indirectly (because of the change in the position of the particle with time) in  $x$ . Since the expansion is uniform the size of the spherical region can be expressed in the form:

$$\mathcal{R} = \mathcal{R}_0 + v_{exp} t. \quad (2.2.10)$$

For simplicity, it is advisable to express the radius  $\mathcal{R}(t)$  in units of  $\mathcal{R}_0$ . Thus, from now on the size of the region will be described using the variable  $\rho(t)$  defined as:

$$\rho = \frac{\mathcal{R}(t)}{\mathcal{R}_0}, \quad (2.2.11)$$

or equivalently:

$$\rho = 1 + \frac{t}{t_0}, \quad (2.2.12)$$

with

$$t_0 = \frac{\mathcal{R}_0}{v_{exp}}; \quad (2.2.13)$$

which is known as the *characteristic time of the expansion* since it coincides with the time that it takes for the source to double its radius.

Then,  $\left[\frac{dE}{dt}\right]_{Tot} = \frac{1}{t_0} \left[\frac{dE}{d\rho}\right]$ , and using the relations (2.2.2)–(2.2.13):

$$\left[\frac{dE}{d\rho}\right] = -\frac{E}{\rho} - a_s \mathcal{B}_0^2 t_0 \rho^{-4} E^2 - a_c \frac{L_{uv}}{4\pi c} t_0 x^{-2} E^2. \quad (2.2.14)$$

For simplicity we define:

$$\begin{aligned} C_s &= a_s \mathcal{B}_0^2, \\ C_c &= a_c \frac{L_{uv}}{4\pi c}. \end{aligned} \quad (2.2.15)$$

Therefore, the energy losses of a relativistic particle at a position  $x$  from the primary at the instant  $t$  is expressed as:

$$\left[\frac{dE}{d\rho}\right] = -\frac{E}{\rho} - C_s t_0 \frac{E^2}{\rho^4} - C_c t_0 \frac{E^2}{x^2} \quad (2.2.16)$$

$$\left[\frac{dE}{dt}\right]_{Tot} = \frac{1}{t_0} \left[\frac{dE}{d\rho}\right]$$

## 2.3 Application to a group of relativistic particles within an expanding plasmon

Now that we know the energy losses for a single electron we need to find the global losses for a group of particles with a certain distribution in energy and position in space. Specifically, we are dealing with an spherical plasmon that is expanding uniformly.

Figure (2.1) shows the geometric approach we have adopted for our particular model, where:

- $\mathcal{R}(\rho)$  is the radius of the plasmon at a normalized instant  $\rho$ ,
- $P$  is the position of the primary object,
- $S$  is the separation from  $P$  of the center of the plasmon  $C$ ,
- $x$  is the distance from  $P$  of an electron within the plasmon. In equation (2.2.16) we have seen that, at a given instant, the losses of the particles that are located at the same distance  $x$  from the primary depend only on their energy. Therefore, for our geometrical treatment of the problem, we divide the plasmon in ‘spherical zones’ each of them defined by the intersection between the plasmon and a ‘spherical shell’ of radius  $x$  centered in  $P$  (see figure 2.1). From now on, we will call such ‘spherical zones’ ‘shells’.
- $dx$  the thickness of the shells,
- $dV(x)$  is the volume of a shell  $x$ . Its expression has two different forms depending whether it is an ‘open shell’ or a ‘closed shell’. An ‘open shell’ is such that the loci of the points with the same  $x$  define an arch smaller than  $360^\circ$ . In contrast, the points forming a ‘closed shell’ define a circumference. When  $R(t) < S$  all the shells are open, whereas for  $R(t) > S$  both kind of shells are found (see Figure 2.1).



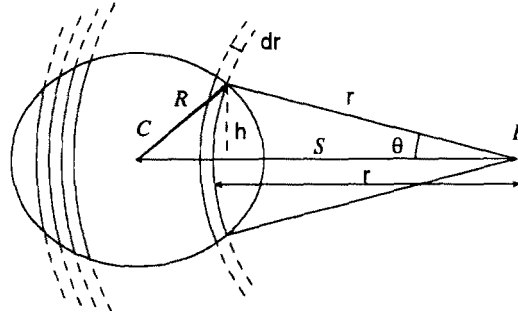


Figure 2.1: Division of the plasmon into spherical shells centered on the primary source

Therefore, the volume of a shell will be:

$$dV = \begin{cases} \pi \frac{x}{S} [\mathcal{R}^2 - (S - x)^2] dx & \text{open shells, i.e. } \begin{cases} \mathcal{R} < S \\ \text{or} \\ \begin{pmatrix} \mathcal{R} > S \\ \text{and} \\ x > \mathcal{R} - S \end{pmatrix} \end{cases} \\ 4 \pi x^2 dx & \text{closed shells, i.e. } \begin{cases} \mathcal{R} > S \\ \text{and} \\ x < \mathcal{R} - S \end{cases} \end{cases} \quad (2.3.1)$$

In order to simplify the problem of new shells appearing while the plasmon expands we 'normalize' the quantities  $\mathcal{R}(\rho)$ ,  $S$ ,  $x$  and  $dx$  by dividing them by  $\mathcal{R}(\rho)$ . We define the corresponding variables as

$$\left\{ \begin{array}{l} r \equiv \frac{x}{\mathcal{R}(\rho)} \\ dr \equiv \frac{dx}{\mathcal{R}(\rho)} \\ \sigma \equiv \frac{S}{\mathcal{R}(\rho)} \end{array} \right. \quad (2.3.2)$$

Thus, in this way, the geometry of the problem shown in Figure 2.1 is equivalent to a plasmon of a constant radius of value 1 and with a constant number of shells. Hereafter, when mentioning ‘shells’, ‘volume of a shell’, etc, we refer to the ‘normalized variables’ (2.3.2), unless another use is specified.

To indicate the volume  $dV$  of a shell  $r$ , we use the expression  $\mathcal{V}(\sigma, r) dr$ . Therefore, we have:

$$\begin{array}{l} \mathcal{V}(\sigma, r) dr = \pi \frac{r}{\sigma} [1 - (\sigma - r)^2] dr \quad \text{open shells, i.e.} \left\{ \begin{array}{l} 1 < \sigma \\ \text{or} \\ \left( \begin{array}{l} 1 > \sigma \\ \text{and} \\ r > 1 - \sigma \end{array} \right) \end{array} \right. \\ \\ \mathcal{V}(\sigma, r) dr = 4 \pi r^2 dr \quad \text{closed shells, i.e.} \left\{ \begin{array}{l} 1 > \sigma \\ \text{and} \\ r < 1 - \sigma \end{array} \right. \end{array} \quad (2.3.3)$$

Using definitions (2.3.2), the expression of the global losses (2.2.16) is equivalent to:

$$\boxed{\begin{array}{l} \left[ \frac{dE}{d\rho} \right] = -\frac{E}{\rho} - C_s t_0 \frac{E^2}{\rho^4} - \frac{1}{\mathcal{R}_0^2} C_c t_0 \frac{E^2}{\rho^2} \frac{1}{r^2} \quad (2.3.4) \\ \left[ \frac{dE}{dt} \right]_{Tot} = \frac{1}{t_0} \left[ \frac{dE}{d\rho} \right] \end{array}}$$

Relation (2.3.4) is a Bernoulli differential equation whose solution is:

$$E(\rho) = \frac{E_i \frac{\rho_i}{\rho}}{1 + \left[ \frac{C_s t_0}{4 \rho_i^3} \left( 1 - \left( \frac{\rho_i}{\rho} \right)^4 \right) - \frac{C_c t_0}{\mathcal{R}_0 r_i S} \left( 1 - \frac{\rho_i r_i}{\rho r} - \frac{r_i}{\sigma_i} \ln \frac{r_i}{r} \right) \right]} E_i \quad (2.3.5)$$

If in addition the plasmon is separated from the primary, i.e. there is an ejection such that

$$S = S_0 + v_{ej} t \quad (2.3.6)$$

then we find:

$$E(\rho) = \frac{E_i \frac{\rho_i}{\rho}}{1 + \left[ \frac{C_s t_0}{4 \rho_i^3} \left( 1 - \left( \frac{\rho_i}{\rho} \right)^4 \right) - \frac{C_c t_0}{\mathcal{R}_0^2 (\sigma_{00} - v_f)} \frac{1}{r_i} \left( 1 - \frac{\rho_i r_i}{\rho r} - \frac{r_i}{\sigma_{ii}} \ln \frac{r_i}{r} \right) \right]} E_i \quad (2.3.7)$$

where

$$\begin{aligned} \sigma_{00} &\equiv \frac{S_0}{\mathcal{R}_0}; & v_f &\equiv \frac{v_{ej}}{v_{exp}} \\ \sigma_{ii} &\equiv \frac{\sigma_{00} - v_f}{\rho_i} \end{aligned}$$

After having expressed the energy losses of a single particle according to the geometry of the cloud where all the particles are distributed, we can look for the global energy losses of the whole plasmon.

We define the **distribution function**,  $\mathcal{N}(t, r, E) dE dr$ , as the number of electrons with energy between  $E$  and  $E + dE$  within a shell of thickness  $dr$  at a distance  $r$  from the primary. To determine the global energy losses of the whole cloud we must integrate  $\left\{ \frac{dE}{dt} \mathcal{N}(t, r, E) dE dr \right\}$  over all the electron energies in each shell and over all the shells.

Therefore, to find the losses<sup>a</sup>

$$L_{Tot}(t) = \int_{Sph} \left[ \int_{E_l(r)}^{E_u(r)} \left[ \frac{dE}{dt} \right]_{Tot} \mathcal{N}(t, r, E) dE \right] dr \quad (2.3.8)$$

we need to know  $\mathcal{N}(t, r, E)$  –or  $\mathcal{N}(\rho, r, E)$  if we use  $\frac{1}{t_0} \frac{dE}{dt} \mathcal{N}(\rho, r, E) dE dr$ .

Since the flux of particles through a shell must be conserved, the distribution function has to satisfy the *continuity equation*

$$\frac{\partial \mathcal{N}(\rho, r, E)}{\partial \rho} + \frac{\partial}{\partial E} \left( \mathcal{N}(\rho, r, E) \frac{dE}{d\rho} \right) = \mathcal{Q}(\rho, r, E). \quad (2.3.9)$$

or equivalently:

$$\frac{\partial \mathcal{N}(\rho, r, E)}{\partial \rho} + \frac{\partial \mathcal{N}(\rho, r, E)}{\partial E} \frac{dE}{d\rho} + \mathcal{N}(\rho, r, E) \frac{\partial}{\partial E} \left( \frac{dE}{d\rho} \right) = \mathcal{Q}(\rho, r, E), \quad (2.3.10)$$

where we define  $\mathcal{Q}(\rho, r, E)$  as the number of particles injected per unit time with energies within the range  $(E, E + dE)$  in the shell limited by  $(r, r + dr)$ . We will call  $\mathcal{Q}(\rho, r, E)$  the *source function* of the shell  $r$ .

Since the solution of a lineal differential equation like (2.3.10) is the sum of the homogeneous solution (i.e. null source function) and a particular one, we can express it as

$$\mathcal{N}(\rho, r, E) = \mathcal{N}_H(\rho, r, E) + \mathcal{N}_P(\rho, r, E) \quad (2.3.11)$$

and look for the solution of each term.

### 2.3.1 Solution of the homogeneous continuity equation

In the case of the homogeneous solution, the first term of the sum in (2.3.11) has to satisfy:

---

<sup>a</sup>The subindex *Sph* in the first integral refers to the integration over the shells of the spherical plasmon. Normally the upper limit is  $(1 + \sigma)$ , whereas the lower limit is either  $(1 - \sigma)$  or  $(\sigma - 1)$  depending on the size of the plasmon  $R$  with respect to  $S$ .

$$\frac{\partial \mathcal{N}_H(\rho, r, E)}{\partial \rho} + \frac{\partial \mathcal{N}_H(\rho, r, E)}{\partial E} \frac{dE}{d\rho} + \mathcal{N}_H(\rho, r, E) \frac{\partial}{\partial E} \left( \frac{dE}{d\rho} \right) = 0. \quad (2.3.12)$$

To solve this equation we impose three conditions:

- 1) **We assume that the initial energy distribution follows a power-law with spectral index  $-p$ , and it does not depend on  $r$ .**

That is, when the particles were injected into the plasmon, at  $\rho = 1$ , the electron distribution was:

$$\mathcal{N}_H(1, r, E_1) dE_1 dr = \mathcal{N}_0(r) E_1^{-p} dE_1 dr. \quad (2.3.13)$$

where by definition  $E_1 \equiv E(\rho = 1)$ .

This assumption comes from empirical observation of high-energy cosmic-ray energy distributions, where the spectral index of the power-law is typically between 2 and 3 (Shu, 1991).

- 2) **When the particles were injected from outside into the plasmon they distributed uniformly over the volume of the whole sphere.**

Thus, the number of particles injected in each shell is proportional to its volume. Therefore, defining  $K$  as the proportionality constant and  $E_{lo}$ ,  $E_{uo}$  as the lower and upper limits of the electron energies injected, we have:

$$dr \left[ \int_{E_{lo}}^{E_{uo}} \mathcal{N}_H(1, r, E_1) dE_1 \right] = K \mathcal{V} \left( \frac{S}{\mathcal{R}_0}, r \right) dr, \quad (2.3.14)$$

and solving the integral after substituting equation (2.3.13) into it:

$$\mathcal{N}_0(r) dr \frac{E_{uo}^{1-p} - E_{lo}^{1-p}}{1-p} = K \mathcal{V} \left( \frac{S}{\mathcal{R}_0}, r \right) dr \quad (2.3.15)$$

thus,

$$\mathcal{N}_0(r) = K \frac{1-p}{E_{uo}^{1-p} - E_{lo}^{1-p}} \mathcal{V} \left( \frac{S}{\mathcal{R}_0}, r \right). \quad (2.3.16)$$

We define  $N_e$  as the total number of particles injected, which means,

$$N_e = \int_{Sph} \left[ \int_{E_{lo}}^{E_{uo}} \mathcal{N}_H(1, r, E_1) dE_1 \right] dr.$$

$$N_e = K \frac{1-p}{E_{uo}^{1-p} - E_{lo}^{1-p}} \int_{Sph} \mathcal{V}\left(\frac{S}{\mathcal{R}_0}, r\right) dr \int_{E_{lo}}^{E_{uo}} E_1^{-p} dE_1. \quad (2.3.17)$$

In condition 1) we have imposed that  $E_{lo}$  and  $E_{uo}$  do not depend on  $r$ . Thus, it is easily found that the solution of (2.3.17) is

$$\begin{aligned} N_e &= K \frac{4}{3} \pi, \\ K &= N_e \frac{3}{4\pi}. \end{aligned} \quad (2.3.18)$$

And substituting in (2.3.16) and in (2.3.13) we obtain:

$$\mathcal{N}_H(1, r, E_1) dE_1 dr = N_e \frac{3}{4\pi} \frac{1-p}{E_{uo}^{1-p} - E_{lo}^{1-p}} \mathcal{V}\left(\frac{S}{\mathcal{R}_0}, r\right) E_1^{-p} dE_1 dr. \quad (2.3.19)$$

The factors that do not depend on  $E_1$  and  $r$  can be included in a constant that we call  $K_0$ , thus:

$$\mathcal{N}_H(1, r, E_1) dE_1 dr = \mathcal{N}_0(r) E_1^{-p} dE_1 dr. \quad (2.3.20)$$

$$\mathcal{N}_0(r) = K_0 \mathcal{V}\left(\frac{S}{\mathcal{R}_0}, r\right) \quad (2.3.21)$$

$$K_0 = N_e \frac{3}{4\pi} \frac{1-p}{E_{uo}^{1-p} - E_{lo}^{1-p}} \quad (2.3.22)$$

- 3) As the plasmon expands, the number of particles in each shell will be constant in time and the same as when  $\rho = 1$ .**

Therefore, if we define  $N_e^r$  as the number of electrons in the shell  $r$ :

$$N_e^r = \int_{E_l(r)}^{E_u(r)} \mathcal{N}_H(\rho, r, E) dE = \int_{E_{lo}}^{E_{uo}} \mathcal{N}_H(1, r, E_1) dE_1. \quad (2.3.23)$$

This condition is satisfied if the shells  $dr$  are defined in such a way that the volume of each of them grows with time as the volume of the whole spherical plasmon does. We have made sure this condition is fulfilled when we have expressed the distribution equations as a function of the redefinition of a shell  $x$  by dividing its value by  $R(\rho)$  in equations (2.3.2).

The function  $E(E_1)$ , i.e. equation (2.3.7) for the particular case  $\rho = 1$ . has the form

$$E(E_1) = \frac{a E_1}{1 + b E_1} \quad (2.3.24)$$

where  $a = \frac{1}{\rho}$  and  $b = \frac{C_s t_0}{4} \left(1 - \left(\frac{1}{\rho}\right)^4\right) + \frac{1}{\mathcal{R}_0^2} \frac{C_c t_0}{2} \left(1 - \left(\frac{1}{\rho}\right)^2\right) \frac{1}{r^2}$ .

It can be seen that this is a monotonically increasing function, so one of its properties is that it is well behaved in the sense that the number of particles having energies between  $E_l(\rho, r)$  and  $E_u(\rho, r)$  is the same as the number of particles with energies between  $E_l(1)$  and  $E_u(1)$  (defined as  $E_{l_0}$  and  $E_{u_0}$ ). Moreover, this is satisfied for any energy beam we take, i.e., if  $E_1^k < E_1^m$  then  $E^k(\rho) < E^m(\rho)$  for any  $\rho$ , and the number of particles having energies between  $E^k(\rho)$  and  $E^m(\rho)$  will be the same as the number of particles that at  $\rho = 1$  had energies in the range  $E_1^k$  and  $E_1^m$  no matter how narrow the beam  $[E^m(\rho) - E^k(\rho)]$  is. This implies that expression (2.3.23) is equivalent to

$$\mathcal{N}_H(\rho, r, E) = \mathcal{N}_H(1, r, E_1) \frac{dE_1}{dE}. \quad (2.3.25)$$

Therefore, from conditions 1) and 2) we obtain the expression for  $\mathcal{N}_H(1, r, E_1)$  and from condition 3) we know the relation between it and  $\mathcal{N}_H(\rho, r, E)$ .

To obtain the general expression of the homogeneous distribution function we use (2.3.24) to express  $E_1$  and  $\frac{dE_1}{dE}$  in function of  $E$ , i.e.:

$$E_1 = \frac{E}{a - b E}, \quad (2.3.26)$$

$$\frac{dE_1}{dE} = \frac{a}{(a - b E)^2}. \quad (2.3.27)$$

Finally, substituting in (2.3.25) the expressions for  $\mathcal{N}_H(1, r, E_1)$  using (2.3.20), (2.3.26) and (2.3.27), we obtain:

$$\mathcal{N}_H(\rho, r, E) dE = \mathcal{N}_0(r) a(\rho) \frac{E^{-p}}{[a(\rho) - b(\rho, r) E]^{2-p}} dE. \quad (2.3.28)$$

Therefore, we can partially separate the dependence on  $r$  and on  $E$  of  $\mathcal{N}_H(\rho, r, E)$  by expressing it as the following product:

$$\mathcal{N}_H(\rho, r, E) dE d\rho dr = \mathcal{N}_0(r) E^{-p} \mathcal{G}(E, \rho, r) dE d\rho dr \quad (2.3.29)$$

where

$$\mathcal{N}_0(r) = N_e \frac{3}{4\pi} \frac{1-p}{E_{uo}^{1-p} - E_{lo}^{1-p}} \mathcal{V}\left(\frac{S}{\mathcal{R}_0}, r\right) \quad (2.3.30)$$

and

$$\mathcal{G}(E, \rho, r) = \frac{1/\rho}{\left\{ \frac{1}{\rho} - \left[ \frac{C_s t_0}{4} \left( 1 - \left( \frac{1}{\rho} \right)^4 \right) - \frac{C_c t_0}{\mathcal{R}_0^2 (\sigma_{00} - v_f)} \frac{1}{r_i} \left( 1 - \frac{1}{\rho} \frac{r_i}{r} - \frac{r_i}{\sigma_{ii}} \ln \frac{r_i}{r} \right) \right] E \right\}^{2-p}}. \quad (2.3.31)$$

We can demonstrate that  $\mathcal{N}_H(\rho, r, E)$  in (2.3.29) satisfies the Homogeneous Continuity Equation (2.3.12).

### 2.3.2 Particular solution of the continuity equation

As we mentioned before, to find the general solution of the continuity equation we need to add the solution for the homogeneous equation (2.3.12) and a particular solution  $\mathcal{N}_P(\rho, r, E)$  of (2.3.10), which satisfies:

$$\frac{\partial \mathcal{N}_P(\rho, r, E)}{\partial \rho} + \frac{\partial \mathcal{N}_P(\rho, r, E)}{\partial E} \frac{dE}{d\rho} + \mathcal{N}_P(\rho, r, E) \frac{\partial}{\partial E} \left( \frac{dE}{d\rho} \right) = \mathcal{Q}(\rho, r, E) \quad (2.3.32)$$

The source function  $\mathcal{Q}(\rho, r, E)$  of the shell  $r$  has been defined in section 2.3 as the number of particles with energies within the range  $(E, E + dE)$  injected per unit time  $\rho$  into the shell limited by  $(r, r + dr)$ .



This definition is equivalent to:

$$\frac{dN_s(\rho, r)}{d\rho} = \int_{E_l(\rho, r)}^{E_u(\rho, r)} \mathcal{Q}(\rho, r, E) dE dr, \quad (2.3.33)$$

where we call  $N_s(\rho, r)$  to the total number of particles in a shell  $r$  at an instant  $\rho$ .

If we define  $\rho_i$  as the instant when a particle  $i$  was injected into a shell  $r$ , and  $E_i$  was its energy at that time, then the total number of electrons injected into the shell between instant  $\rho_i = 1$  and instant  $\rho$  is:

$$\Delta N_s(\rho, r) = N_s(\rho, r) - N_s(1, r) = \int_{\rho_i=1}^{\rho_i=\rho} \left[ \int_{E_l(\rho_i, r)}^{E_u(\rho_i, r)} \mathcal{Q}(\rho_i, r, E_i) dE_i \right] d\rho_i dr, \quad (2.3.34)$$

which is equivalent to:

$$\begin{aligned} \int_{E_l(\rho, r)}^{E_u(\rho, r)} \mathcal{N}_P(\rho, r, E) dE dr = \\ \int_{E_l(1, r)}^{E_u(1, r)} \mathcal{N}_P(1, r, E_1) dE_1 dr + \int_{\rho_i=1}^{\rho_i=\rho} \left[ \int_{E_l(\rho_i, r)}^{E_u(\rho_i, r)} \mathcal{Q}(\rho_i, r, E_i) dE_i \right] d\rho_i dr. \end{aligned} \quad (2.3.35)$$

Since the number of particles in a shell  $r$  with energy between  $E$  and  $E + dE$  at instant  $\rho$  is the sum of the number of particles that were in that shell at the instant  $\rho = 1$ , and had energies in the corresponding unevolved range  $[E_1(E), E_1(E + dE)]$ , plus the particles that have been injected from instants  $\rho_i = 1$  to  $\rho_i = \rho$  also in the corresponding range of energies  $[E_i(E), E_i(E + dE)]$  at each time  $\rho_i$ , we can transform (2.3.35) to

$$\mathcal{N}_P(\rho, r, E) dE dr = \mathcal{N}_P(1, r, E_1) dE_1 dr + \int_{\rho_i=1}^{\rho_i=\rho} [\mathcal{Q}(\rho_i, r, E_i) dE_i] d\rho_i dr \quad (2.3.36)$$

with the condition that  $E(E_i)$  satisfies (2.3.5), so it is a monotonically increasing function thus, for the equality to be fulfilled, we have no need to integrate over the energies (as in the case of the homogeneous solution).

In order to express the relation between  $E$  and  $E_i$  more clearly we define the following variables:

$$\alpha = \frac{\rho_i}{\rho}, \quad (2.3.37)$$

$$\gamma = \frac{C_s t_0}{4\rho_i^3} (1 - \alpha^4) + \frac{1}{\mathcal{R}_0^2} \frac{C_c t_0}{2\rho_i} (1 - \alpha^2) \frac{1}{r^2}, \quad (2.3.38)$$

$$\beta = \alpha - \gamma E. \quad (2.3.39)$$

and thus, we can write

$$E(E_i) = \frac{\alpha E_i}{1 + \gamma E_i}, \quad (2.3.40)$$

$$E_i(E) = \frac{E}{\alpha - \gamma E} = \frac{E}{\beta}, \quad (2.3.41)$$

$$\frac{dE_i}{dE}(E) = \alpha \beta^{-2} \quad (2.3.42)$$

bearing in mind that  $\alpha$ ,  $\beta$  and  $\gamma$  depend on the variables  $\rho$ ,  $\rho_i$  and  $r$  (a part of depending on constant parameters of the system).

For the moment we will assume there were no particles in the plasmon before the injection started, in which case (2.3.36) is equivalent to

$$\mathcal{N}_P(\rho, r, E) dr = dr \int_{\rho_i=1}^{\rho_i=\rho} \left[ \mathcal{Q}(\rho_i, r, E_i) \frac{dE_i}{dE} \right] d\rho_i \quad (2.3.43)$$

and hence, a particular solution of the continuity equation can be expressed as:

$$\mathcal{N}_P(\rho, r, E) = \int_{\rho_i=1}^{\rho_i=\rho} \left[ \mathcal{Q}(\rho_i, r, E_i) \alpha \beta^{-2} \right] d\rho_i. \quad (2.3.44)$$

We can demonstrate that (2.3.44) satisfies the Particular Continuity Equation (2.3.32).

### 2.3.3 Source Function: case of an spherical plasmon

We now know that for any distribution like (2.3.44) the continuity equation is satisfied. Nevertheless, we need to find the form of the source function  $\mathcal{Q}(\rho, r, E)$  for the physics of our particular scenario. Analysis of the form of the appropriate source function will require some conditions consistent with our problem and with the conditions imposed to solve the homogeneous equation.

#### 1) Separability of $\mathcal{Q}(\rho, r, E)$

In section 2.3.1, we have imposed the condition that the shells  $dr$  be defined in such a way that they expand in time as the whole plasmon does. This condition implies that any variation of the particles in a shell will be due to “fresh” particles injected from outside the plasmon itself but not from particle flow coming from the neighboring shells.

A sensible first step is to separate  $\mathcal{Q}(\rho, r, E)$  into the product of two functions, one of which is independent on  $E$  since we want it to represent the uniform instantaneous distribution of the new particles over the whole volume at the instant they are injected, beyond their energy at that time. Therefore,

$$\mathcal{Q}(\rho, r, E) = \mathcal{Q}_1(E[\rho, r]) \mathcal{Q}_2(\rho, r). \quad (2.3.45)$$

Moreover, from the same requirement that every increment in the number of particles in a shell comes from outside the plasmon, the energies of these new particles will not depend on the time  $\rho$  at which they were injected into a shell or on their position in the plasmon at the instant of injection. This means that  $E_i$  does not depend on the position  $r_i$  or the time  $\rho_i$  of the injection of the particle  $i$ , and we can write  $\mathcal{Q}_1(E[\rho, r]) = \mathcal{Q}_1(E)$ .

#### 2) The energy distribution of the new particles coming into the plasmon follows a power-law with spectral index $-p$ .

$$\mathcal{Q}_1(E) = K_1 E^{-p}. \quad (2.3.46)$$

This is imposed for the same reasons that were used for the initial energy distribution function of the homogeneous solution in section 2.3.1.

**3) Uniform spatial distribution of the new particles pumped into the plasmon at the instant of their injection.**

The fact that when they enter the plasmon, the new electrons distribute uniformly implies that the instantaneous number density of fresh particles is the same for any  $dr$ . The number of particles injected per unit time in a shell is  $\frac{dN_s(\rho, r)}{d\rho}$ , as we defined at the beginning of the section. We will call this quantity  $\partial n_{inj}(\rho, r)$  for convenience. Then,

$$\frac{\partial n_{inj}(\rho, r)}{\partial V(r)} = constant \implies \frac{\partial n_{inj}(\rho, r)}{\partial V(r)} = \frac{N_{inj}(\rho)}{\frac{4\pi}{3} r^3}, \quad (2.3.47)$$

where  $N_{inj}(\rho)$  is the total number of particles injected at the instant  $\rho$  in the whole plasmon.

Therefore,

$$\partial n_{inj}(\rho, r) = \frac{N_{inj}(\rho)}{\frac{4\pi}{3}} \partial V(r), \quad (2.3.48)$$

and applying equation (2.3.33):

$$\partial n_{inj}(\rho, r) = dr \int_{E_{lo}}^{E_{uo}} Q(\rho, r, E) dE. \quad (2.3.49)$$

Substituting  $Q(\rho, r, E)$  as expressed in (2.3.45) and (2.3.46), and integrating over the energies of the injected particles, with lower and upper values  $E_{lo}$  and  $E_{uo}$  respectively, we have:

$$K_1 \frac{(E_{lo}^{1-p} - E_{uo}^{1-p})}{(1-p)} Q_2(\rho, r) = \frac{N_{inj}(\rho)}{\frac{4\pi}{3}} \partial V(r) \quad (2.3.50)$$

thus,

$$Q_2(\rho, r) = \frac{1}{K_1} \frac{(1-p)}{(E_{lo}^{1-p} - E_{uo}^{1-p})} \frac{N_{inj}(\rho)}{\frac{4\pi}{3}} \mathcal{V}(\sigma, r) dr. \quad (2.3.51)$$

- 4) **The number of particles pumped in per unit of time is constant during the injection interval.**

This is the simplest approach to the injection rate: the injection starts at  $\rho_i = 1$  and stops at  $\rho_i = \rho_{inj}$  and its rate is constant while it occurs.

If the total number of incoming particles during the injection is  $N_e$ , then the injection rate will be:

$$N_{inj} = \frac{N_e}{\rho_{inj} - 1}, \quad (2.3.52)$$

and since

$$\rho_{inj} = \frac{t_{inj}}{t_0} + 1, \quad (2.3.53)$$

we obtain the expression for the source function in a shell  $r$

$$\mathcal{Q}(\rho, r, E) dr = \frac{(1-p)}{(E_{lo}^{1-p} - E_{uo}^{1-p})} N_e \frac{t_0}{t_{inj}} \frac{1}{4\pi} E^{-p} \mathcal{V}_S(\rho, r) dr. \quad (2.3.54)$$

We describe the relation between the parameters that are independent of  $E$ ,  $\rho$ , or  $r$ , by defining the constant  $K$  as

$$K = \frac{3}{4} \frac{(1-p)}{(E_{lo}^{1-p} - E_{uo}^{1-p})} N_e \frac{t_0}{t_{inj}}. \quad (2.3.55)$$

Since the expression  $\mathcal{V}(\sigma, r) dr$  (2.3.3) depends on whether the shell is open or closed, we have:

$$\mathcal{Q}(\rho, r, E) dE dr = \begin{cases} \bullet K E^{-p} \frac{1}{\sigma} r [1 - (\sigma - r)^2] dE dr & \text{open shells} \\ \bullet 4K E^{-p} r^2 dE dr & \text{closed shells} \end{cases} \quad (2.3.56)$$

Now we can obtain the particular solution of the continuity equation for a shell  $r$ , for which the expression as function of  $\mathcal{Q}(\rho, r, E)$  is (2.3.44):

$$\mathcal{N}_P(\rho, r, E) = \int_{\rho_i=1}^{\rho_i=\rho} [\mathcal{Q}(\rho_i, r, E_i) \alpha \beta^{-2}] d\rho_i. \quad (2.3.57)$$

If for example, we develop the case where  $r$  is an open shell we have:

$$\mathcal{N}_P(\rho, r, E) = K \int_1^\rho E_i^{-p} \frac{1}{\sigma_i} r [1 - (\sigma_i - r)^2] \alpha \beta^{-2} d\rho_i.$$

Using relations (2.3.37), (2.3.41) and (2.3.2) we know that  $\alpha = \frac{\rho_i}{\rho}$ ,  $E_i^{-p} = \left(\frac{E}{3}\right)^{-p}$ .

and that  $\sigma_i = \frac{S}{\mathcal{R}(\rho_i)} = \frac{S}{\mathcal{R}_0 \rho_i}$ , hence:

$$\mathcal{N}_P(\rho, r, E) = K \frac{\mathcal{R}_0}{S} \frac{r}{\rho} E^{-p} \int_1^\rho [1 - (\sigma_i - r)^2] \rho_i^2 \beta^{(p-2)} d\rho_i.$$

Applying a similar development for a shell  $r$  that has been closed from an instant  $\rho_c$  to an instant  $\rho$  we find an analogous result.

In conclusion, the expression for the distribution function will be:

$$\mathcal{N}_P(\rho, r, E) = \begin{cases} \bullet K \frac{\mathcal{R}_0}{S} \frac{r}{\rho} E^{-p} \int_1^\rho [1 - (\sigma_i - r)^2] \rho_i^2 \beta^{(p-2)} d\rho_i & \text{open shells} \\ \bullet 4K E^{-p} \frac{r^2}{\rho} \int_1^\rho \rho_i \beta^{(p-2)} d\rho_i & \text{closed shells} \end{cases} \quad (2.3.58)$$

## 2.4 Applications to a source in a REXRB scenario

We have obtained the distribution function of a group of relativistic electrons in a plasmon with the geometry shown in Figure (2.1) and embedded in a magnetic field. This will allow us to calculate the diverse physical variables that are of interest for our problem and will help determine the parameters (like magnetic field, expansion velocity, etc) that are consistent with the observations of the REXRB to which we apply the model.

Therefore, we will use  $\mathcal{N}(\rho, r, E)$  in the next sections to calculate:

- 1) the total Adiabatic Losses:  $L_{Ad}(t)$ ,
- 2) the total Synchrotron Losses:  $L_{Sync}(t)$ ,

- 3) the total Inverse Compton Losses:  $L_{IC}(t)$ ,
- 4) the total radiated power:  $L_{Tot}(t)$ ,
- 5) the energetic distribution of the particles  $\mathcal{N}(t, E) dE$   
(i.e. the Break Frequency),
- 6) the number of particles in the plasmon as function of time:  $N_{pt}(t)$ ,
- 7) and the Radio Flux Density:  $S_\nu(t)$ .

To calculate these expressions it is necessary to integrate over the energy of all the particles, therefore we need to know the lower and upper energy values at every instant  $\rho$ . To start, we know the energy range  $[E_{lo}, E_{uo}]$  of the injected particles from outside since it is an input parameter of our model. From equation (2.3.7) we know the energy of an electron as a function of its initial energy. Since the lowest energy injected is  $E_{lo}$ , and if we consider there were no such particles when the injection started at  $\rho = 1$ , we can deduce the particles' lower energy (in the whole plasmon or in a shell) at any time  $\rho$  using equation (2.3.7) to calculate  $E_l(\rho, r) = E(\rho_i, r, E_i)$ , being  $\rho_i = 1$  and  $E_i = E_{lo}$ . For the case of the upper limit of the energy at any time  $\rho$  the value will depend on whether the injection has finished or not. If the injection continues the upper limit of the electron's energy for any shell will still be  $E_{uo}$ , since the particles that had been injected before  $\rho$  have already lost some energy. If the injection has finished, the upper energy in a shell will be  $E_u(\rho, r) = E(\rho_i, r, E_i)$ , where  $\rho_i = \rho_{inj}$  and  $E_i = E_{uo}$ , since  $\rho_{inj}$  was the last instant that the highest energy was injected and from there the upper energy also started to decay.

We know the distribution function is  $[\mathcal{N}_H(\rho, r, E) + \mathcal{N}_P(\rho, r, E)] dE dr$ . For the case in which we consider there is no injection we can use only the first term of the sum, whereas for the case in which we consider there was injection from the beginning (i.e. there were no particles in the plasmon when the injection started) the distribution will be only the second term of the sum. Since the first case can be included in the second for the limit  $\rho_{inj} \rightarrow 1$ , or can be added to it relatively easily, for the moment we will look for the expressions that arise from the second supposition. Hence, we will assume the injection started at  $\rho = 1$  and there were no electrons in the magnetized cloud before that time. Another approach can be followed when we relate the observed behaviour to the superposition of series of different injection events separated in time. Then the distribution of the particles already present in a cloud when the current injection event started can be calculated by adding to it the homogeneous solution for the distribution of the past event.

Therefore, considering there were no electrons when the injection started we shall find the expressions for:

### 1) Total Adiabatic Losses: $L_{Ad}(t)$

We have seen that the expression for the adiabatic losses of a distribution  $\mathcal{N}(\rho, r, E) dE dr$  of electrons is:

$$L_{Ad}(t) = \frac{1}{t_0} L_{Ad}(\rho), \quad (2.4.1)$$

$$\text{where } L_{Ad}(\rho) = \int_{S_{ph}} \int_{E_l(\rho, r)}^{E_u(\rho, r)} \frac{E}{\rho} \mathcal{N}(\rho, r, E) dE dr.$$

Therefore,

$$L_{Ad}(\rho) = \frac{1}{\rho} \int_{S_{ph}} \left[ \int_{E_l(\rho, r)}^{E_u(\rho, r)} E \mathcal{N}(\rho, r, E) dE \right] dr,$$

and substituting in it equation (2.3.44):

$$L_{Ad}(\rho) = \frac{1}{\rho} \int_{S_{ph}} dr \int_{E_l(\rho, r)}^{E_u(\rho, r)} E dE \int_{\rho_i=1}^{\rho_i=\rho} \left[ \mathcal{Q}(\rho_i, r, E_i) \alpha \beta^{-2} \right] d\rho_i \quad (2.4.2)$$

The development of this equation can have two forms depending on the values of  $\sigma(\rho_i)$  relative to 1, (i.e. the size of the expanding radius  $\mathcal{R}(\rho_i)$  relative to  $S$  at every  $\rho_i$ ):

- If  $\mathcal{R}(\rho) < S$  all the shells are open for all  $\rho_i$ .
- If  $\mathcal{R}(\rho) > S$  some shells are closed (those for which  $r < 1 - \sigma$ ).

For the second case, we assume that at  $\rho = 1$  (when the injection started) the plasmon was smaller than its separation from the primary (i.e.  $\mathcal{R}(1) < S$ ). Therefore, there was an instant –named  $\rho_c(r)$ –, between  $\rho_i = 1$  and  $\rho_i = \rho$  when a shell  $r$  closed.



We know that a shell is closed when  $r < (1 - \sigma)$  i.e.  $r < (1 - \frac{S}{R(\rho)})$ , which is  $r < (1 - \frac{S}{R_0} \frac{1}{\rho})$ . Hence, the instant  $\rho_c(r)$  at which a shell closes is:

$$\rho_c = \frac{S}{R_0} \frac{1}{(1-r)}. \quad (2.4.3)$$

For  $\rho_i < \rho_c(r)$  the shell  $r$  will be open, whereas for  $\rho_i > \rho_c(r)$  it will be closed.

Thus, using (2.3.58) and (2.4.2) the adiabatic losses can be expressed in the form:

$$L_{Ad}(\rho) = K \frac{R_0}{S} \frac{1}{\rho^2} \int_{S_{ph}} r dr \int_{E_l(\rho,r)}^{E_u(\rho,r)} E^{(1-p)} dE \int_1^\rho [1 - (\sigma_i - r)^2] \rho_i^2 \beta^{(p-2)} d\rho_i.$$

For  $\mathcal{R}(\rho) < S$

(2.4.4)

$$L_{Ad}(\rho) = K \frac{1}{\rho^2} \int_{S_{ph}} r dr \int_{E_l(\rho,r)}^{E_u(\rho,r)} E^{(1-p)} dE \left\{ \frac{R_0}{S} \int_1^{\rho_c(r)} [1 - (\sigma_i - r)^2] \rho_i^2 \beta^{(p-2)} d\rho_i + 4r \int_{\rho_c(r)}^\rho \rho_i \beta^{(p-2)} d\rho_i \right\}.$$

For  $\mathcal{R}(\rho) > S$

(2.4.5)

Where

$$\begin{aligned} \rho_c(r) &= \frac{S}{R_0} \frac{1}{(1-r)} & \text{for } r < [1 - S/\mathcal{R}(\rho)], \\ \rho_c(r) &= \rho & \text{for } r \geq [1 - S/\mathcal{R}(\rho)]. \end{aligned} \quad (2.4.6)$$

The constant  $K$  has been defined in (2.3.55) (depends on the parameters of the system) and the variable  $\beta$  has been defined in (2.3.39) (depends on  $\rho$ ,  $\rho_i$ , and  $r$ ).

## 2) Total Synchrotron Losses: $L_{Synch}(t)$

The expression for the synchrotron losses of a distribution  $\mathcal{N}(\rho, r, E) dE dr$  of electrons is:

$$L_{Synch}(t) = \frac{1}{t_0} L_{Synch}(\rho), \quad (2.4.7)$$

$$\text{where } L_{Synch}(\rho) = \int_{Sph} \int_{E_l(\rho, r)}^{E_u(\rho, r)} a_s \mathcal{B}_0^2 \frac{E^2}{\rho^4} \mathcal{N}(\rho, r, E) dE dr.$$

Which is equivalent to:

$$L_{Synch}(\rho) = a_s \frac{\mathcal{B}_0^2}{\rho^4} \int_{Sph} dr \int_{E_l(\rho, r)}^{E_u(\rho, r)} E^2 dE \int_{\rho_i=1}^{\rho_i=\rho} [\mathcal{Q}(\rho_i, r, E_i) \alpha \beta^{-2}] d\rho_i. \quad (2.4.8)$$

Considering the size of the plasmon with respect to the distance from the primary and with the same substitutions as in the previous case, we obtain:

$$L_{Synch}(\rho) = a_s K \frac{\mathcal{R}_0}{S} \frac{\mathcal{B}_0^2}{\rho^5} \int_{Sph} r dr \int_{E_l(\rho, r)}^{E_u(\rho, r)} E^{(2-p)} dE \int_1^\rho [1 - (\sigma_i - r)^2] \rho_i^2 \beta^{(p-2)} d\rho_i.$$

For  $\mathcal{R}(\rho) < S$  (2.4.9)

$$L_{Synch}(\rho) = a_s K \frac{\mathcal{B}_0^2}{\rho^5} \int_{Sph} r dr \int_{E_l(\rho, r)}^{E_u(\rho, r)} E^{(2-p)} dE \left\{ \frac{\mathcal{R}_0}{S} \int_1^{\rho_c(r)} [1 - (\sigma_i - r)^2] \rho_i^2 \beta^{(p-2)} d\rho_i + 4r \int_{\rho_c(r)}^\rho \rho_i \beta^{(p-2)} d\rho_i \right\}.$$

For  $\mathcal{R}(\rho) > S$  (2.4.10)

$(\rho_c(r)$  defined in 2.4.6)

**3) Total Inverse Compton Losses:  $L_{IC}(t)$** 

The expression for the inverse Compton losses of a distribution  $\mathcal{N}(\rho, r, E) dE dr$  of electrons is

$$L_{IC}(t) = \frac{1}{t_0} L_{IC}(\rho), \quad (2.4.11)$$

$$\text{where } L_{IC}(\rho) = \int_{Sph(\mathcal{R})} \int_{E_i(\rho, x)}^{E_u(\rho, x)} a_c \frac{t_0}{4\pi c} \frac{L_{uv}}{x^2} E^2 \mathcal{N}(\rho, x, E) dE dx.$$

If we apply the substitutions as in the previous case and take into account  $r = \frac{x}{\mathcal{R}} = \frac{x}{\mathcal{R}_0 \rho}$ , then:

$$L_{IC}(\rho) = a_c \frac{t_0}{4\pi c} \frac{L_{uv}}{\mathcal{R}_0 \rho} \int_{Sph} \frac{dr}{r^2} \int_{E_i(\rho, r)}^{E_u(\rho, r)} E^2 dE \int_{\rho_i=1}^{\rho_i=\rho} [Q(\rho_i, r, E_i) \alpha \beta^{-2}] d\rho_i. \quad (2.4.12)$$

With similar substitutions and development as the cases of adiabatic and synchrotron losses we obtain:

$$L_{IC}(\rho) = a_c K \frac{L_{uv}}{S} \frac{1}{\rho^2} \int_{Sph} \frac{dr}{r} \int_{E_i(\rho, r)}^{E_u(\rho, r)} E^{(2-p)} dE \int_1^\rho [1 - (\sigma_i - r)^2] \rho_i^2 \beta^{(p-2)} d\rho_i.$$

For  $\mathcal{R}(\rho) < S$  (2.4.13)

$$L_{IC}(\rho) = a_c K \frac{L_{uv}}{\mathcal{R}_0} \frac{1}{\rho^2} \int_{Sph} \frac{dr}{r} \int_{E_i(\rho,r)}^{E_u(\rho,r)} E^{(2-p)} dE \left\{ \frac{\mathcal{R}_0}{S} \int_1^{\rho_c(r)} [1 - (\sigma_i - r)^2] \rho_i^2 \beta^{(p-2)} d\rho_i + \frac{4}{r} \int_{\rho_c(r)}^{\rho} \rho_i \beta^{(p-2)} d\rho_i \right\}.$$

$$\text{For } \mathcal{R}(\rho) > S \quad (2.4.14)$$

( $\rho_c(r)$  defined in 2.4.6)

#### 4) Total radiated power: $L_{Tot}(t)$

The total radiated power (i.e. the total energy losses  $L_{Tot}(t) = \frac{dE}{dt}(t)$ ) is the sum of (2.4.1), (2.4.7), and (2.4.11):

$$L_{Tot}(t) = L_{Ad}(t) + L_{Sync}(t) + L_{IC}(t).$$

Thus,

$$L_{Tot}(t) = \frac{1}{t_0} [L_{Ad}(\rho) + L_{Sync}(\rho) + L_{IC}(\rho)]. \quad (2.4.15)$$

#### 5) Energetic distribution of particles $\mathcal{N}_{pe}(\rho, E) dE$

The number of particles ( $\mathcal{N}_{pe}(t, E) dE$ ) with an energy  $E$  at instant  $\rho$  is

$$\mathcal{N}_{pe}(\rho, E)_{pe} dE = \int_{Sph} \mathcal{N}(\rho, r, E) dr dE. \quad (2.4.16)$$

Substituting equation (2.3.44) in the integral we obtain:

$$\mathcal{N}(\rho, E)_{pe} dE = dE \int_{Sph} dr \int_{\rho_i=1}^{\rho_i=\rho} [\mathcal{Q}(\rho_i, r, E_i) \alpha \beta^{-2}] d\rho_i.$$

From (2.3.58) it is straightforward to obtain:

$$\begin{aligned} \mathcal{N}_{pe}(\rho, E) dE = \\ E^{-p} dE \left[ K \frac{\mathcal{R}_0}{S} \frac{1}{\rho} \int_{S_{ph}} r dr \int_1^\rho [1 - (\sigma_i - r)^2] \rho_i^2 \beta^{(p-2)} d\rho_i \right] \\ \text{For } \underline{\mathcal{R}(\rho) < S} \end{aligned} \quad (2.4.17)$$

$$\begin{aligned} \mathcal{N}_{pe}(\rho, E) dE = \\ E^{-p} dE \left[ K \frac{1}{\rho} \int_{S_{ph}} r dr \left\{ \frac{\mathcal{R}_0}{S} \int_1^{\rho_c(r)} [1 - (\sigma_i - r)^2] \rho_i^2 \beta^{(p-2)} d\rho_i \right. \right. \\ \left. \left. + 4r \int_{\rho_c(r)}^\rho \rho_i \beta^{(p-2)} d\rho_i \right\} \right]. \\ \text{For } \underline{\mathcal{R}(\rho) > S} \quad (2.4.18) \\ (\rho_c(r) \text{ defined in 2.4.6}) \end{aligned}$$

We know that both the synchrotron losses and the inverse Compton losses depend directly on the square of the electrons' energy, which leads to the high energy electrons to shift quickly to lower energies, as we already mentioned. Thus, a consequence of the presence of primary-object photons and a strong magnetic field, is a rapid evolution of the high energy tail of the relativistic particle energy distribution  $\mathcal{N}_{pe}(\rho, E) dE$ . The short life time of the most energetic particles produces a “**break energy**” corresponding to an electron life time smaller than the evolution time of the system. The number of particles drops rapidly for energies higher than the break energy. This should be reflected in the radio spectra: we know that the frequency region where most of the synchrotron radiation is emitted by a particle with energy  $E$  is around the frequency defined by  $\nu_c = C_1 \frac{B_0 R_0^2}{R^2} E^2$ . Therefore, corresponding to the “break energy” there is a “**break frequency**” above which the emitted spectrum steepens to a high negative slope. The values for the break frequency depend strongly on the proximity to the primary, the strength of the magnetic field, and the

size of the emitting region (as the region expands the break frequency decreases), therefore the determination of this frequency or a lower limit to it can help us to place constraints on the dimensions and location of the plasmon.

### 6) Number of particles in the plasmon as function of time: $N_{pt}(t)$

The total number of particles present in the cloud at a given time  $\rho < \rho_{inj}$  will be the integration over the energies of the particles in a shell and the integration of that over all the shells at that instant, i.e:

$$N_{pt}(\rho) = \int_{Sph} \left[ \int_{E_l(\rho,r)}^{E_u(\rho,r)} \mathcal{N}(\rho, r, E) dE \right] dr.$$

Which is

$$N_{pt}(\rho) = \int_{Sph} dr \int_{E_l(\rho,r)}^{E_u(\rho,r)} dE \int_{\rho_i=1}^{\rho_i=\rho} \left[ \mathcal{Q}(\rho_i, r, E_i) \alpha \beta^{-2} \right] d\rho_i. \quad (2.4.19)$$

Actually, since we have defined  $N_{inj}$  as the constant injection rate of particles, at a given time  $\rho < \rho_{inj}$  the number of particles will be:

$$N_{pt}(\rho) = N_{inj} (\rho - 1).$$

On the other hand,  $N_e$  is the total number of particles in the plasmon after the injection stops, therefore, we know that the injection rate is:

$$N_{inj} = \frac{N_e}{\rho_{inj} - 1},$$

and since  $(\rho - 1) = \frac{t}{t_0}$  then,  $N_{inj} = N_e \frac{t_0}{t_{inj}}$ ; and  $N_{pt}(t) \equiv N_{pt}(\rho) = N_{inj} \frac{t}{t_0}$ .

Finally,

$$N_{pt}(t) = \frac{t}{t_{inj}} N_e \quad (2.4.20)$$

Comparison between equations (2.4.19) and (2.4.20) will allow us to test the expressions for  $\mathcal{Q}(\rho_i, r, E_i)$ ,  $\alpha$  and  $\beta$  – entered in the model's computer codes –, and to estimate the steps  $dE$ ,  $dr$  and  $d\rho_i$  needed in the code's numerical integration in order to achieve a good balance between the accuracy level of the non-analytical multiple

integrals and the computational time required.

### 7) Radio Flux Density: $\mathcal{S}_\nu(t)$

In our case, the best information we have to test our models are the radio light curves observed in the REXRBs we study (together with some X-ray detections and X-ray light curves). Let's then see the theoretical radio flux density curve predicted for our model at a given radio frequency  $\nu$ .

The specific intensity  $I_\nu$  of an emitting body element is defined as the radiant power per steradian and unit frequency crossing through a perpendicular unit area.

The flux density  $\mathcal{F}_\nu$  detected from the whole body is the sum of all the body elements' intensities diluted by their solid angle with respect to the observer, is to say:

$$\mathcal{F}_\nu = \int_{Vol} I_\nu d\Omega,$$

which is equivalent to:

$$\mathcal{F}_\nu = \int_{Vol} I_\nu \frac{da}{D^2}, \quad (2.4.21)$$

where  $da$  is the area of a radiating element and  $D$  is the distance of the observer from it.

In order to know the flux density, we must know the expressions of the variables inside the integral in (2.4.21). For this case, we will not take into account interactions between particles themselves but interactions between particles and radiation. Electrons in a radiation field absorb and emit photons both spontaneously and by induction. In this scenario, the specific intensity variation  $dI_\nu$  can be described by the **equation of radiative transfer**:

$$\frac{dI_\nu}{dl} = -\kappa_\nu I_\nu + \varepsilon_\nu, \quad (2.4.22)$$

where

- $dl$  is the length (along to the observer's direction) of the matter element where the intensity variation is produced.

- $\kappa_\nu$  and  $\varepsilon_\nu$  are the absorption coefficient and emission coefficient respectively. They are phenomenological parameters which depend on the microscopic processes of the medium.

The radiative transfer equation (2.4.22) describes, in a macroscopic fashion, the conservation of the radiation field's energy.

To solve it, it is more convenient to express equation (2.4.22) in the following way:

$$\frac{dI_\nu}{d\tau_\nu} = -I_\nu + \mathcal{S}_\nu, \quad (2.4.23)$$

where the definitions:

$$\begin{aligned} \mathcal{S}_\nu &= \frac{\varepsilon_\nu}{\kappa_\nu} \\ \tau_\nu(l) &= \int_0^l \kappa_\nu dl, \end{aligned} \quad (2.4.24)$$

are applied.

$\tau_\nu$  is the so called *optical depth* at frequency  $\nu$  and  $\mathcal{S}_\nu$  is named *source function* at frequency  $\nu$ . The total length  $l$  is the optical path covered by the photons along that direction.

Let's see the physical meaning of the variables  $\mathcal{S}_\nu$  and  $\tau_\nu$ , considering a simple case where we assume the absorption and emission coefficient to be constant through the observed region. In this example, the solution of the linear differential equation (2.4.23) will be:

$$I_\nu = I_\nu(0)e^{-\tau_\nu} + \mathcal{S}_\nu(1 - e^{-\tau_\nu}). \quad (2.4.25)$$

$I_\nu(0)$  is the incident radiation from the background (since the optical path is 0). Then, from the previous equation, in this simple case the incident radiation suffers an absorption of a factor  $e^{-\tau_\nu}$ , and the source function  $\mathcal{S}_\nu$  (i.e. the ratio between the emission and absorption coefficients) stands for the balance of the radiation produced in every element  $dl$  and is also absorbed by a factor  $e^{-\tau_\nu}$  from the point where it is produced to the end of the path.

Therefore,  $\tau_\nu = \int_0^l \kappa_\nu dl$  is an adimensional magnitude that accounts for the attenuation over the intensity  $I_\nu$  when crossing a radiant region of longitude  $l$ .



It is also illustrative, for this example, to examine the form of the specific intensity in the asymptotic cases where the optical depth is either large or small. Lets assume the incident background radiation is null. Then:

- For  $\tau_\nu \gg 1$  the equation (2.4.25) can be approximated to  $I_\nu = \mathcal{S}_\nu$ , which means only the radiation at the surface of the region is seen. It is then said that **the emission is optically thick or opaque for the frequency  $\nu$** .

- For  $\tau_\nu \ll 1$  the equation (2.4.25) can be approximated to  $I_\nu = \mathcal{S}_\nu \tau_\nu$ , which means we can see the radiation from the interior of the region, although it is somehow absorbed by the corresponding factor  $\tau_\nu$  depending on the depth. It is then said that **the emission is optically thin for the frequency  $\nu$** .

To obtain  $I_\nu$  we need to know the values of  $\mathcal{S}_\nu$  and  $\tau_\nu$ , both of them depending on the coefficients  $\kappa_\nu$  and  $\varepsilon_\nu$ . In our case the mechanisms of interactions between electrons and radiation that can be considered are the synchrotron radiation, the self-inverse Compton scattering, and the free-free radiation (or thermal bremsstrahlung). In this way, the emission coefficient and the absorption coefficient will be:

$$\begin{aligned}\varepsilon_\nu &= \varepsilon_\nu^s + \varepsilon_\nu^{ic}, \\ \kappa_\nu &= \kappa_\nu^s + \kappa_\nu^{ic} + \kappa_\nu^{ff}.\end{aligned}\tag{2.4.26}$$

where the super-indexes *s*, *ic*, and *ff* stand for synchrotron, self-Inverse Compton, and free-free radiation respectively. We note that the emission coefficient for the free-free radiation is not taken into account since it is generally insignificant compared with  $\varepsilon_\nu^s$ .

#### I- *Synchrotron absorption and emission coefficients*

The emission coefficient for the case of synchrotron radiation is found using (2.1.4) and adapting it for a distribution of a group of electrons. Thus, in c.g.s units,

$$\varepsilon_\nu^s = 1.87 \times 10^{-23} B \int_0^\infty n(\rho, E) F\left(\frac{\nu}{\nu_c}\right) dE.\tag{2.4.27}$$

where  $n(\rho, E)$  is the distribution function at time  $\rho$  per unit volume.

The atomic properties of matter are linked through its macroscopic characteristics through Einstein's probability coefficients of absorptions and emissions

(both induced and spontaneous). Using these, Pacholczyk (1970) shows the deduction to find  $\kappa_\nu^s$  for the case of an isotropic energetic distribution function of relativistic electrons. The author also assumes that the linear momentum of the interacting photons is much smaller than the linear momentum of the electrons –which is consistent with our case since we consider the radiation field created by the synchrotron emission, therefore, the photons are in the radio band of the spectrum (i.e. have low energies) whereas the electrons have relativistic energies. The expression found for the absorption coefficient, in c.g.s units, is:

$$\kappa_\nu^s(\rho) = -1.87 \times 10^{-23} \frac{c^2}{2\nu^2} B \int_{E_l(\rho)}^{E_u(\rho)} E^2 \frac{d}{dE} \left[ \frac{n(\rho, E)}{E^2} \right] F\left(\frac{\nu}{\nu_c}\right) dE.$$

thus,

$$\kappa_\nu^s(\rho) = -1.87 \times 10^{-23} \frac{c^2}{2\nu^2} B \int_{E_l(\rho)}^{E_u(\rho)} E \left[ \frac{dn(\rho, E)}{dE} - \frac{2}{3} \frac{1}{E} n(\rho, E) \right] F\left(\frac{\nu}{\nu_c}\right) dE. \quad (2.4.28)$$

## II- Self-Inverse Compton absorption and emission coefficients

The self-inverse Compton effect is the interaction of relativistic particles with the radio-photons that themselves radiate due to their movement in the magnetic field. After the collision the photon has gained energy at the expense of the electron's energy. Then, the emission and absorption coefficients are:

$$\begin{aligned} \varepsilon_\nu^{ic}(\rho) &= \int \int J(\nu_i) \sigma\left(\frac{h\nu}{mc^2}, \frac{h\nu_i}{mc^2}, \frac{E}{mc^2}\right) n(\rho, E) d\nu_i dE, \\ \kappa_\nu^{ic}(\rho) &= \int \int \sigma\left(\frac{h\nu}{mc^2}, \frac{h\nu_i}{mc^2}, \frac{E}{mc^2}\right) n(\rho, E) d\nu_i dE. \end{aligned} \quad (2.4.29)$$

where  $J(\nu_i)$  is the averaged intensity of the radiation field, and  $\sigma$  represents the probability that a photon of frequency  $\nu_i$  shifts to frequency  $\nu$  after the interaction of a relativistic particle with energy  $E$ .

The expressions for  $J(\nu_i)$  and  $\sigma$  can be found in Pacholczyk (1970)

## III- Free-free or thermal bremsstrahlung absorption coefficient

This is produced by the change of energy of free non-relativistic electrons that might be present on the plasmon when encountering an ion. The absorption coefficient in this case is:

$$\kappa_\nu^{th}(\rho) = 9.8 \cdot 10^{-3} \frac{n_e^2}{T_e^{3/2} \nu^2} \left[ 17.7 + \ln \left( \frac{T_e^{3/2}}{\nu} \right) \right]. \quad (2.4.30)$$

where  $T_e$  is the temperature of the thermal electrons and  $n_e$  its number density.

Therefore, we see in the expressions for  $\kappa_\nu$  and  $\varepsilon_\nu$  that to calculate the source function  $\mathcal{S}_\nu$  and optical depth  $\tau_\nu$ , we need the energetic distribution function of the relativistic particles per unit volume (which we will call “specific energy distribution function”). We know that the number of particles with energies in the range  $[E, E + dE]$  in a shell  $[r, r + dr]$  per unit of volume is  $\frac{\mathcal{N}(\rho, E, r) dE dr}{\mathcal{V}(\sigma, r) dr}$ , thus,  $\varepsilon_\nu$  and  $\kappa_\nu$  will depend on the position  $r$  in the plasmon, i.e. they are not uniform. This implies  $\tau_\nu$  will depend on the line of sight from where the plasmon is observed. Because we do not know our observer’s position with respect to the primary and the plasmon, and, furthermore, this can change in one cycle due to the orbital movement or the ejection of the cloud, we cannot predict  $\tau_\nu$  exactly.

The approach we will take then, is to average the energetic distribution per unit volume over the whole plasmon volume.

For a single shell the specific energy distribution will be:

$$n(\rho, E, r) dE = \frac{\mathcal{N}(\rho, E, r) dE dr}{\mathcal{V}(\sigma, r) dr}. \quad (2.4.31)$$

To the whole plasmon we will assign an averaged specific energy distribution function  $\overline{n(\rho, E) dE}$ , defined as the sum of all the  $n(\rho, E, r) dE$  weighed by the volume corresponding to each shell, i.e.:

$$\overline{n(\rho, E) dE} = \frac{\int_{S_{ph}} n(\rho, E, r) dE \mathcal{V}(\sigma, r) dr}{\int_{S_{ph}} \mathcal{V}(\sigma, r) dr}.$$

Integrating the denominator and substituting equation (2.4.31) in the integral of the numerator, we can write:

$$\overline{n(\rho, E) dE} = \frac{3}{4\pi} \int_{S_{ph}} \frac{\mathcal{N}(\rho, E, r) dE dr}{\mathcal{V}(\sigma, r) dr} \mathcal{V}(\sigma, r) dr,$$

which is:

$$\overline{n(\rho, E) dE} = \frac{3}{4\pi} \int_{Sph} \mathcal{N}(\rho, E, r) dE dr,$$

and from (2.4.16) we derive

$$\overline{n(\rho, E) dE} = \frac{3}{4\pi} \mathcal{N}_{pe}(\rho, E) dE. \quad (2.4.32)$$

Therefore, the averaged specific energy distribution equals the number of particles in the whole plasmon between energies  $E$  and  $E + dE$  divided by its volume, as expected assuming the consistency of definitions.

The optical path of the radiation is symmetrical in tubes at equal distance  $s$  from the center of the sphere. Then it will be

$$l = 2\sqrt{(\mathcal{R}^2 - s^2)} \quad \text{and} \quad \tau_\nu = \int_0^{2\sqrt{(\mathcal{R}^2 - s^2)}} \kappa_\nu dl., \text{ so, in this case,}$$

$$\tau_\nu(\rho) = 2\sqrt{(\rho\mathcal{R}_0)^2 - s^2} \kappa_\nu \quad (2.4.33)$$

In this way, since the area  $da$  of a shell is  $da = 2\pi s ds$  the flux density (2.4.21) can be expressed as:

$$\mathcal{F}_\nu = \frac{2\pi}{D^2} \int_{Vol} I_\nu(s) s ds. \quad (2.4.34)$$

To calculate the specific intensity  $I_\nu(s)$  we will assume the background radiation is null and use

$$I_\nu(s) = \mathcal{S}_\nu (1 - e^{-\tau_\nu(s)}),$$

and introducing it in equation (2.4.34) we obtain

$$\mathcal{F}_\nu(\rho) = \frac{\pi \mathcal{R}(\rho)^2}{D^2} \mathcal{S}_\nu(\rho) - \frac{2\pi}{D^2} \mathcal{S}_\nu(\rho) \int_0^{\mathcal{R}(\rho)} e^{-\tau_\nu(s,\rho)} s ds.$$

Solving the integral after substituting in it (2.4.33) and applying  $\mathcal{R}(\rho) = \mathcal{R}_0 \rho$ , we finally obtain:

$$\mathcal{F}_\nu(\rho) = \frac{\pi}{D^2} \mathcal{S}_\nu(\rho) \left[ \mathcal{R}_0^2 \rho^2 + \frac{\mathcal{R}_0 \rho}{\kappa_\nu(\rho)} e^{-(2\kappa_\nu(\rho)\mathcal{R}_0\rho)} - \frac{1}{2\kappa_\nu(\rho)^2} \left( 1 - e^{-(2\kappa_\nu(\rho)\mathcal{R}_0\rho)} \right) \right] \quad (2.4.35)$$

The asymptotic solutions for the flux density are:

- **For an optically thick frequency (i.e.  $\tau_\nu \gg 1$ ):**

$$\mathcal{F}_\nu(\rho) = \frac{2\pi \mathcal{R}_0^2 \rho^2}{D^2} \mathcal{S}_\nu(\rho)$$

- **For an optically thin frequency (i.e.  $\tau_\nu \ll 1$ ):**

$$\mathcal{F}_\nu(\rho) = \frac{4\pi}{3} \mathcal{R}_0^3 \frac{r^3}{D^2} \mathcal{S}_\nu(\rho) \kappa_\nu(\rho)$$

Since the absorption coefficient decreases for increasing frequencies, the larger the frequency, the lower the optical depth, or equivalently, for low enough frequencies the medium is opaque.

Thus, the procedure we follow in our code to **obtain the radio flux density at frequency  $\nu$  at a given time  $t$**  is:

- First calculate  $\overline{n(\rho, E) dE}$  by integrating numerically  $\frac{3}{4\pi}$  times (2.4.17) –or (2.4.18), depending on the size of the plasmon with respect to  $S^-$ .
- Then substitute it in the expressions (2.4.27), (2.4.28), and (2.4.29). to get  $\varepsilon_\nu^s$ ,  $\kappa_\nu^s$ , and  $\varepsilon_\nu^{ic}$  and  $\kappa_\nu^{ic}$  respectively, and also through numerical integration.
- Compute  $\mathcal{S}_\nu(\rho)$  given in (2.4.24) and  $\tau_\nu(\rho)$  given in (2.4.33).
- Introducing the previous variables in (2.4.35) obtain the radio flux density of the source at frequency  $\nu$ .
- To calculate the radio flux density for several frequencies set a loop starting from the second point.

- To calculate the light curve given by the radio flux density at the desired frequencies set a loop starting from the first point.

In the next two chapters we discuss the physical predictions given by this model and compare them with observed radio and X-ray light curves of LS I+61°303 and Cygnus X-3.

## Chapter 3

# LS I+61°303 as a radio, X-ray and $\gamma$ -ray source: Modeling the emission

### 3.1 Introduction

The behaviour seen in older observations of LS I+61°303 indicated synchrotron radiation from expanding plasmons in them. This fact together with previous models fits, suggested at the same time the theoretical basis for our model and the type of further observations we needed for a better knowledge of the source.

We collected different series of observations taken by our team, collaborators and some from the literature and public data bases. Some of them were destined to test whether different predictions of models from different authors were satisfied. In this part we concentrate in the analysis of luminosity information (magnitudes, light curves, spectra) given by the observations at different radio wavelengths and high energy (in contrast with further chapters where we analyse radio images or study variability and periodic behaviour).

The different type of observations we used are:

- 1- Coordinated X-ray and two-frequency radio observations over one LS I+61°303 orbital cycle**

Taken in August–September 1992 with the ROSAT observatory (X-ray) and

the Very Large Array (cm). Up to that moment there were very few observations of LS I+61°303 at X-ray energies and none of them had been regularly sampled over a long period of time. Therefore, to observe during a whole cycle at cm and X-ray would allow to more deeply investigate the X-ray properties of the source (specially the possible existence of variability) and its relationship with the radio emission.

## 2- Simultaneous radio and $\gamma$ -ray observations

Taken by Kniffen et al. in 1993 and 1994, and Tabani et al. (1996) in 1994 and 1995. We use them to test the whether our model is consistent with the ratio of luminosities between high energy emission and radio emission.

## 3- Coordinated mm, submm and cm observations

We took them simultaneously with the JCMT (mm and submm) and the VLA (cm) in October 1994 on with the objective of investigating the possible existence of an spectral turn-down at high frequencies as it was predicted for our model (see Chapter 2, section 2.4).

We also carried out a monitoring campaign from October 1994 to April 1995 of the source at cm –using the 70m antenna at the MDSCC<sup>a</sup> in Robledo de Chavela (Spain)– and submm using the Nobeyama Millimeter Array (NMA) observatory in Japan. Nonetheless, simultaneity was difficult to achieve in this case due to the large difference in the longitude earth coordinate of the observatories.

Together with LS I+61°303 we observed Cygnus X-3 and SS433 in both the coordinated VLA–JCMT sessions and the Madrid–Nobeyama survey.

## 4- Multiwavelength radio light curves during a LS I+61°303 orbital cycle:

Simultaneous observations at 6 different centimetric wavelength taken with the VLA in June–July 1994 (Paredes et al., 1996). This is the widest coverage in frequency of an observed radio outburst of the source and provides us with useful information about the radio–spectral behavior.

## 5- A large variety of monowavelength radio light curves and single data observations

From bibliography, taken by collaborators, and mainly taken by ourselves at the

---

<sup>a</sup>Madrid INTA–NASA Deep Space Communication Complex



antenna DSS63 in the space communications complex INTA-NASA (Madrid, Spain).

In the following sections we present in detail the analysis and results of the different type of observations listed above.

## 3.2 Simultaneous Radio and X-ray observations of LS I+61°303 during an orbital cycle

Since the first detection of X-ray photons from LS I+61°303 was reported by Bignami et al in 1981, further X-ray observations of the source were taken seldomly, and none of them was devoted to establish whether this emission was variable or not. Although Bignami et al. themselves reported the source to be constant within a 30% of a flux level of  $2 \times 10^{-12}$  erg cm<sup>-2</sup> s<sup>-1</sup> they were based on only two data points taken several cycles apart and in different phases of the radio period.

In order to see whether the X-ray emission from LS I+61°303 experimented any variations during an orbital cycle, and test the possible relationship of the X-ray photons with the radio emission, simultaneous X-ray observations with the ROSAT observatory and two wavelength centimetric observations with the antenna network VLA were carried out in August–September 1992. The temporal overlap between the different frequencies spans through an orbital 26 day cycle although for one of the radio frequencies the observations were prolonged through the following outburst.

### 3.2.1 Radio Observations

Radio observations were carried out at 1.5 GHz and 4.9 GHz with the Very Large Array observatory, during 16 different observing sessions spanning from August 10th to September 30th 1992. The details of the observing and data reduction procedures are described in Taylor et al., (1996).

Figure 3.1 shows the results of the flux measurements versus time. As it can be seen the measurements at 4.9 GHz span through about one orbital period whereas the 1.5 GHz measurements are taken in a time range of about 50 days which is almost

two times a cycle of the 26.5 orbital period. Two radio outburst were tracked with these data: the first one was observed in both frequencies although it was traced out with more detail at 4.9 GHz; the second one was only observed at 1.5 GHz. The X-ray measurements were taken during the same time range as the 4.9 GHz data.

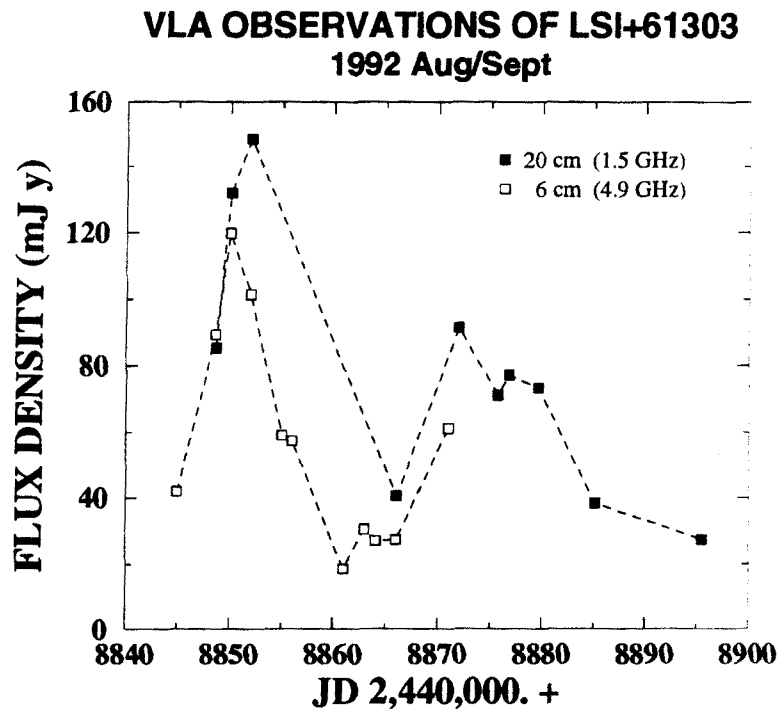


Figure 3.1: The radio flux densities of LS I+61°303 obtained at  $\nu = 4.9$  GHz (open squares) and  $\nu = 1.5$  GHz (filled squares)

Table 3.1 shows the flux density results of each measurement.

### 3.2.2 X-ray Observations

The X-ray flux from LS I+61°303 was measured with the ROSAT<sup>b</sup> during 9 sessions spanning from August 11th to September 4th, 1992. The detector measured photons with energies in the range 0.07 to 2.48 KeV. The details of the observation and data reduction procedures are presented in Taylor et al., 1996.

The energy flux in the 0.07 to 2.48 keV band was derived by fitting the observed

<sup>b</sup>Roentgen-Satellit

Table 3.1: Radio Flux Densities

Julian Date (-2,440,000)	phase	1.5 GHz Flux Density (mJy)	4.9 GHz Flux Density (mJy)
8844.98	0.78		42 ± 2
8848.73	0.90	85 ± 3	89 ± 4
8850.07	0.95	132 ± 4	119 ± 3
8852.00	0.02	148 ± 5	101 ± 3
8855.05	0.14		59 ± 2
8855.99	0.17		57 ± 2
8860.95	0.36		19 ± 1
8862.97	0.44		31 ± 1
8864.07	0.48		27 ± 1
8866.01	0.55	41 ± 2	28 ± 1
8870.98	0.74	92 ± 3	61 ± 2
8875.73	0.92	71 ± 2	
8876.73	0.95	77 ± 2	
8879.64	0.06	74 ± 2	
8885.11	0.27	39 ± 1	
8895.52	0.66	60 ± 2	

Table 3.2: X-ray Observations

Julian Date (-2,440,00)	Counts	Flux*		
		Power Law	Black Body	Bremmstrahlung
8845.71	535	2.57	2.28	2.45
8849.90	42	0.15	0.13	0.15
8853.50	45	0.24	0.21	0.23
8856.13	102	0.76	0.63	0.72
8860.05	178	1.32	1.16	1.27
8864.04	190	3.44	2.98	3.33
8867.95	182	2.41	2.10	2.26
8868.95	493	2.25	1.88	2.10
8869.95	549	2.48	2.18	2.37

\* in units of  $10^{-12}$  erg cm $^{-2}$  s $^{-1}$

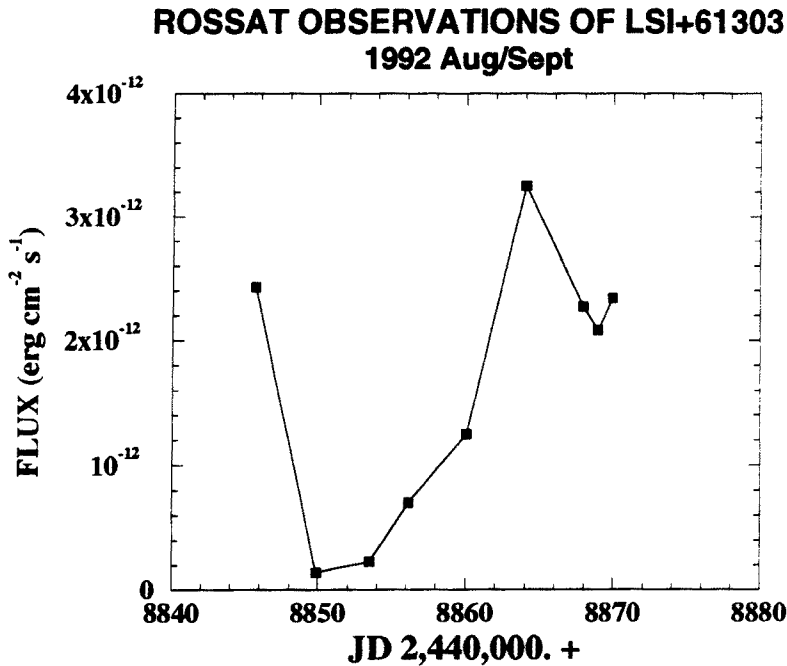


Figure 3.2: The X-ray flux over the 0.07 to 2.48 keV band.

spectral distribution to power law, blackbody and optically-thin thermal energy spectra. The signal-to-noise level per energy bin was very similar for each of these spectral models. The low energy part of the X-ray spectrum is dominated by the effects of absorption by neutral gas in the interposed interstellar medium. Thus, the flux was corrected applying the value of  $N_H = 8.4 \times 10^{21} \text{ cm}^{-2}$  for the atomic hydrogen column density taken from measurements by Frail & Hjellming, 1991. Table 3.2 shows the results of the calculated flux for the three spectral models.

The X-ray flux plotted versus Julian date is displayed in Figure 3.2, The flux values taken for the representation have been calculated by averaging the flux obtained from the three model spectral distributions. The plot shows the flux to exhibit a variation of about a factor of 10 in a time scale of 20 days, similarly to the radio outburst occurred in the same cycle. The peak luminosity obtained after correction by interstellar columnar density, and considering the distance from LS I+61°303 to be 2.3 kpc ranges from one to several  $10^{34} \text{ ergs s}^{-1}$ , depending on the spectral model applied.

*This is the first detected X-ray outburst of LS I+61°303. The existence of X-ray*

fluctuations in this source has been also reported recently by Goldoni & Mereghetti (1995). They observed a variation of a factor of 3 over a period of a few days, with an average X-ray flux of  $4 \times 10^{-12}$  erg cm<sup>-2</sup> s<sup>-1</sup>.

### 3.2.3 Analysis: Radio versus X-ray Variations

Both the radio and X-ray flux densities varied by a factor of 10, with the X-ray peak occurring at phase 0.5 and the radio peak at phase 0.95. The range of phase of high X-ray emission matches the phase interval during which the source is, on average, active at radio.

In Figure 3.3 we show the radio and X-ray flux density and spectral properties plotted against radio phase. The error bars shown for the spectral data are plus and minus one standard deviation. The upper panel shows the 4.9 GHz radio flux density and the X-ray flux. For X-ray data we have adopted the average value for the three model spectral distributions. Both data sets have been normalized to a peak value of unity. Two facts are readily apparent: one, the radio and X-ray emission exhibit a similar fractional change in flux of about a factor of 10, and two, the timing of the peak intensity at radio and X-ray differ by approximately 0.5 in phase. The exact phase difference between the radio and X-ray curves is difficult to estimate, both because of the coarse sampling of the data.

The central panel shows the radio spectral index,  $\alpha$ , defined by assuming a power dependence,  $\nu^\alpha$ . There is a clear evolution from positive to negative spectral index during the rise and decay of the first radio outburst. The spectral index crosses zero close to the time of peak radio flux density, and decays to a constant value of -0.3. The average spectral index following the decay is  $-0.33 \pm 0.04$ . The spectral index appears to remain at this value into the rise of the second outburst. However, the time sampling of the radio light curve is poor, and it is possible that the radio peak occurred between the last two radio measurements which are widely separated in phase - 0.55 and 0.74. This is the more common range of phase of peak flux density (Taylor & Gregory 1984; Paredes et al. 1990). In that case, the last measurement of spectral index would be during radio decay.

To examine the possibility of a change in the spectral shape of the X-ray emission, we calculated a hardness ratio based on the observed spectra. The hardness ratio was

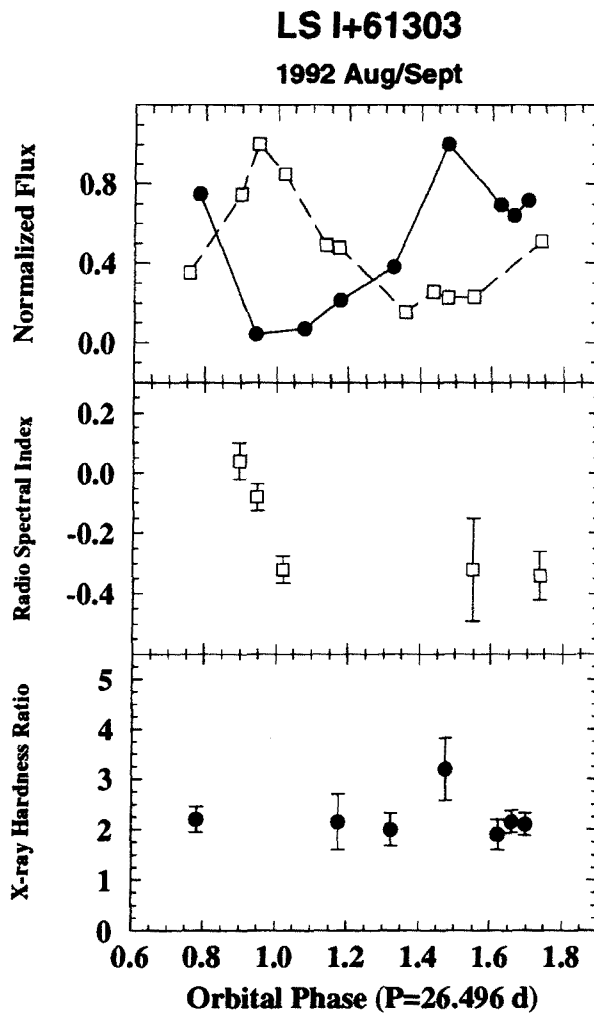


Figure 3.3: Comparison of the X-ray and radio flux density and spectral variations. The top panel shows the 4.9 GHz radio flux density (dashed line and open squares) and the X-ray flux (solid line and filled circles). In both cases the flux measurements have been normalized by the peak flux. The radio spectral index between 4.9 GHz and 1.5 GHz is shown in the central panel. The bottom panel shows the X-ray hardness ratio, defined as the ratio of photon counts in the energy range 1.0 to 2.48 keV to those in the 0.07 to 1.0 keV range. There is a suggestion of hardening of the X-ray emission at peak X-ray flux co-incident with the onset of the second radio outburst. All quantities are plotted against the phase of the radio period of 26.496 days.

Table 3.3: Parameters used for the model fit displayed in Figure 3.4

$R_0$	$1.5 \cdot 10^{13}$ cm	Initial sphere radius
$v_{exp}$	$3 \cdot 10^7$ cm s <sup>-1</sup>	Expansion velocity
$v_{jec}$	$1.5 \cdot 10^9$ cm s <sup>-1</sup>	Ejection velocity
$B_0$	0.15 G	Magnetic field at $R_0$
$L_{uv}$	$10^{38}$ erg s <sup>-1</sup>	Luminosity uv photons
P	2.1	Index of power law for the $e^-$ energetic distr.
$N_e^-$	$2.1 \cdot 10^{46}$	Total num. of rel. $e^-$ injected in the cloud
$T_{inj}$	7 d	Duration of the injection
$E_0$	$10^{-6}$ erg	Minimum $e^-$ energy
$E_F$	$5 \cdot 10^{-3}$ erg	Maximum $e^-$ energy

defined as the ratio of photon counts in spectral channels defining the energy range 1.0 to 2.48 keV to the counts in the energy range 0.07 to 1.0 keV. The hardness ratio appears to be roughly constant for most of the observations. For the first and last observations which were obtained at very close to the same radio phase the spectral shapes are identical to within the limits of the data. However, there is a suggestion that the spectrum hardens for the observations at peak X-ray flux at phase 0.48. This occurs at the onset of the second radio outburst.

### 3.2.4 Model fits of the radio light curves

Using the code we have elaborated to compute the model described in Chapter 2 we have fitted the radio light curves at 20 cm and 6 cm plotted in Figure 3.1. Since we didn't have data at 6 cm for the second outbursts we have restricted our fit to the late stages of the rise and to the decay of the first outbursts.

The theoretical light curves for each frequency of the best fit we obtained can be seen in Figure 3.4 together with the points observed.

The parameters introduced into the model to obtain this result are showed in Table 3.3.

The number of protons injected must be equal to the number the electrons injec-

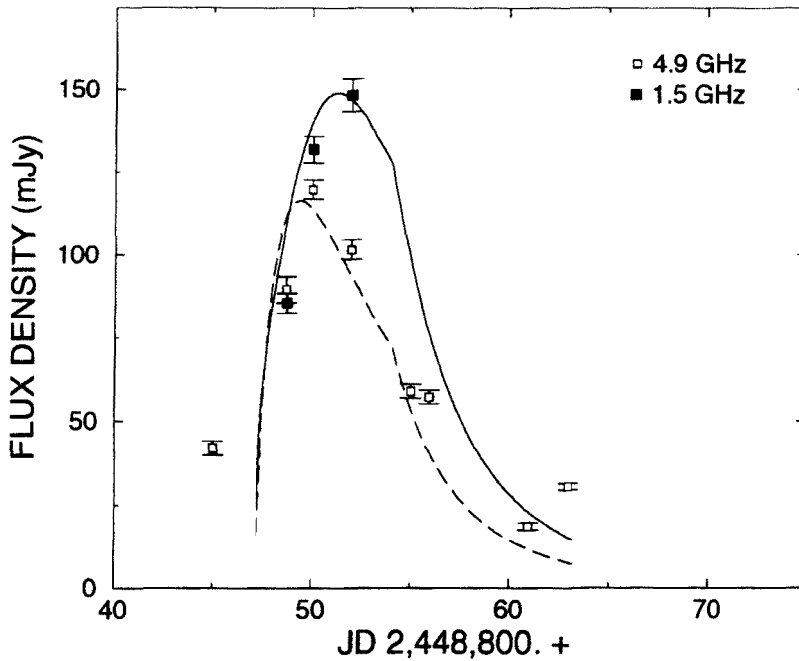


Figure 3.4: Model fit to the outburst observed between JD- 2448840 and JD- 2448860 with the VLA at the frequencies  $\nu = 4.9$  GHz (dashed line) and  $\nu = 1.5$  GHz (solid line).

ted. Therefore, the total mass of the particles transferred in the 7 days during which the injection is taking place is  $\sim 1.8 \cdot 10^{-11} M_{\odot}$ . Since we know there are about 14 outburst in a year, that implies a mass transfer rate of about  $2.5 \cdot 10^{-10} M_{\odot}/yr$ .

### 3.2.5 Inverse-Compton Emission

We have seen in the previous chapter that in the case of a radio emitting system, an alternative method to produce X-ray emission is inverse-Compton scattering. If the relativistic electrons responsible for the radio emission are produced in proximity to the primary, the photons in the radiation field of the primary may be inverse-Compton scattered to X-ray and  $\gamma$ -ray energies.

For inverse-Compton production, the X-ray and radio emission are both linked to the creation of relativistic particles and one might expect that the X-ray outburst would be very nearly coincident with the radio outburst. The fact that our observations show radio and X-ray outburst peaks at nearly opposite phase contradicts



this simple prediction. However, a strict coincidence of radio and X-ray emission is relaxed if the radio and X-ray flux originate from different volumes. To produce detectable, optically-thin radio emission, relativistic particles must either be produced in, or escape to, a region at large radii from the underlying Be star; where they can fill a sufficient volume to be detectable and survive against the high inverse-Compton losses that occur at smaller radii. On the other hand, inverse-Compton X-rays are most efficiently produced close to the star, where the stellar radiation energy density is high.

Paredes et al. (1990) have noted that the phase of peak radio outburst varies from cycle to cycle, lying within the boundaries 0.4 to 0.9. It is striking that the duration of the high state of the X-ray light curve matches the range of phases during which the system is, on average, radio active. Taylor & Gregory (1984) noted that the radio emission from LS I+61°303 is optically-thin during most of the rise of the outburst (as observed during the second outburst in Figure 3.1) and consequently there must be continued particle production during at least the rising portion of the outburst. The detection, on several occasions, of weaker bursts of emission past the main outburst (Taylor et al., 1992), indicates further that relativistic particle production continues well past the time of peak flux density. The data therefore indicate a continuous period of particle production during the active radio interval (phase 0.4 – 1.0). If at least some of this particle production occurs close to the primary star, a continuous high state of inverse-Compton scattered photons would be produced during this phase range. The relative strength and timing of the associated radio activity from cycle to cycle might then depend on additional factors affecting the transport of electrons to large radii.

The constraints on this calculation are the observed properties of LS I+61°303. The primary has  $T_{eff} \sim 26,000$  K and luminosity  $L_*$  about  $10^{38}$  erg/s (Hutchings & Crampton, 1981). From analysis of the multi-wavelengths radio observations (Taylor & Gregory 1984, Paredes et al. 1991) estimate the power-law index of the energy distribution for the injected particles  $p \sim 1.6$ , an initial size of  $10^{12} - 10^{13}$  cm, the magnetic field strength at that time  $B_o \sim 1G$  and a total energy in radio-emitting, relativistic particles of a few  $10^{39}$  erg. The inverse-Compton luminosity also depends on the upper energy limit,  $E_u$ , of the injected particle distribution function. To produce scattered photons with energies above 100 MeV,  $E_u$  must be at least several  $\times 10^{-3}$  ergs (see below). Taking  $E_u = 10^{-2}$  ergs, and placing the site of particle injection at a distance equal to the semi-major axis yields a peak inverse-Compton

luminosity of  $\sim 10^{37}$  erg  $s^{-1}$ . This luminosity is sufficient to explain the flux of high energy photons from LS I+61°303 above 1 MeV, however it greatly exceeds the X-ray luminosity.

### 3.3 Multiwavelength centimetric observations

In June 1994 we tracked a radio outburst of LS I+61°303 during a full 26.5 day cycle at 6 different centimetric wavelengths with the VLA interferometer.

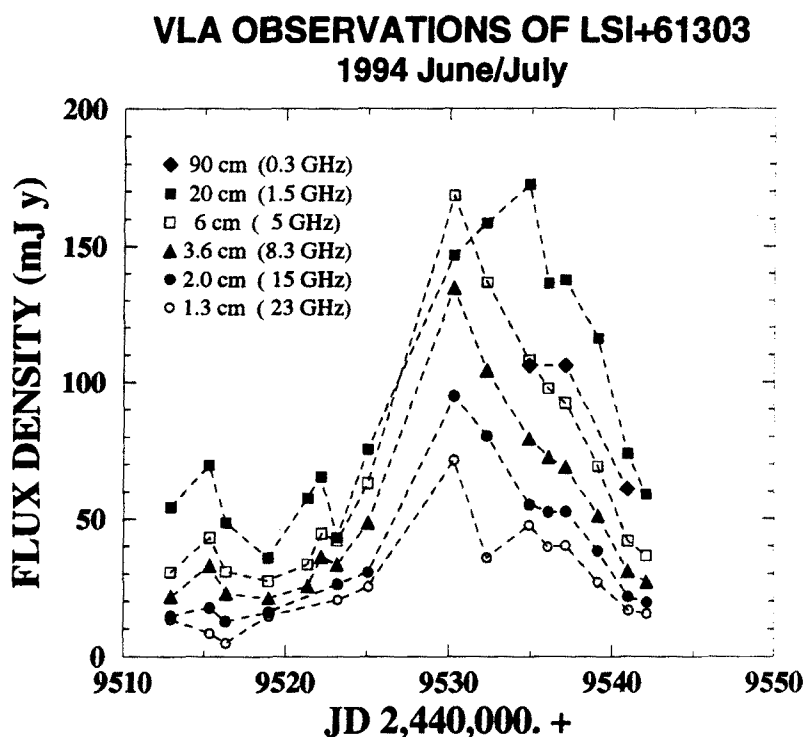


Figure 3.5: The radio flux densities of LS I+61°303 obtained at the indicated frequencies during VLA observations of a whole cycle in June 1994

The light curve observed for each figure is plotted in Figure 3.5.

The overlapping of consecutive outburst observed, specially at low frequencies only allows to perform a reliable fit of the rise and early stages of the decay of the central strong flare. And the model fit we performed is displayed in Figure 3.6. The input parameters of this fit are listed in Table 3.4 they are very similar to the fits of the 1992 observations performed in section 3.2.4.

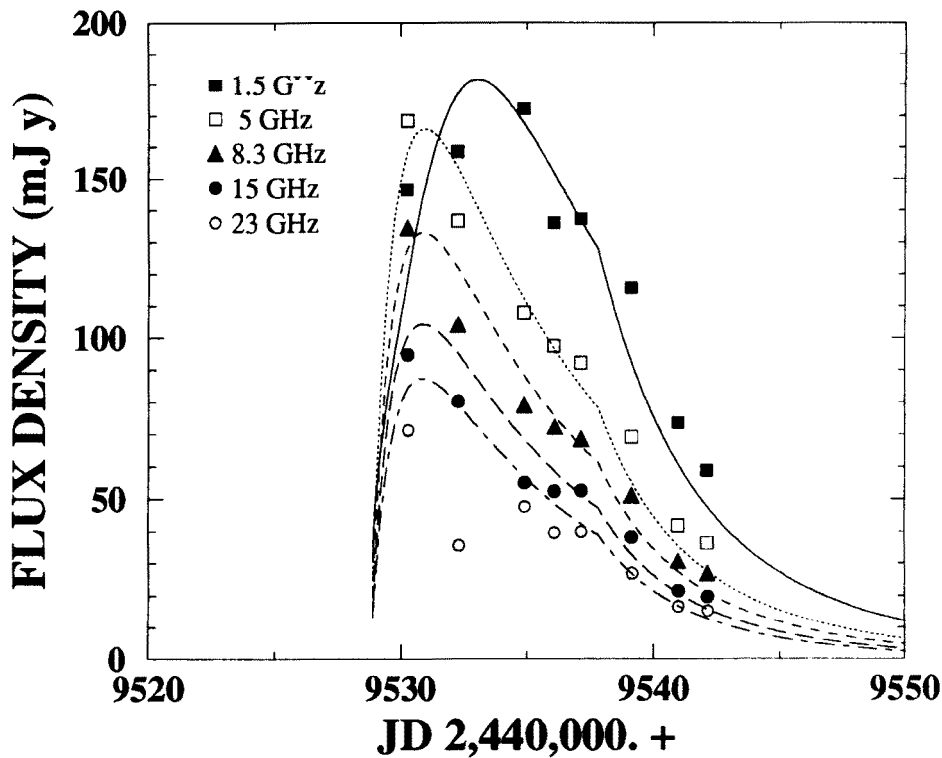


Figure 3.6: Fits to the observations presented in the previous figure of the model described in Chapter 2.

### 3.4 Simultaneous cm-mm observations

We monitored four radio emitting X-ray binaries: Cygnus X-3, SS433, LSI+61°303, and GRS1915+105 with Nobeyama Millimeter Array(NMA) and the 70 m antenna at the MDSCC<sup>c</sup>. We also carried out simultaneous observations of the four sources with the VLA and JCMT at six different wavelengths during two separated sessions.

Some observing parameters are summarized in Table 3.5 GRS1915+105 was under the detection limits in all the observations. For SS433 and LSI+61°303, the VLA-JCMT data on October 1994 can be represented by power laws, as expected from the synchrotron model. For Cygnus X-3 the simultaneous data as well as quasi-simultaneous Madrid-NMA data indicate much flatter spectra than the former two sources. Although it appeared to be in quiescent state, we did see significant variations between 3.6cm and 2mm in two days of VLA-JCMT observations.

<sup>c</sup>Madrid INTA-NASA Deep Space Communication Complex

Table 3.4: Parameters used for the model fit displayed in Figure 3.4

$R_0$	$1.4 \cdot 10^{13}$ cm	Initial sphere radius
$v_{exp}$	$3.5 \cdot 10^7$ cm s <sup>-1</sup>	Expansion velocity
$v_{ejec}$	$1.5 \cdot 10^9$ cm s <sup>-1</sup>	Ejection velocity
$B_0$	0.15 G	Magnetic field at $R_0$
$L_{uv}$	$10^{38}$ erg s <sup>-1</sup>	Luminosity uv photons
P	1.85	Index of power law for the $e^-$ energetic distr.
$N_e^-$	$1.65 \cdot 10^{46}$	Total num. of rel. $e^-$ injected in the cloud
$T_{inj}$	9 d	Duration of the injection
$E_0$	$10^{-6}$ erg	Minimum $e^-$ energy
$E_F$	$5 \cdot 10^{-3}$ erg	Maximum $e^-$ energy

Table 3.5: Observing parameters for simultaneous mm-cm observations

	instrument	wavelengths	int. time
VLA-JCMT simultaneous observations(Oct.14-15,1994)	VLA JCMT(14UKT)	20cm,3.6cm,1.3cm 2mm,1.3mm, 800 $\mu$ m	4min. 30min.
Madrid-NMA monitoring (Oct.1994-May 1995)	Madrid 70-m NMA	13cm, 3.6cm 3.1 - 3.5mm	10min. 20-100min.

In Figure 3.7, we show the model fit to the VLA-JCMT spectra obtained on October 14 and 15. The parameters used for the calculation are taken from the previous observed properties and modeling of these sources (*e.g.* Paredes et al. 1991, Taylor et al. 1992, Seaquist et al. 1982, Martí 1993). The observations of LSI+61°303 were carried out around phase 0.8. The phase of the peak radio outburst lies on average within phases 0.4 to 0.9 (Paredes et al. 1990). Therefore, we have chosen to fit the spectra some time around the peak and 1.5 days after. The size of the region would be about 2.2 AU for the first day and about 2.6 AU for the second one. Although in the case of the spectra of SS 433 we do not have information about the epoch of the onset of the outburst we have also tried to fit an average spectrum for the 2 days. The fit gives an spectral index of  $\alpha = -0.4$  below 8.4 GHz and  $\alpha = -0.6$  above it, which agrees with the general trend observed. The upper limit for the size of the region required to detect the mm-submm emission with the parameters used is about 1.6 AU.

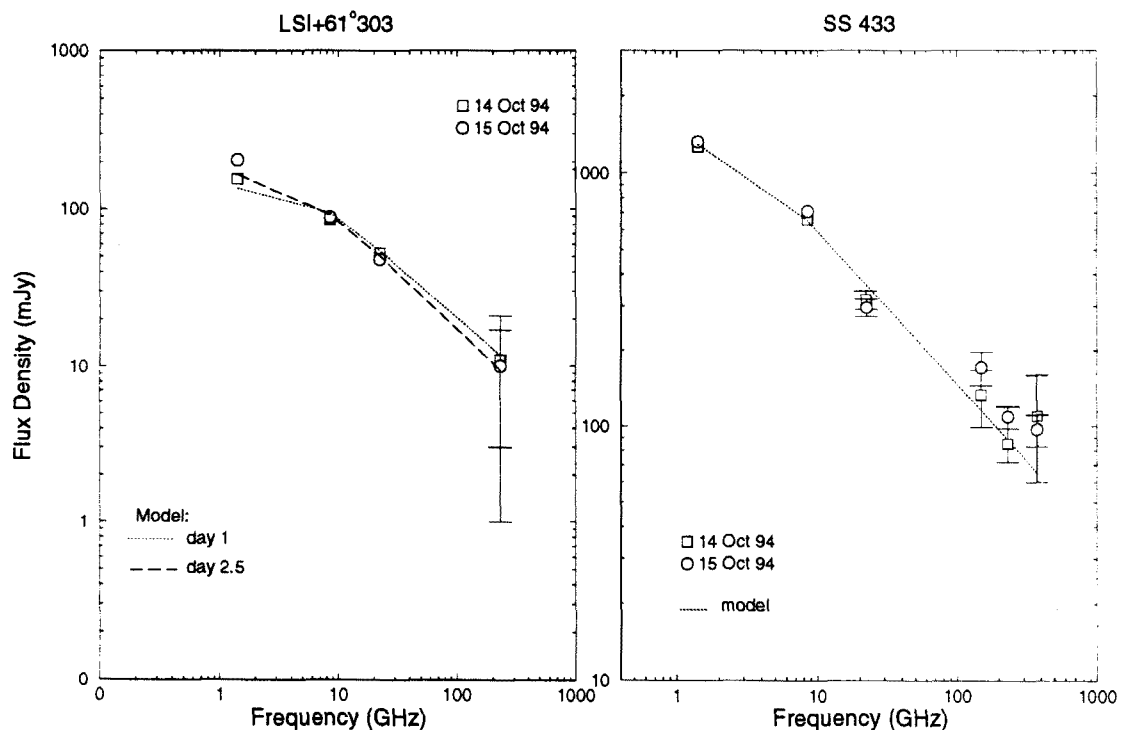


Figure 3.7: Spectra and results of model fits for LSI+61°303 and SS433



**Part II**  
**RADIO IMAGES**





## Chapter 4

# Imaging the milli-arcsecond radio structure of LS I+61°303

### 4.1 Introduction

Since 1978, when LS I+61°303 was discovered to emit in radio wavelengths, few high resolution images of the source have been obtained, and the relation between the outbursts and its structural shape it is not yet clear. The source was observed with VLBI techniques by Lestrade et al. (1988) during its quiescent state (25 mJy) at 1.6 GHz yielding a source size of 4 mas; however, it remained uncertain if such size was due to interstellar scattering. Taylor et al. (1992) observed LS I+61°303 at 5 GHz<sup>a</sup> using the European VLBI Network (EVN), therefore no intercontinental baselines were involved in their interferometric data. Their observations were taken at two different epochs of the same orbital cycle. During the first one (at phase  $\sim 0.56$  of the radio outburst period<sup>b</sup>) the source was in quiescent state, whereas the second session (at phase  $\sim 0.79$ ) took place during a strong outburst. In both epochs the source seems to merely consist of a single compact component. Visibility fits of a single spherical gaussian to the data yields to an angular source size of  $3.2 \pm 0.9$  mas (resolved) for the first session and of  $1.6 \pm 1.2$  mas (unresolved) for the second one.

---

<sup>a</sup>By extrapolating the 1.6 GHz measurements to 5 GHz, a size of 0.4 mas for interstellar scattering is obtained.

<sup>b</sup>Since we assume they are coincident, we will refer to the radio outburst period and the binary orbital period indistinctly. The period used is 26.496 days and the origin of phase is at Julian Date 2443366.775 (Taylor & Gregory 1982).

Massi *et al.* (1993) studied the source also at 5 GHz but with a resolution higher than the previous authors, using intercontinental baselines. Their observations took place at phase 0.7 of the orbital cycle when the source was in a radio active state (200 mJy). They obtained a map showing an elongated structure of about 2 mas. However, fits of the clean components were indicative of the existence of a double source which showed up by convolving them with an underestimated clean beam. The two components appear to be separated by 0.9 mas with an orientation angle of  $\sim 45^\circ$  (from North towards East) and a source overall size of  $\sim 1.6 \times 1.0$  mas. Both, Taylor *et al.* (1992) and Massi *et al.* (1993) have used their VLBI observations to indirectly infer (assuming a given epoch for the onset of the outburst) expansion velocities on milli-arcsecond scales of the order of hundreds of  $\text{km s}^{-1}$ ; this is roughly two orders of magnitude lower than appears to be typical of other X-ray binaries studied with VLBI, which have tended to have velocities  $\sim 0.15\text{--}0.30c$  (Cyg X-3: Molnar *et al.* 1988; SS 433: Hjellming & Johnston 1981), or even greater (GRS 1915+105  $\sim 0.9c$ : Mirabel & Rodríguez 1994, GRO J1655 Tingay *et al.* 1995).

In order to clarify the milli-arcsecond radio structure behaviour of LS I+61°303, and its plausible relation with the phase of the cycle and with the occurrence and strength of the radio outburst peak, it is necessary to keep on studying high resolution images of the source at various phases (radio active and quiescence) and outburst types (strong or weak).

We disposed of two sets of VLBI data of LS I+61°303 taken 1.25 years apart. The first run was on 8 June 1992, at phase 0.4 of the 26.496 radio period. The source radio emission happened to be in a quiescent state; however it presented one of its so called mini-outbursts. Hereafter, these VLBI observations of LS I+61°303 will be referred to as **Run I**. A second VLBI observation campaign of this REXRB was carried out on days 9 and 13 in September 1993, corresponding respectively to phases 0.66 and 0.81 of the same orbital cycle. In this case, phase 0.81 happened to be in quiescence or during the decay towards quiescence, whereas phase 0.66 was near the outburst peak. Hereafter this 1993 set will be referred to as **Run II**.

Therefore, analysis of *Run I* can provide us with information about the milli-arcsecond structure of LS I+61°303 during a mini-flare occurred in between outbursts (quiescent state); whereas analysis of *Run II* can allow us to study for a same orbital cycle the structure at two different epochs or phases, as well as its plausible geometric variations from the state of activity to the state of quiescence.

Table 4.1: Antennas Used in *Run I*

Antenna	Location	Diameter (m)
Effelsberg (B)	Bonn, Germany	100
Haystack (K)	Westford, Massachusetts	37
North Liberty (I)	North Liberty, Iowa	25
Phased VLA (Y)	Socorro, New Mexico	27×25
OVRO (O)	Owens Valley, California	25
Brewster (R)	Brewster, Washington	25

Comparison of the results for the two sets, *Run I* and *Run II*, might provide some knowledge of structural differences between epochs separated about 1/4 of the four year modulation of the radio outburst peak strength.

## 4.2 Observations

**Run I:** The 6 cm LS I+61°303 data gathering intervals of *Run I* took place during about 24 hours (from phases 0.38 to 0.42 of the major outburst cycle) using a six-element global VLBI array. The antennas used are listed in Table 4.1. The data were recorded using the Mk III (mode A) VLBI system (Rogers et al. 1983) and correlated on the Mk III correlator at Haystack Observatory. All antennas recorded both the *RCP* and *LCP* signals incident from the radio source, and both *RR* and *LL* correlations were made. The calibrators observed were 0235+164, 0735+178 and OQ208.

**Run II:** In *Run II* LS I+61°303 was observed with a 7-element VLBI array at 6 cm wavelength, during two different sessions of about 12 hours each. The antennas used are listed in Table 4.2. The data were recorded using the Mark III recording system (mode B) and correlated on the Mark III correlator operated by the Max-Planck-Institut für Radioastronomie in Bonn. Since hardware errors at Westerbork during the whole VLBI session made the observations much less sensitive than normal we have edited out these data. In this case the VLBI calibrator was 0228+673 (4C67.05).

Table 4.2: Antennas Used in *Run II*

Antenna	Location	Diameter (m)
Effelsberg	Bonn, Germany	100
Jodrell2	Jodrell Bank, U.K.	25
Medicina	Bologna, Italy	32
Noto	Noto, Italy	32
Onsala85	Onsala, Sweden	25
VLBA OV	Owens Valley, U.S.A.	25
Phased VLA	Socorro, New Mexico	27 × 25

In both experiments, **Run I** and **Run II**, one of the antennas in the VLB array was the phased VLA (Very Large Array interferometer of NRAO). In addition to using the VLA as a VLBI element, we processed the VLA observations separately to derive integrated flux measurements during each of the VLBI experiments. This provided essentially continuous monitoring of the flux of LS I+61°303 during the VLBI observations. In both runs, the VLA data was calibrated using the standard calibrators 3C48 (0137+331) and 3C286 (1331+305) for the fluxes, and the nearby calibrator 0228+673 for the phases (which was observed prior to each LS I+61°303 scan). Images performed with the visibilities of the each of these VLA sessions are presented and extensively analyzed in Chapter 5 of this work. In the case of *Run II* the Effelsberg antenna was also used to measure the total integrated flux density from the source.

---

\*The NRAO is operated by Associated Universities, Inc., under cooperative agreement with the National Science Foundation

## 4.3 Structure evolution during a LS I+61°303 mini-flare: *Run 1* results

### 4.3.1 *Run 1* data analysis

The measurements made with the VLA during *Run 1* show that LS I+61°303 was experiencing a “mini-flare” during the observing time, with the total flux rising from  $\sim 30$  mJy to  $\sim 35$  mJy and then falling to  $\sim 22$  mJy, as shown in the top panel of Figure 4.1. This represents a substantial variation in the flux density, of the order of 50–60%. This kind of “mini-flares” have been seen in many observations of LS I+61°303 light curves, both between and during the actual periodic outbursts (superposed onto the general trend of the flux density rise and decay). Taylor and Gregory (1984) interpret them as successive events of luminosity driven shocks (LDSs) which produce relativistic particles. Peracaula et al. (1997) have observed a quasi-periodic modulation of about 1.4 hours superposed onto some of these small amplitude radio flares when they occur near the outburst peak (such period analysis is presented in Chapter 9 of this work).

In Figure 4.1 we also plot the amplitudes for the VLBI baselines involving the VLA. As it can be seen there, the amplitudes for individual VLBI baselines appear to track the integrated variations measured with the VLA, suggesting that the variations occurred on VLBI scales. The amplitudes for increasingly shorter baselines (top to bottom panels in Figure 4.1) begin to decay successively later, indicating an expansion in the size of the compact radio structure.

Often, REXRBs might exhibit substantial variations within the several hours that a typical observing run may last. When this happens, it is not possible to use directly the standard CLEAN algorithm to compute maps, since the assumption of a constant brightness distribution is no longer acceptable. Otherwise, these temporal variations could be confused with real spatial frequency variations (i.e. source structure) and wrong conclusions about the source shape could arise.

Therefore, in order to minimize the effect of time variations on our VLBI images, as well as to study the nature of mini-flare events, we divided the VLBI data into five time ranges, during which the total source flux density, as indicated by the VLA observations, was roughly constant. These time ranges, which we refer to as “A-F”,

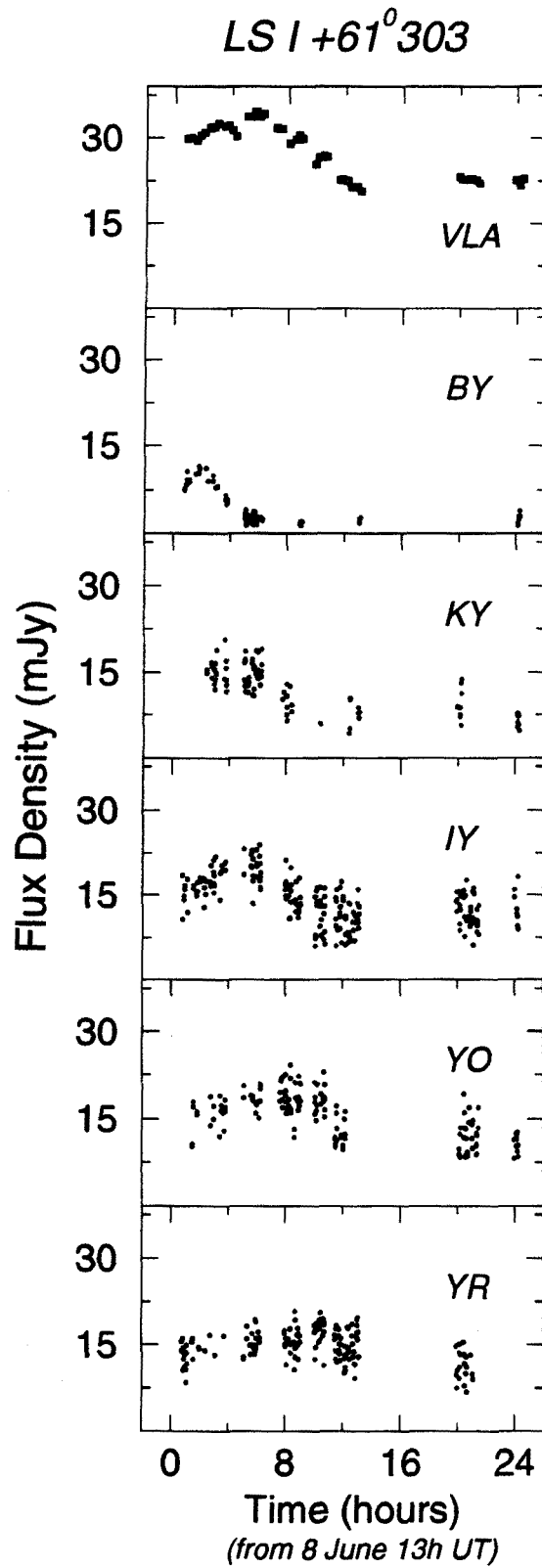


Figure 4.1: Flux measured by the VLA and on the most sensitive baselines of our VLB interferometer (those involving the VLA)

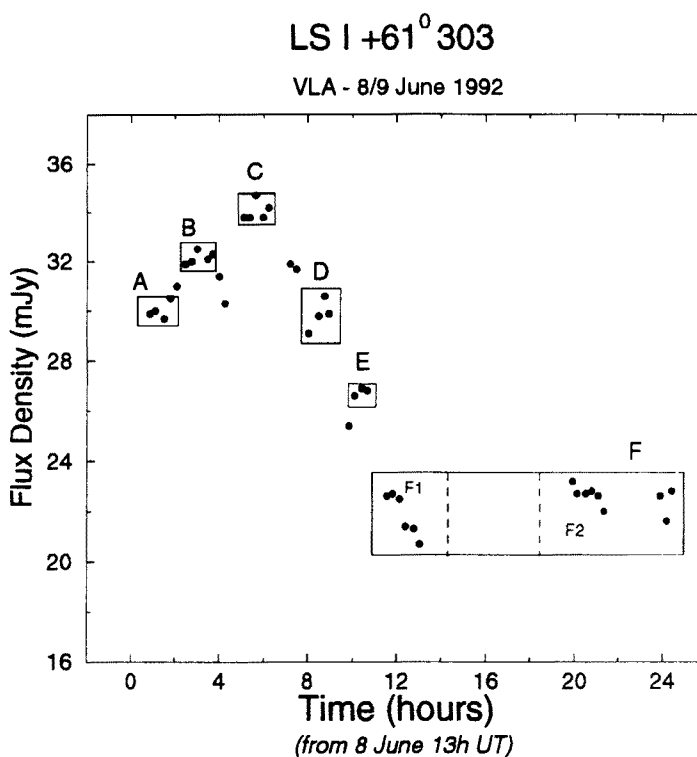


Figure 4.2: Flux variations measured by the VLA during our VLB experiment, with boxes showing the different datasets used to make individual VLBI images during periods when the flux was roughly constant

are shown in Figure 4.2 and they correspond to the flare rise (A and B), the flare maximum (C), the flare decay (D and E), and the post-flare state (F). The several scans showed in Figure 4.2 that do not fall into any of the indicated boxes were not used in our analysis because their integrated fluxes were substantially different from surrounding regions on the integrated flux curve, as well as because they do not provide enough data for an independent analysis.

The  $uv$ -coverages for the entire data set and for each individual time range are shown in Figure 4.3. It is important to notice that the visibilities are distributed along a preferential direction that is rather different for each part (due to the shortness of their sampling time range, the hour angle covered by the rotation is quite narrow). Therefore, the resolution we will have for the images is going to be highly concentrated in one direction which will be different for each part. Figure 4.3 also shows that there are long (transatlantic) baselines for all parts except part E.

Hybrid maps of the distribution of total intensity  $I$  were made using a self-calibration algorithm similar to that described by Cornwell and Wilkinson (1981) in the Brandeis VLBI package (Roberts, Wardle, and Brown 1994). Both  $RR$  and  $LL$

correlations were used to perform the maps. Images for subsets A, B, C, and D are shown in Figure 4.4; there were not enough complete triangles of data in parts E and F for the hybrid mapping process to reconstruct the data phases, and so no maps are shown for these time ranges. In addition, the data were insufficient for us to use amplitude self-calibration during the hybrid mapping. In each of these maps, the restoring beam is shown as a cross in the top right corner of the map: in all cases, the restoring beam was determined by fitting an elliptical gaussian function to the central lobe of the dirty beam.

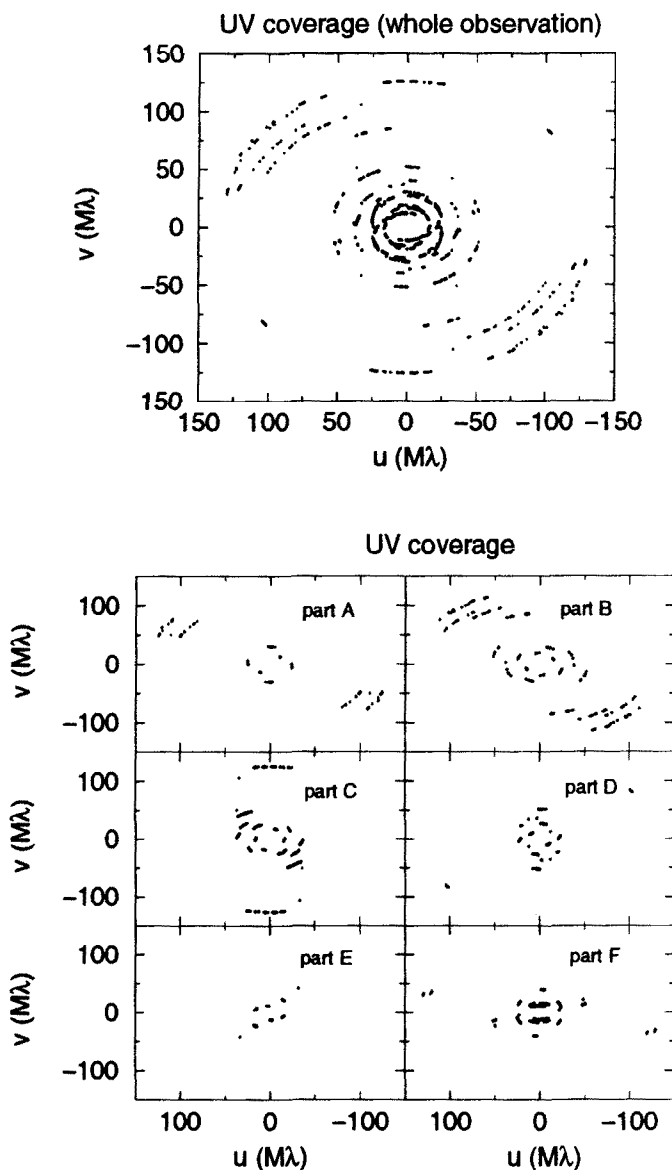


Figure 4.3:  $uv$ -coverages for the entire VLB dataset, and for the separate datasets A–F

Plots of the visibility amplitudes as a function of  $u$ - $v$  distance are shown in



Figure 4.5. As it can be seen from these plots, LS I+61°303 is clearly resolved in all cases. The source structure was also investigated by fitting the complex  $I$  visibilities using a variety of models, as described by Roberts, Gabuzda, & Wardle (1987) and Gabuzda, Roberts, & Wardle (1989). Although for some parts there was evidence that the source structure was made up of more than a single component (see Section 4.3.4), it was not possible to get a unique picture of the alignment direction of the multiple components and the evolution of the source by comparing different time range maps. This is probably due in part to the different directions of maximum resolution for each part; i.e., it may be that in some parts, elongated structure is not seen as clearly as in others, due to the lack of resolution in the direction of the source structure. Thus, the limited  $uv$ -coverage for the individual parts prevents us from determining whether there is elongated structure along a well-defined direction during our observations; in particular, we cannot discriminate if at our epoch LS I+61°303 is extended along structural position angle  $\sim 45^\circ$ , as in the image by Massi *et al.* (1993), taken close to a main outburst maximum.

We concluded that a reasonable approach to investigating the behavior of the radio source during the course of our VLB observations was to fit a single circular gaussian component to the data for each time range in order to obtain an estimate of the size for each part. Because the quantity and quality of phase data (triangles) for the different time ranges was rather non-uniform – in particular, there were not enough closure triangles for parts E and F to calibrate the VLBI phases – we decided that fitting the visibility amplitudes was the best way to obtain a model for the source for every time range in a systematic way, so that they could then be meaningfully compared with each other. The amplitude data for parts A, B, and C are very well fitted both by a single circular gaussian component or by a weak point source plus a circular gaussian component, while parts D and F require both components, the point and the circular gaussian, for a satisfactory fit. The general expression for the function used to fit the data can therefore be written

$$S[\text{mJy}](d) = S_p + S_g \exp(-K d^2)$$

where  $S(d)$  is the visibility amplitude as a function of  $u$ - $v$  distance  $d = \sqrt{(u^2 + v^2)}$ ;  $S_p$  is the amplitude of the unresolved (point) central component, if present; and  $S_g$  is the amplitude of the peak of the circular gaussian component. The constant  $K$  is related to the full width at half maximum (FWHM)  $\phi$  of the gaussian in the visibility plane and the FWHM in the image plane  $H$  by the relations

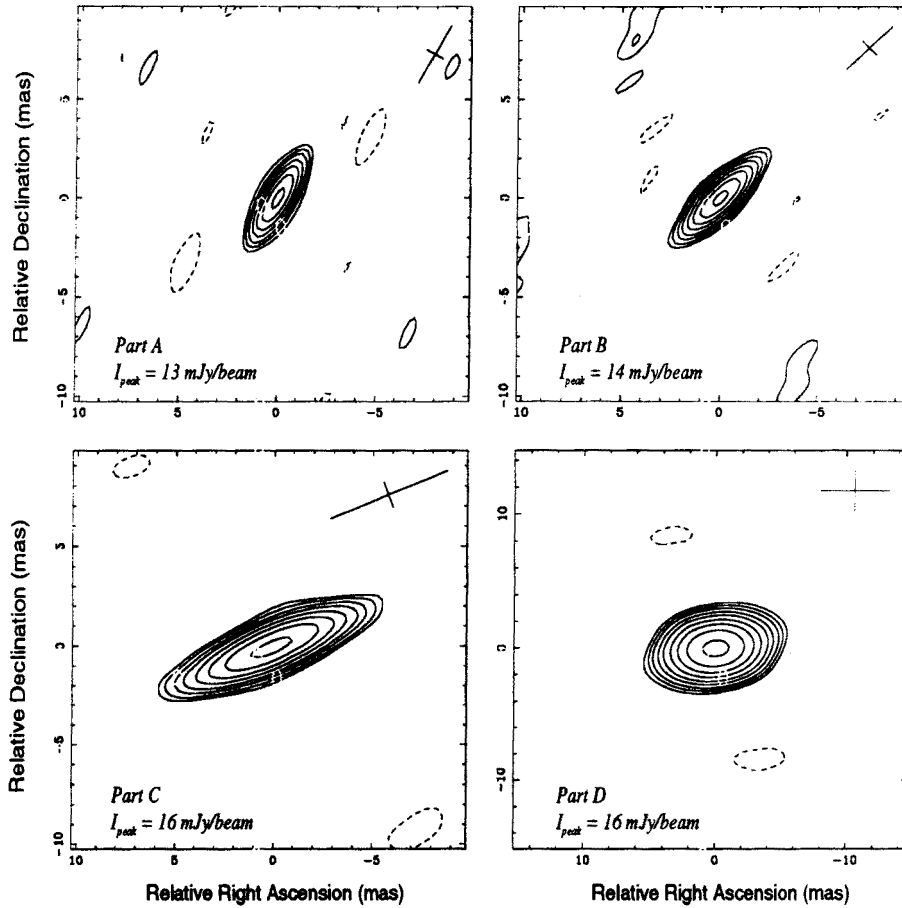


Figure 4.4: Hybrid maps for datasets A–D. In each image, the antenna beam is shown as a cross in the top right corner and the contours go up in multiples of the square root of 2; the bottom contours are 11% (A), 8% (B), 8% (C), and 5.6% (D)

$$\begin{cases} \phi[M\lambda] = \sqrt{\frac{\ln 2}{K}} & (\text{FWHM}) \\ H[mas] = \frac{182.}{\phi[M\lambda]} & (\text{FWHM}) \end{cases} \quad (4.3.1)$$

which are straightly deduced from the Fourier Transform relations between the image and visibility planes (see for example Thompson et al., 1986).

For part E it was not possible to determine the presence or the flux level of the weak point component present in parts D and F, since the absence of long baselines

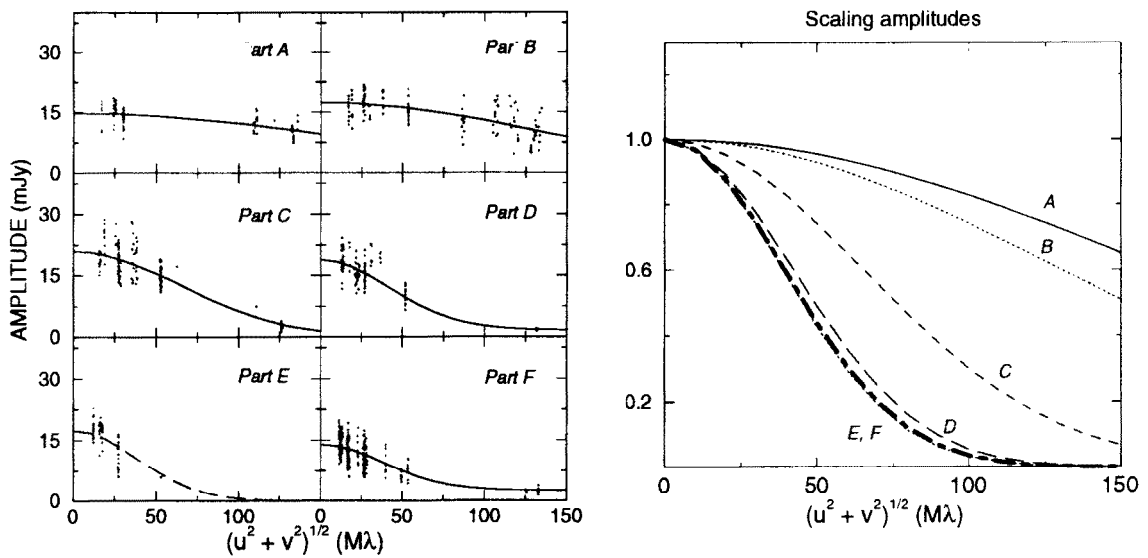


Figure 4.5: Plots of the visibility amplitudes for each dataset (A–F) as a function of  $u$ - $v$  distance. The solid lines overlaid represent circular gaussian plus point (A,B,C, D, F) fits to these amplitudes. The fit for part E is a single circular gaussian represented in dashed lines because of its larger uncertainty due to the lack of data at large  $u$ - $v$  distances. The right panel shows an overlay of the normalized gaussian component of the fits for the different datasets, clearly showing a tendency for the width of the gaussian in the visibility plane to decrease with time, corresponding to an increase of the source size with time

for this time range (see Figure 4.3) does not allow to determine the constant level added to the gaussian fit in the  $u$ - $v$  plane. Although we were able to obtain circular gaussian plus point fits for parts A, B, and C, in these cases, the point component was quite weak; the fits are quite similar to those for a circular gaussian alone. We shall consider the circular gaussian plus point<sup>d</sup> fits for these three parts, in order to treat the data for the different times as uniformly as possible. The resulting fits are shown in Figure 4.5 by the solid lines superposed on the data for each individual part. Due to its separation in time, and in order to see if there had been some evolution, we considered the datasets labeled F1 and F2 in Figure 4.2 independently, and confirmed that the parameters fit for both parts were practically the same; therefore, parts F1

<sup>d</sup>For a practical and physical view of the structure we might call ‘halo’ to the gaussian component or extended component of the fit and ‘core’ to the point or compact component of the fit. However, we must keep in mind that because of the low resolution of the data we can not be sure whether the fits are really describing an halo and a core or they are actually two components separated a distance similar to the size given by the gaussian fit (see section 4.3.4).

Table 4.3: *Run I* gaussian fit to the VLBI amplitudes, sizes, and brightness temperatures

Data set	Time	$S_{VLA}$ (mJy)	$S_g$ (mJy)	$S_p$ (mJy)	$S_{tot}$ (mJy)	$H_{FWHM}$ (mas)	Linear Size (AU)	$T_B$ ( $10^9$ K)
A	0 <sup>d</sup> 14.4 <sup>h</sup>	30.0±0.4	14.3	0.8	15.1±1.0	0.5 ± 0.1	1.2	4.3
B	0 <sup>d</sup> 16.0 <sup>h</sup>	32.2±0.3	16.6	1.0	17.6±0.7	0.6 ± 0.1	1.4	3.5
C	0 <sup>d</sup> 18.7 <sup>h</sup>	34.9±0.4	20.2	1.1	21.3±0.9	1.2 ± 0.2	2.8	1.0
D	0 <sup>d</sup> 21.7 <sup>h</sup>	29.9±0.6	17.1	1.7	18.8±1.0	1.8 ± 0.2	4.1	0.4
E*	0 <sup>d</sup> 23.4 <sup>h</sup>	26.9±0.2	17.5	-	17.5±0.8	2.0 ± 0.4	4.6	0.3
F <sub>1</sub>	1 <sup>d</sup> 01.3 <sup>h</sup>	21.9±0.9	12.0	2.4	14.4±0.9	1.9 ± 0.2	4.4	0.3
F <sub>2</sub>	1 <sup>d</sup> 11.1 <sup>h</sup>	22.6±0.5	11.3	2.6	13.9±0.5	2.1 ± 0.2	4.8	0.2

\*Gaussian+point fit not possible due to lack of data at large  $u$ - $v$  distances

and F2 are shown together as part “F” in Figure 4.5. A summary of the model fit results is given in Table 4.3. In all cases whenever it was possible to obtain circular gaussian fits using phase information as well (parts A, B, C, and D), these were fully consistent with the amplitude fits.

The size of the emitting region and the observed flux density (core plus halo) allow us to determine the brightness temperature using the relation

$$\left(\frac{T_B}{K}\right) = 1.77 \times 10^9 \left(\frac{\nu}{\text{GHz}}\right)^{-2} \left(\frac{S}{\text{mJy}}\right) \left(\frac{\theta}{\text{mas}}\right)^{-2}, \quad (4.3.2)$$

being  $S$  the flux density and  $\theta$  the angular size of the source. By assuming a distance of 2.3 kpc for LS I+61°303 (Gregory et al. 1979) we can derive the linear size and the brightness temperature for each data set (see Table 4.3). If we compare the size obtained,  $\sim 4$  AU, with the semimajor axis of the orbit assuming a  $10 M_\odot$  for the primary B star, 0.40 AU (0.17 mas at 2.3 kpc), we see that the source size is one order of magnitude greater than the binary system separation. The value obtained for the brightness temperature,  $T_B \sim 10^9$  K, is characteristic of non-thermal emission.

### 4.3.2 Rapid expansion during the mini-outburst

We may investigate the evolution of the VLBI structure in LS I+61°303 during this mini-flare by comparing the models obtained for each time period. Figure 4.6 shows a plot of the integrated flux measured by the VLA and the total flux from

the VLBI models in Table 4.3. As it can be seen in this table, the variation in the total fluxes derived from the amplitude fits mimics the integrated variations fairly well, suggesting that the variations measured by the VLA occurred mainly on milli-arcseconds scales. While the fluxes for the halo rise and fall with the VLA fluxes, those for the weak VLBI core monotonically increase during the mini-flare. It is not clear if this is due to (1) an actual growth in the strength of this component, or (2) to the fact that it becomes more visible as the extended component expands. The fact that in many light curves of LS I+61°303 with short sampling time intervals several consecutive or even overlapped mini-flares are seen, suggests us that possibility (1) could be due to the onset of a subsequent mini-flare.

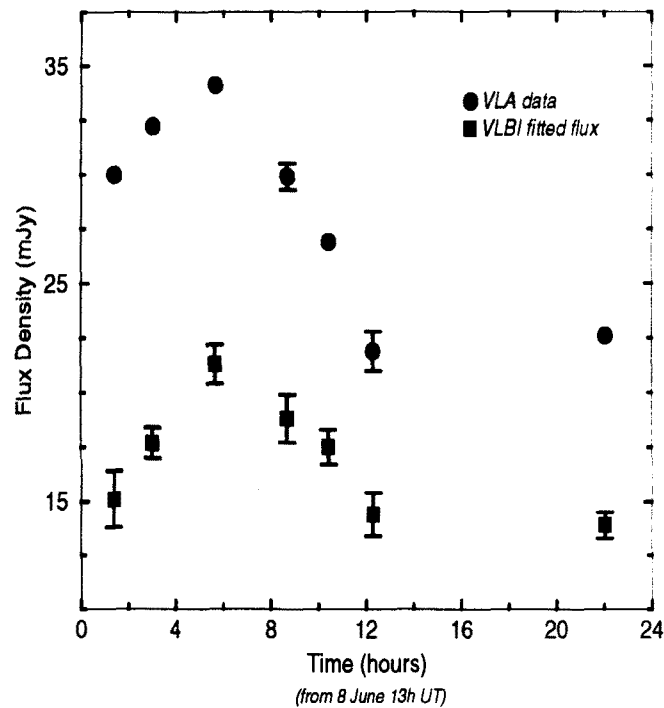


Figure 4.6: Integrated flux measured by the VLA and the total flux contained in our VLBI models. The variations in the total milli-arcseconds scale flux track fairly well the variations measured in the VLA, indicating that these variations occurred basically on the scales measured by our VLB interferometer

In the right panel of Figure 4.5, we have plotted together the gaussian visibility components for each fit normalized to peak amplitude 1 (i.e.  $\exp(-K d^2)$ ). This figure clearly shows a decrease in the gaussian FWHM in the visibility plane (corresponding to an increase of the source size in the image plane) with time for parts A–D. The source size is roughly constant during parts D–F.

Figure 4.7 shows a plot of circular gaussian size  $H$  versus time, where  $0^h$  is arbitrarily set to correspond to the beginning of the observations. The model results for parts F1 and F2 are plotted separately here in order to more clearly show the evolution of the source structure after the burst maximum. This plot indicates that during the flare up to part D, the halo expanded uniformly in time; a linear regression fit indicates the velocity to be  $v = (0.06 \pm 0.01)c$  for a distance of about 3.5 AU. This is the first expansion speed in LS I+61°303 that has been directly measured. Although lower, this velocity is comparable to expansion or ejection speeds measured for other well-studied X-ray binary systems (typically  $\sim 0.15 - 0.3c$ ). As the flare decayed, this enlargement stopped; if the source had continued to extend, this would have been clearly visible in our VLBI data for parts F1 and F2. The formal speed for parts D–F is  $(0.006 \pm 0.006)c$ , consistent with zero. The size of the source in the post-burst period (F1–F2) is  $\sim 2.0$  mas and its flux is  $\sim 14$  mJy. We do not know the reason for this apparent deceleration. One possibility could be that the mini-flare expanded into an evacuated cavity, but then ran into material from a more slowly expanding major eject when it reached a dimension of  $\sim 2.0$  mas. (Taylor *et al.*, 1992 and Massi *et al.* 1993, report a size of about 2 mas some days after the peak of major outbursts). Another possibility could be that a sudden drop in the opacity of the growing source when it reaches the dimension of 2 mas reduced the intensity of the outer parts below our detection level. In that case the braking of the enlargement would be apparent.

### 4.3.3 The flux on intermediate scales

Table 4.3 also indicates the flux measured by the VLA and the difference between this integrated flux and the total flux in the VLBI model. This flux difference indicates the amount of flux inferred to be on scales intermediate between those sampled by the VLB array and by the VLA. Figure 4.8 shows a plot of this intermediate scale flux as a function of time. It is interesting that during parts A–F<sub>1</sub> (or A–E), there appears to be a linear decrease in the inferred intermediate-scale flux; the inferred intermediate-scale flux is roughly constant for parts E–F. There are essentially two possible origins for such a trend: (1) it could represent a real physical decrease in the observed flux on intermediate scales, or (2) it could represent the inaccuracies in our models for the flux observed on VLBI scales. Since it seems somewhat unlikely that model inaccuracies would manifest themselves in such a systematic way, it seems more likely to us that the linear decay in the intermediate-scale flux shown

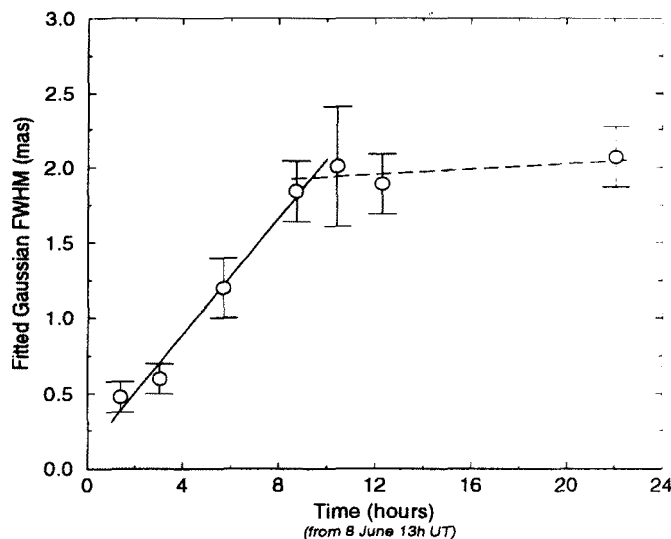


Figure 4.7: Size of the circular gaussian components from Table 2 as a function of time. During the mini-flare, the source size grows linearly with  $v = (0.06 \pm 0.01)c$  up to parts D–E (the mini-flare decline), then stays constant for the remainder of our observing period

in Figure 4.8 represents an actual physical decrease in the flux on scales larger than those sampled by our VLB interferometer, but contained within the VLA core. One natural possibility is that this flux decay is associated with earlier variations in LS I+61°303, since we have no information about the time dependence of its flux prior to the onset of our VLBI observations.

#### 4.3.4 Discussion: single or double structure?

In general, the picture described above –a uniformly expanding circular halo on VLBI scales corresponding to the mini-flare detected with the VLA– fits the VLBI observations well. It gives a relatively simple, physically reasonable, and complete explanation of the observed changes in the VLBI source structure, within the constraints of the data available. Nonetheless, we have some evidence that the VLBI source structure may have been more complex, in particular, that it may have had a double structure. This evidence comes primarily from the VLBI data for part C, corresponding to the mini-flare maximum. We had a relatively large number of VLBI data points for this part, and a relatively large number of intact closure triangles for the hybrid mapping. Model fitting indicates that a two-component model to the

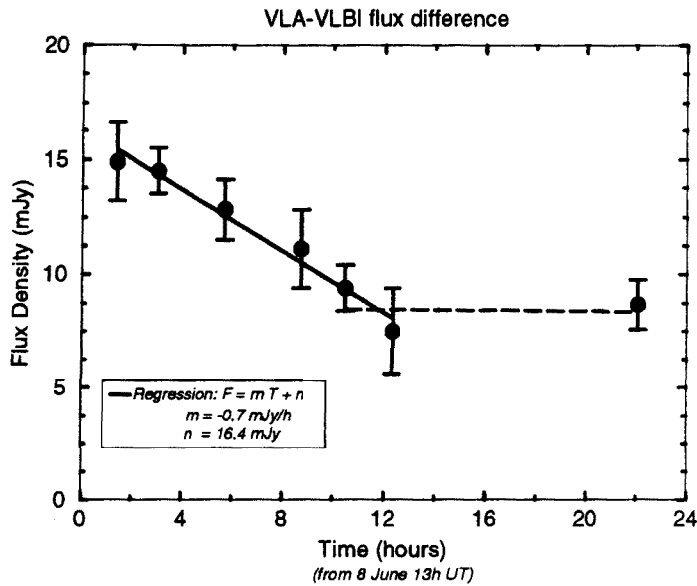


Figure 4.8: Difference between the flux measured in the VLA core and the total flux measured on VLBI scales as a function of time. The clear trend for this “intermediate-scale” flux to decrease during the flare is puzzling; after the flare, the inferred intermediate-scale flux remains constant

part C data (with either points or gaussian components) renders a very good fit to both the amplitudes and phases.

Figure 4.9 shows plots of the model and data visibility phases and amplitudes for part C for the best-fit models with (a) a single circular gaussian, (b) two point components, and (c) two circular gaussian components. In each case, the data have been projected onto structural position angle  $-21^\circ$ , which is the position angle corresponding to the double structure indicated by the two-point fit. As it can be seen, all three models fit the visibility amplitudes well, but the double models clearly fit the visibility phases much better than the circular gaussian model. The double separation and total flux for the two-gaussian fit (1.3 mas and 19.8 mJy) are virtually identical to the size and total flux for the single circular gaussian fit to the amplitudes (1.2 mas and 21.3 mJy), giving us confidence that our analysis based on circular gaussian fitting of the visibility amplitudes renders reasonable estimates for the expansion speed of the VLBI source size during the mini-flare, even if the actual source structure may be more complex. This possibility also implies that the increasing size observed could correspond to a separation velocity of the components forming the complex structure.

We also tried to obtain double fits to the remaining datasets (A, B, D, E, F).



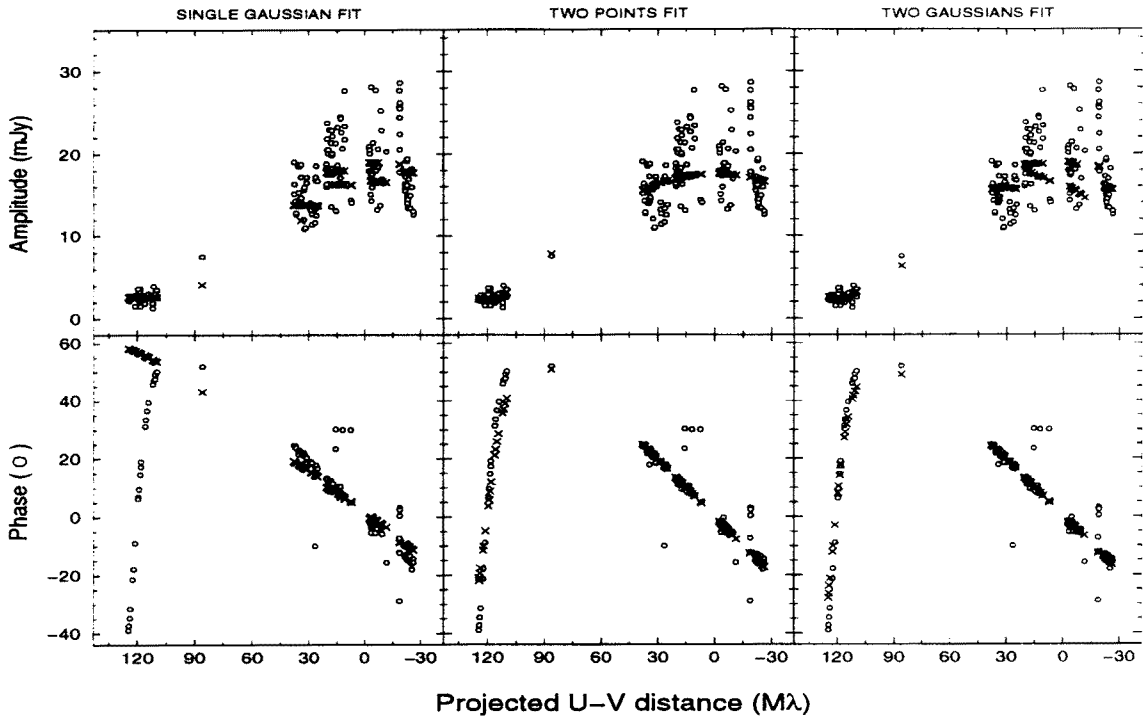


Figure 4.9: Plots of the visibility phases and amplitudes for part C projected onto structural position angle  $-21^\circ$ , together with the visibilities predicted by (a) the best-fit single circular gaussian component, (b) the best-fit point double model, and (c) the best-fit circular gaussian double model. In all three sets of plots, the open circles represent the data and the crosses the model visibilities. The angle onto which the visibilities have been projected corresponds to the structural position angle for the point double model. The visibilities have also been shifted by a small amount so that the stronger component of the point double model is located at (0, 0). The double models clearly describe these data rather well, but are difficult to interpret together with the data for other times during the flare

For cases A and B the fits are satisfactory but do not significantly improve the circular gaussian fit. Case D behaves very similar to C: the two component models fit the visibility phases much better than the circular gaussian model. The alignment angle of the two components ( $-10.3^\circ$ ) slightly differs from case C. The fact that we do not have closure phases for parts E and F does not allow us to obtain phase fits giving information about the orientation of possible elongated structure in the source. Nonetheless, we note that the amplitudes for part F can also be well fit with a double model or elongated elliptical gaussian model. Since there are no data at large  $u-v$  distances for part E, the significance of multiple-component fits to these data is rather low compared to other parts. The fitting of models with multiple components is complicated by the fact that the  $uv$ -coverages – and therefore, the directions of

maximum resolution – for the different parts are quite different. This could explain why we obtain slightly different structural position angles for the double fits for parts C and D. We can understand these results in terms of two possible behaviors a) or b) for the expansion associated with the mini-flare, being:

- a) We are seeing a more or less spherically symmetric expanding source (halo):  
When the source becomes sufficiently resolved, however, we see apparent structure along the preferred resolution direction, due to the limited  $uv$ -coverage. For our data, this would be the case for times corresponding to part C and later.
- b) We are seeing enlargement of the source along a welldefined direction  $\sim -20^\circ$  (such as a double source with a relative separation velocity between the two components). For some parts (A, B), the double structure could not be clearly seen due to lack of resolution along the direction of the structure. We could see the double structure in other parts (C, D) where the direction of maximum resolution better coincided with the direction for the source structure.

In conclusion we are confident that mas structural variations have been detected in LS I+61°303. The analysis precludes however to discriminate between uniform and jet-like expansions. Nevertheless, a bipolar expansion model is found to fit extremely well the visibility data during some particular data sets.

## 4.4 Structure evolution during a LS I+61°303 strong outburst decay: *Run II* results

### 4.4.1 *Run II* data analysis

The observations of LS I+61°303 in *Run II* were carried out during two sessions at two different orbital phases (0.66 and 0.81) of a same cycle, in order to obtain a direct estimation of the projected possibly existing expansion velocity as well as the possible geometrical variations. From the known average radio light curves of LS I+61°303 for the active phase and the quiet phase (Paredes et al. 1990), the observing dates could be selected to coincide with the active and the decaying part of the radio outburst<sup>e</sup>.

The radio light curves of LS I+61°303 during the two observing sessions measured with the VLA and the Effelsberg antenna are shown in Figure 4.10. As it can be seen, during the first session (September 9, top panels) the flux density varies significantly, rising from  $\sim 80$  mJy to  $\sim 130$  mJy and then falling to  $\sim 75$  mJy within the about 12 hours the data gathering took place. Although we do not know the behaviour of the emission during the hours before and after these observations, we suspect, from the shape and time amplitude of this radio light curve, that we were observing another of the LS I+61°303 mini-outbursts superposed onto the strong periodic radio outbursts. If that was the case, this time we were detecting a LS I+61°303 mini-flare when the source was in an active state, as opposed to the observations of *Run I* when the mini-flare took place in a quiescent state. The bottom panels of the plots in Figure 4.10 show that during the second session (September 13) the flux density of LS I+61°303 was very stable, at a level of 60 mJy.

From Figure 4.10 we can also see that the VLA got in the experiment a bit later than the Effelsberg antenna. It is also obvious from these plots that the flux level of the source detected by the two telescopes was coincident during the span of time they were observing simultaneously. Therefore, the flux density variations we observed are at least contained within the VLA sampling resolution (i.e. few arcseconds).

Because of the different radio flux density behaviour of LS I+61°303 during the

---

<sup>e</sup>The peak of the radio outburst usually occurs in the range of phases from 0.4 to 1.0 although with apparent concentration around phase  $\sim 0.6$  for the strongest peaks (Paredes et al. 1990)

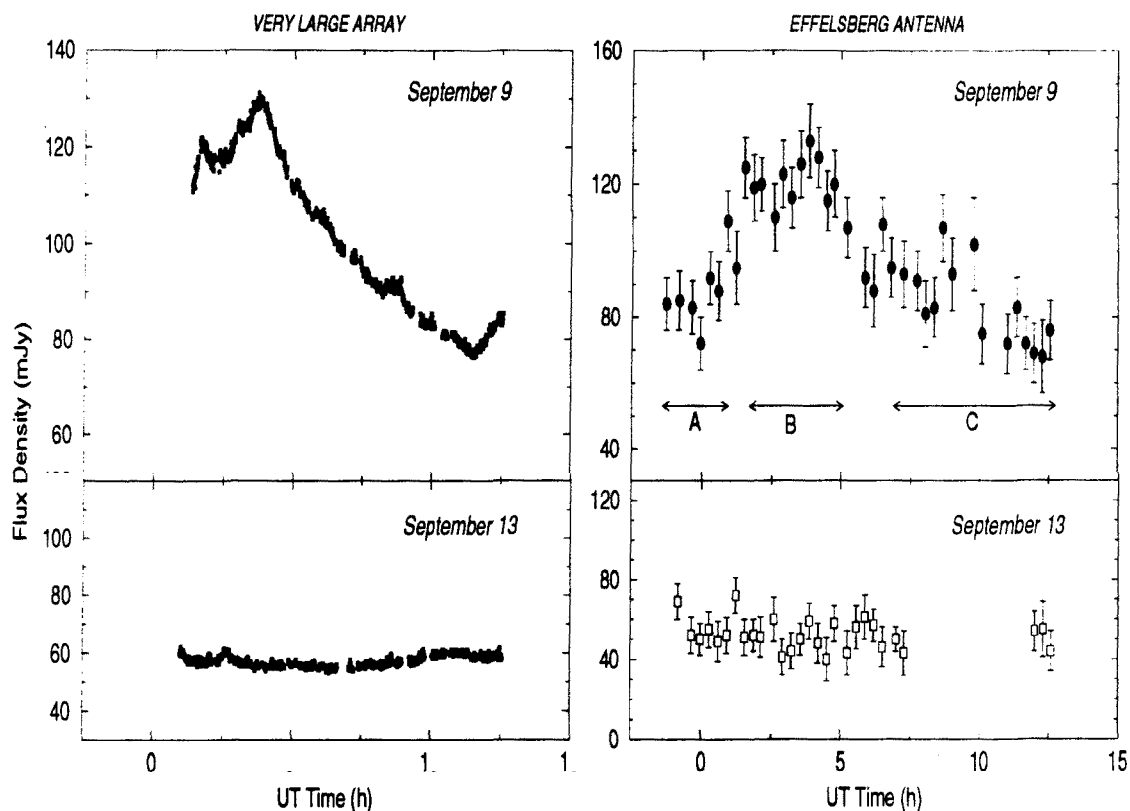


Figure 4.10: Flux density variations of LS I+61°303 obtained during the two observing sessions 1993 September 9 (*Upper panels*) and 1993 September 13 (*Lower panels*). The left plot corresponds to the VLA measurements. The rms of each data point is usually 1 mJy or less. The behaviour of the data respect with time is thoroughly discussed in Chapter 9 and in Peracaula et al. (1997). The plot on the right corresponds to the Effelsberg antenna measurements. The horizontal arrows show the different datasets in which the emission level could be considered constant during the September 9 session.

two sessions of *Run II*, we are going to describe the analysis of the source structure for each of them separately:

### September 9:

Due to the substantial flux density variations of LS I+61°303 during this session it was not possible to use the whole data set to obtain a unique image. Therefore, in order to minimize the effect of time variations, we had to act as we did for the mini-outburst observed in *Run I* (analyzed in section 4.3.1). For this session we segmented the VLBI data in three sets, with reliable flux density stability in each of them. The time ranges of each dataset are shown in the right top panel of Figure 4.10, and we will refer to them as Part A, B and C. The  $uv$ -coverage for each dataset

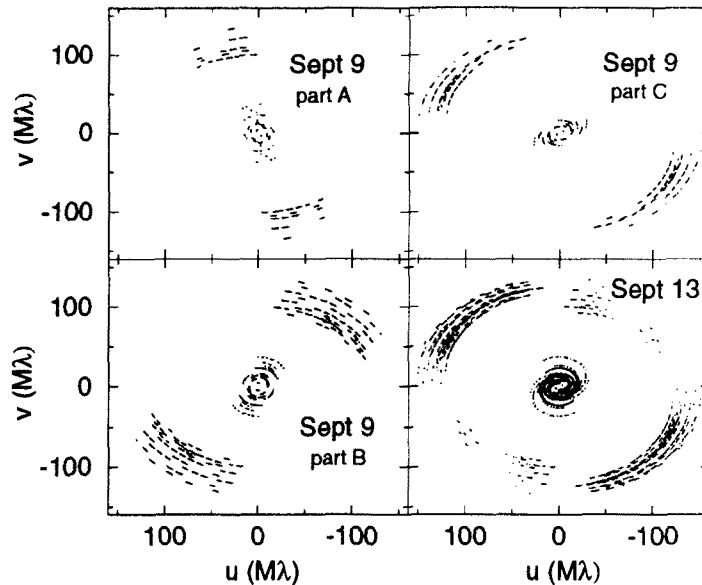


Figure 4.11:  $uv$ -coverage for the separate VLB datasets A, B and C of September 9, and of September 13.

are shown in Figure 4.11. As it happened with the segmented data of *Run I*, the visibilities are distributed along a preferential direction that is different for each part so the resolution of the corresponding image will be highly concentrated in a different direction for each of them.

Therefore, this limited  $uv$ -coverage of Part A, B and C of September 9 and its high directivity prevented us again from reliable hybrid mapping, thus the model fitting techniques described in section 4.3.1 were used on the visibility data. In Figure 4.12 the amplitude versus baseline spacing is shown for each of the three data sets. A filled circle in each plot, at zero spacing, marks the Effelsberg total flux, representing the upper limit to the flux density of the milli-arcsec VLBI structure. The best fit for all three data set was that of a core-halo structure, with an halo size of  $\sim 3$  mas and the unresolved core contributing for at least one fourth ( $1/4$ ) of the total flux. The relations describing such model have been given in Equation 4.3.1. The fitted values are given in Table 4.4 and the best fit curve is drawn as a solid line in Figure 4.12. In this case the size obtained,  $\sim 6$  AU is about a factor 15 greater than the binary system separation. We also have determined the brightness temperature using the relation 4.3.2, obtaining an average of  $T_B = 7 \times 10^8$  K, therefore we are very likely seeing non-thermal emission.

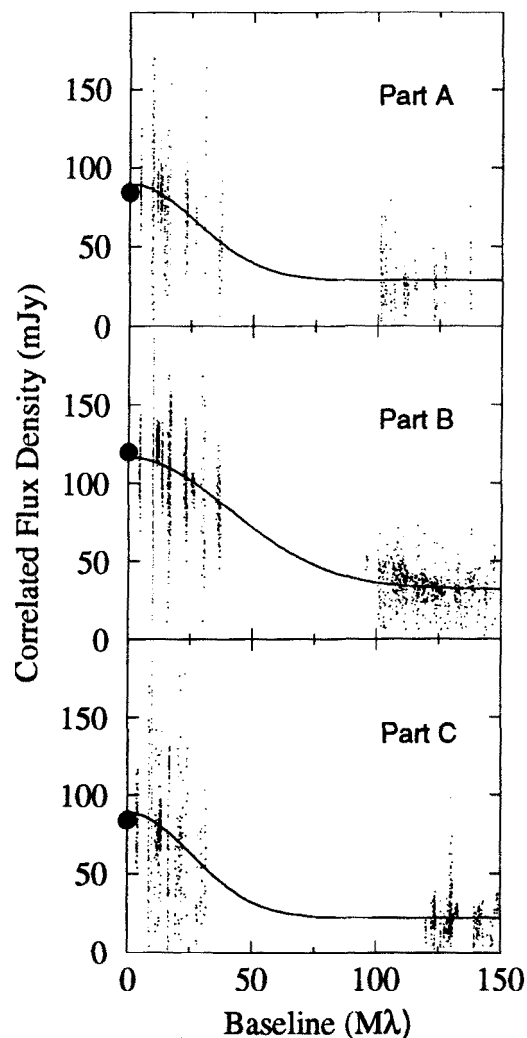


Figure 4.12: Correlated flux density as a function of baseline for each dataset of September 9. The solid lines represent the fit of a circular gaussian halo plus an unresolved core to the data. The filled circle at 0 spacing for each data set represents the total flux as measured by the Effelsberg antenna.

Table 4.4: *Run II* Measured mean flux densities, sizes and brightness temperatures

Date (1993)	Radio Phase	Dataset	Unresolved Core		Gaussian Halo		Brightness Temperature ( $10^8$ K)
			Flux Density (mJy)	Flux Density (mJy)	FWHM (mas)	Linear Size (AU)	
September 9	0.66	A	29	60	3.0	6.9	7.0
		B	30	84	2.5	5.8	12.9
		C	22	67	3.0	6.9	7.0
September 13	0.81		26	25	6.0	13.8	1.0

**September 13:**

The flux density stability along all the second session allows us to use the whole data set and, therefore, to have enough  $uv$ -coverage to attempt reliable hybrid mapping. Such  $uv$ -coverage is shown in the bottom right corner of Figure 4.11. Nonetheless, before mapping, in order to apply the same technique as in the first session, we fitted a core-halo structure to the data. The best size and flux density fit values obtained are also reported in Table 4.4, together with the derived linear size and brightness temperature. We can see in this table that the flux is equally distributed between the resolved and the unresolved components. In Figure 4.13, we display the correlated flux density versus baseline, being the solid line the best fit.

The hybrid map was made using, independently, both the NRAO AIPS and the Caltech DIFMAP packages, obtaining nearly identical results. The final VLBI map, restored using a clean beam of  $1.54 \times 1.15$  mas (PA= $-57.2$ ) is shown in Figure 4.14. The map exhibits an extended structure of about 6 mas, and an unresolved component at the center of the extended structure. The total flux of the map is 50 mJy. The VLA flux density for this epoch is  $\sim 10$  mJy greater than this value. This implies the presence of a larger structure not sampled with our VLBI spacings.

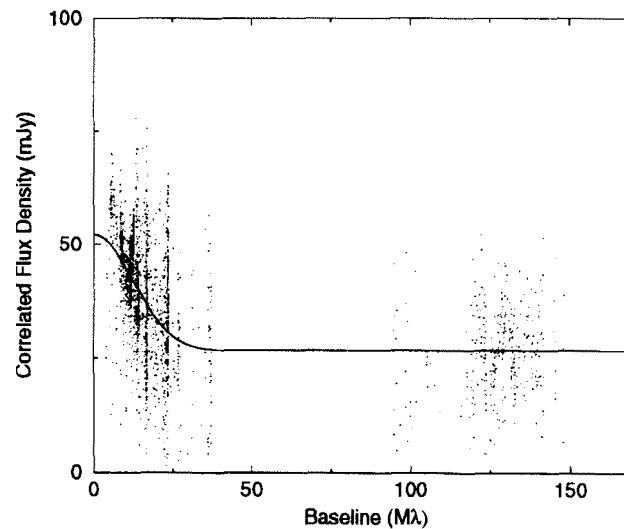


Figure 4.13: Correlated flux density as a function of baseline for September 13. The solid line represents the fit of a circular gaussian halo plus an unresolved core to the data.

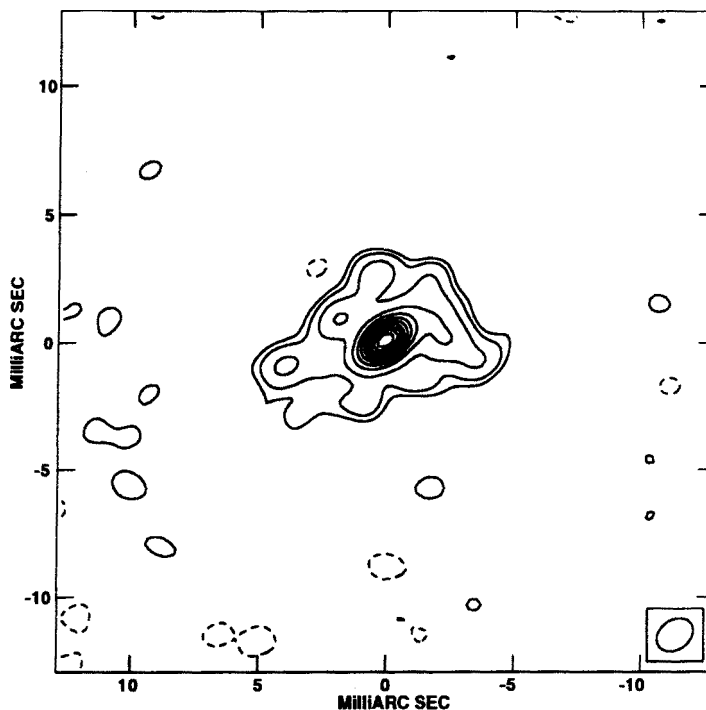


Figure 4.14: Hybrid map of LS I+61°303 obtained from data of 1993 September 13. The restoring beam  $1.54 \times 1.15$  mas at  $57.2^\circ$  is shown as a ellipse in the lower right corner. The map peak is 16.8 mJy/beam. The contour levels displayed are: -3, 3, 5, 10, 20, 30, 40, 50, 60, 70, 80 and 90 % of the peak.

#### 4.4.2 Discussion: Expansion velocity during the decay of a radio outburst

The halo component of the source, of a size of 3 mas in the first session and 6 mas in the second is clearly resolved in both epochs. The fact that the wavelength dependence of the interstellar scattering would predict at our observing frequency a scattering size of 0.4 mas, together with the difference in size measured at high and low radio emission phase, rules out interstellar scattering as the cause of the source appearing extended. The map of LS I+61°303 obtained at phase 0.7 by Massi et al. (1993), shows that the radio emission is mostly concentrated in a 2 milli-arcsecond double or core-halo source of 200 mJy. The phase and flux density in the first epoch of *Run II* are very similar to those of Massi et al. (1993) and the estimated 3 mas size is in agreement with their map. If we compare the structure of the two epochs of *Run II* we can see that the compact component presents the same flux density in both sessions, while the resolved component has enlarged in size from 3 to 6 mas and decayed in intensity from  $\sim 70$  to 25 mJy within the four days that separate



the sessions. Up to 10 mJy of this final extended low level emission could come from larger size scales, not sampled by our interferometer, but with the VLA and the Effelsberg antenna. As our observations were carried out at radio phases 0.66 and 0.81, with an average flux density of 100 and 60 mJy respectively, it is clear that we observed the active and decaying part of the radio outburst. The increase in size and the simultaneous decay in intensity agree with the expected behavior of an optically thin cloud of relativistic electrons expanding adiabatically.

From the source size estimated at each phase of this *Run II*, we can deduce directly the projected expansion velocity, which results to be  $\sim 0.01c$  or  $3000 \text{ km s}^{-1}$ .

## 4.5 Conclusions from *Run I* and *Run II* results

From the just presented VLBI observations of LS I+61°303 during different states of its radio emission we want to remark three main conclusions:

- a) In two independent occasions we have detected **evidences of  $\sim 0.01c$ – $0.1c$  enlargement velocities**:

The values of  $0.01c$  and  $0.06c$  are lower but comparable to the those observed in the radio emission of other X-ray binaries (and normally related with either expansion or plasmon ejection speeds) such as SS433 and Cyg X-3. In addition, they are roughly one and two orders of magnitude greater than the inferred speeds by Taylor et al. (1992) and Massi et al. (1993) for major periodic outburst of LS I+61°303. A possible explanation for that difference might be the fact that these authors used indirect arguments for their speed estimations, which assumed that the material they observed had been ejected a certain number of days before. They also assumed the expansion had maintained a constant speed during these days. Therefore, the slower velocities they inferred could be an average of much higher initial speeds that subsequently decelerated, similar to the behavior during the smaller outburst we have analyzed here; it is also possible that the material seen by them was associated with ejections from smaller flares that occurred *after* the dates they estimated for the onset of the major outburst.

The  $3000 \text{ km s}^{-1}$  and  $18000 \text{ km s}^{-1}$  expansion velocities measured directly from our VLBI observations are consistent with the supercritical accretion model

proposed by Taylor & Gregory (1984), which predicts that radiating electrons must travel outward from the system at velocities in excess of  $1000 \text{ km s}^{-1}$  in order to avoid catastrophic inverse Compton losses by nearby optical primary photons.

- b) During the observations taken when LS I+61°303 was in a quiescent state or near it, an amount of about 10 to 15 mJy was not located on milli-arcsecond scales but on scales intermediate between those sampled by the VLB interferometer (few mas) and the VLA ( $\sim 0''.1$ ). Therefore, this represents an indirect **evidence of radio structure at.  $\lesssim 0''.1$  level.** We think observations of LS I+61°303 with an instrument of this resolution such as MERLIN are necessary to directly observe this extended feature.

On the contrary to the non-active states, during the first session of *Run II* (near the outburst peak) all the emission detected in the VLBI scales seemed to coincide with the flux density measured by the lower resolution instruments VLA and Effelsberg antenna.

- c) The detection of compact (mas-scale) flaring radio emission in LS I+61°303 at an epoch that clearly is not near a major outburst peak indicates that between outbursts the radio emission of this source may have a different origin than during them, i.e., **the quiescent radio emission of LS I+61°303 may not be simply related with the slow decay of the radiation from the major outbursts.** This is consistent with a scenario in which the **inter-outburst flaring radio emission of LS I+61°303 is associated with the overlapping of series of small events**, for example, from luminosity-driven shocks.

On the other hand, from the shape of the light curve observed on *Run II* at phase 0.66, we suspect that during this active state we were observing another one of the mini-flares that superpose onto the radio light curves profile of LS I+61°303. If that is the case we have not detected expansion velocities that could be associated to that particular mini-flare (we remind that the size fits to the visibilities corresponding to the three subsets of the September 9 1993 session was the same, within the errors, for each of them). We have seen, on the contrary, that during the mini-flare observed in quiescence in *Run II* a rapid speed ( $0.06c$ ) is observed. Such comparison might indicate that the structural velocity observed during this *Run II* mini-outburst is not associated to the same fact that causes the short flare, and that possibly the velocity inferred

from the 5 subsets of the data of June 8 1992 is due to having observed a part of the decay of a strong outburst or maybe the onset of the following one. Therefore we think **large velocities are not associated to mini-flares themselves but to the strong periodic radio outbursts.**



# Bibliografy

- [1] Cornwell T.J., Wilkinson P.N., 1981, MNRAS 196, 1067
- [2] Gabuzda D.C., Roberts J.F.C. & Wardle 1989, ApJ 338 743
- [3] Gregory P.C., Taylor A.R., Crampton D., et al., 1979, AJ 84, 1030
- [4] Hjellming, R.M., Johnston, K.J. 1981, ApJ 246, L141
- [5] Lestrade, J.-F., 1988, in *The Impact of VLBI on Astrophysics and Geophysics*, M.J. Reid and J.M. Moran Eds., Kluwer, Boston, 265
- [6] Massi M., Paredes J.M., Estalella R., Felli M., 1993, A&A 269, 249
- [7] Mirabel I.F., Rodríguez L.F., 1994, Nat 371, 46
- [8] Molnar, L.A., Reid, M.J., Grindlay, E.J. 1988, ApJ 331, 494
- [9] Paredes J.M., Estalella R., Rius A., 1990, A&A 232, 377
- [10] Peracaula M., Gabuzda D.C., Taylor A.R., 1997, A&A (submitted)
- [11] Roberts D.H., Gabuzda D.C., & Wardle J.F.C. 1987, ApJ 323, 536
- [12] Roberts D.H., Wardle, J.F.C., and Brown, L.F. 1994, AJ 427, 718
- [13] Rogers A.E.E., Cappallo R.J., Hinteregger H.F., et al., 1983, Sci. 219. 51
- [14] Taylor A.R., Gregory P.C. 1982, ApJ 255, 210
- [15] Taylor A.R., Gregory P.C. 1984, ApJ 283, 273
- [16] Taylor A.R., Kenny H.T., Spencer R.E., Tzioumis A., 1992. ApJ 395, 268
- [17] Thompson A.R., Moran J.M., Swenson G.W. (1986): *Interferometry and Synthesis in Radio Astronomy* (Wiley, New York).

- [18] Tingay S.J., Jauncey D.L., Preston R.A., Reynolds J.E. et al., 1984, Nature 374, 141

## Chapter 5

# Deep VLA images of LS I+61°303: search for associated extended radio emission

### 5.1 Introduction

Our goals in this chapter is to map and to study the field around LS I+61°303 in order to check the possible existence weak extended radio emission associated with this source. The motivation for this kind of search came from previous reports of non-thermal extended radio emission related to a handful of well known REXRBs, as well as in the so called galactic micro-quasars. Some examples known so far include SS 433 (Hjellming & Johnston 1981), Cygnus X-3 (Strom et al. 1989), Cir X-1 (Stewart et al. 1993), 1E 1740.7-2942 (Mirabel et al. 1992) and GRS 1915+105 (Rodríguez et al. 1992). The different morphologies shown by extended components in these sources include jet-like structures, surrounding nebulae, and also extended bow shocks. If these features are powered by the central accretion-driven X-ray source, their presence puts important constraints on the capability of compact objects to accelerate and collimate beams of relativistic particles, and to the total energy injected into the nearby interstellar medium.

Thus, observational and theoretical evidences have lead to the suggestion that extended radio emission in galactic X-ray sources, and specially radio jets, could

be a phenomenon much more common than previously expected (Rodríguez et al. 1992, Falcke & Biermann 1996). Up to now, such structures have not been often detected in the  $\sim 25$  REXRBs catalogued (Hjellming & Han 1995). However, it could be possible that this apparent absence was due to most interferometric radio observations being aimed to find sub-arcsecond details. Then, if the jet structures had a typical parsec linear size, as in the case of micro-quasars, they should appear with angular diameters in the arcminute range at typical distances of few kpc. For instance, at the 2.0 kpc distance of LS I+61°303 (Frail & Hjellming 1991), one parsec corresponds to  $\sim 2'$ . Consequently, any extended emission of this size would be heavily resolved out and undetected by high resolution interferometers.

Table 5.1 shows the list of REXRBs that have been observed with evidences of associated extended structure (Fender et al., 1997). We indicate in it whether such structures have been detected at “VLBI mapping scales”, “VLA mapping scales” or both.

Up to now LS I+61°303 has been mainly radio imaged at high interferometric resolving ranges (VLBI). The only published images at intermediate scales are the map by Gregory et al. (1979) in the arcsecond range but with low sensitivity, and the survey performed by Frail et al. (1987) at arcminute scales, although with a rather low image angular resolution. We present deep interferometric radio maps of LS I+61°303 with different resolutions of  $\sim 0''.5$  and  $\sim 15''$ . In addition, the extended radio emission on larger angular scales ( $\sim 0.5'$ ) is also briefly discussed by using the Dominion Radio Astronomical Observatory (DRAO) survey maps of the galactic plane (Normandeau et al. 1997). All this information together represents a noticeably improvement with respect to the only previous extended radio emission search around LS I+61°303 we just mentioned by Frail et al. (1987).

## 5.2 VLA observations

The VLA was acting as an interferometer element in the VLBI experiments on LS I+61°303 reported in Chapter 4 and in Massi et al. (1993). Since in addition to the phased array mode for VLBI experiments, the VLA can also provide simultaneously its normal interferometer output, we initiated this research through exploitation of the individual LS I+61°303 VLA data obtained during such runs. VLBI experiments normally cover a period of time of the order of hours over the



Table 5.1: REXRBs with associated radio structure detected.

Source	Extended (VLA, arrays)	Compact (VLBI, VLBA)	References
SS 433	$\sim 1''$	$\sim 20$ mas	Hjellming & Johnston (1981). Vermeulen et al. (1993)
GRS 1915+105	$\sim 1''$	--	Mirabel & Rodríguez (1994)
GR0 J1655-40	$\sim 2''$	$\sim 200$ mas	Tingay et al. (1995), Jones et al. (1997)
Cygnus X-3	$\sim 10''$	$\sim 30$ mas	Strom et al. (1989), Molnar et al. (1988), Schalinski et al. (1995). this work
Circinus X-1	$1'$	$\sim 15$ mas	Stewart et al. (1993), Preston et al. (1983)
LS I+61°303	Not detected	$\sim 3$ mas	This work
1E 1740.7-2942	$\sim 1'$	--	Mirabel et al. (1992)
GRS 1758-258	$\sim 1'$	--	Rodríguez et al. (1992)

-- No detections reported.

source, and in our case the VLA was active a large fraction of such period. That could provide a large number of visibilities to try to unveil weak structure at intermediate scales.

The observation dates and VLA configurations used are summarized in Table 5.2. All these observations were at 6 cm with an effective bandwidth of 50 MHz. Two primary amplitude calibrators were observed, namely, 1331+305 and 0137+331 for which 6 cm flux densities of 7.43 Jy and 5.50 Jy were adopted respectively. The phase calibrator observed was always 0228+673 and the flux densities adopted for it in each session are also listed in Table 5.2. The data were edited and calibrated using the Astronomical Image Processing System (AIPS) software package of NRAO.

As we have seen in the previous chapter, an important trouble that one can usually encounter when imaging with radio interferometers is the brightness variability of the

Table 5.2: Input parameters of LS I+61°303 VLA 6 cm observations

Date	VLA Configuration	0228+673 Bootstrapped Flux Density (Jy)
1990 June 6	A	$1.65 \pm 0.01$
1993 Sept 9	CnD	$2.74 \pm 0.01$
1993 Sept 13	CnD	$2.67 \pm 0.01$

source. Often, REXRBs might exhibit substantial variations within the several hours that a typical observing run may last. When this happens, it is not possible to use directly the standard CLEAN algorithm to compute maps, since the assumption of a constant brightness distribution is clearly violated. Therefore, not so straightforward approaches must be adopted in order to remove time variability effects.

The plots in Figure 5.1 show the details of the radio light curve for all VLA observing sessions in an expanded time scale. To have a better view of the stability degree of the data, the measurements are expressed through the percentage of the relative flux density with respect to the average of the absolute values measured in the corresponding session.

We can see in the figure that during the 1990 observation LS I+61°303 did not vary by more than  $\sim 5\%$  within a continuous time span of  $\sim 7$  h (60% of the total run). The source showed as well brightness stability within a  $\sim 5\%$  on the whole observing session of 1993 September 13. However, the situation was completely different two days before, on September 9, when the flux density of LS I+61°303 at 6 cm varied from 131 mJy to 76 mJy in about 7 h. (In chapter 9 we devote a section to the analysis of the variability of these radio light curves).

Since the data sets of September 1993 were taken when the VLA was in a hybrid but relatively compact CnD configuration, they are the more suitable to look for extended radio sources in the arcminute range. Whereas, since during the run of June 1990 the VLA was in its more expanded configuration this qualifies better to get images more tight around the central source. In the next two sections we analyze the results we got from both kind of images, and we sojourn in the method we used

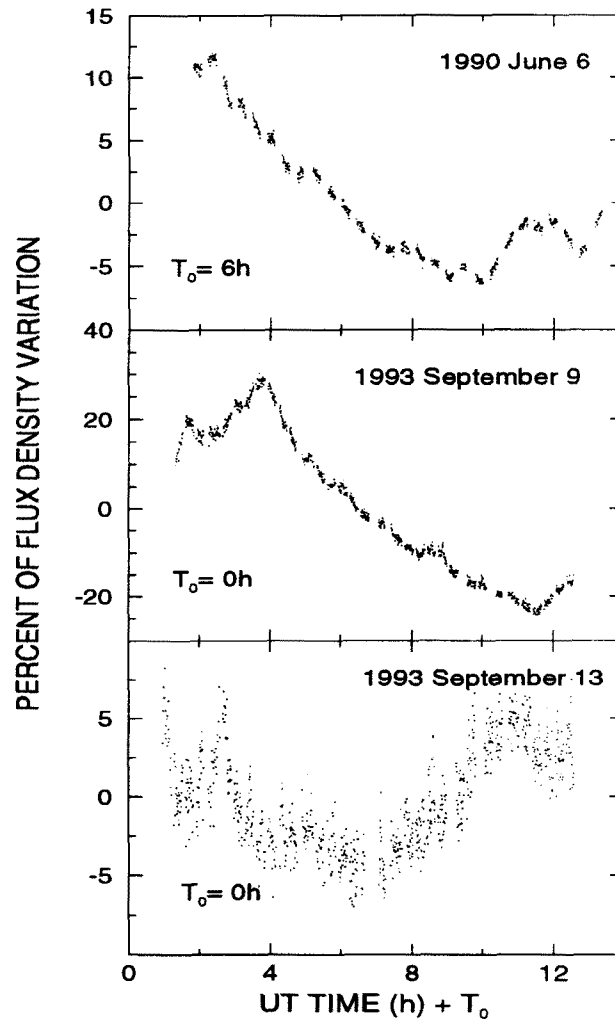


Figure 5.1: Percent of variation relative to the average flux density of LS I+61°303 as observed with the VLA. The time resolution is 30 seconds. From top to bottom, the average flux density measured for each observing session is 233 mJy, 101 mJy and 57 mJy, respectively.

to analyze the variable data from the second session.

### 5.3 Search for arcsecond extended radio emission around LS I+61°303

As we have mentioned the only VLA map of LS I+61°303 with arcsecond resolution so far published is that by Gregory et al. (1979), where the source appears to be unresolved ( $<0''.5$ ). These authors observed at 6 cm when the VLA was near

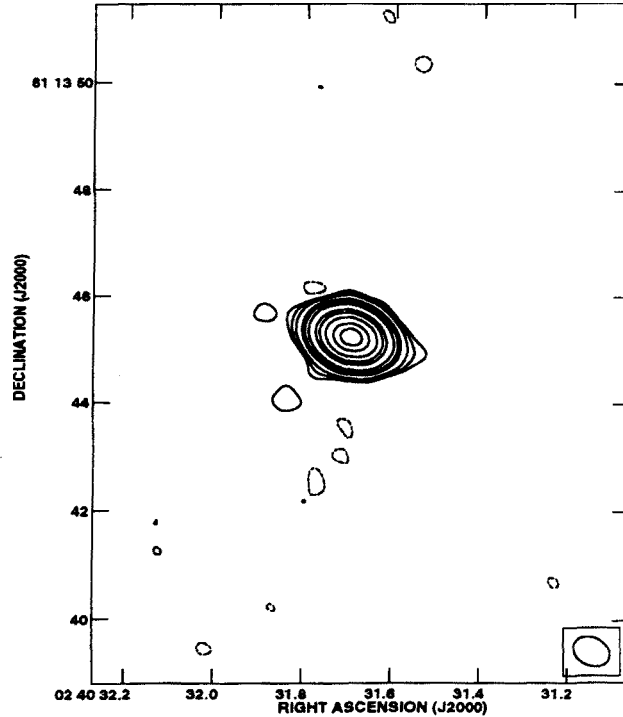


Figure 5.2: Natural weight high resolution map of LS I+61°303 from the VLA A configuration data of 1990 June 6. The synthesized beam (shown in the lower right corner) is  $0'.64 \times 0'.50$ , with position angle of  $56^\circ.1$ . Contours are  $-3, 3, 5, 10, 30, 50, 100, 300, 500, 1000, 2000$  and  $3000$  times  $0.059 \text{ mJy beam}^{-1}$ , the rms noise.

completion, using only eight antennas with a maximum baseline of 10 km.

We obtained a much better image of LS I+61°303 using visibilities taken only from the stable part of our VLA data of 1990 June 6, when the full array was operative and in its most extended A configuration. This image is shown in Figure 5.2. In this map LS I+61°303 also appears unresolved, with a smaller angular size upper limit of  $<0''.3$ . This is consistent of course with the  $\sim 1.6 \times 1.0 \text{ mas}$  size reported by Massi et al. (1993) during a simultaneous VLBI experiment as well as with the size of about 3 mas reported by Taylor et al. (1992) and about 2 to 6 mas reported by ourselves in Chapter 4. As we have seen in section 4.3.3 of that chapter, from comparison with the fluxes computed with the VLA and VLB arrays in simultaneous experiments, we can conclude that any emission extended at arcsecond scales, contributes only a few mJy to the total flux density. From our VLA map in A configuration, we are able to further constrain this statement to a  $4\sigma$  upper limit of  $0.9 \text{ mJy arcsec}^{-2}$  for possible arcsecond extended features existing *at the epoch of this observation*.

## 5.4 Search for arcminute extended 6 cm emission in the vicinity of LS I+61°303

### 5.4.1 Deep images performance

We disposed of two sessions observed in CnD configuration, being the first one (September 9, 1993) highly variable, preventing to perform an image directly. A quick analysis of the second session data (September 13) gave us a first rough version of a map where some faint structure was clearly showing up.

In order to obtain an image as deep as possible, we decided to make also use of the first session. Thus, to be able to proceed, it was necessary for us to check and minimize the effects of luminosity time dependence on the data. The method we used was, basically, to erase the point-like contribution of LS I+61°303 in the images deconvolved from data subsets of constant brightness.

The steps performed can be summarized as follows:

- To start, we self-calibrated in phase the data using as input model a single point source at the position of LS I+61°303 (central target) and with its average flux density. Since LS I+61°303 is the most prominent source in the area at this frequency, this was considered a reasonable first approximation. For the self-calibration we didn't use the amplitude information of the visibilities but the phase information.
- We divided the observation into 17 data blocks about 30 minutes long. During these intervals, the emission level of LS I+61°303 could be considered to stay safely constant.
- A map was computed and the LS I+61°303 flux density was determined for each block.
- From each  $uv$  data subset we subtracted a point source model with the corresponding flux density of LS I+61°303.
- During the subtraction process, we also removed the clean components of BG 0237+61. This is a relatively strong source situated approximately 15'

northeast of the phase center, being detected through the first primary beam sidelobes.

- Afterwards, we concatenated all the subsets together obtaining a single data file.
- Although the variability on 1993 September 13 was not severe, we also applied here the same division and subtraction procedure.
- Next step was to concatenate the variability free data sets of both 1993 September 9 and 13 in order to increase sensitivity.
- We performed the final map by means of the  $uv$  data set resulting from the previous step. In addition, during this process we took care of:
  - applying natural weight (i.e. such that stresses significance of short baselines) in order to increase sensitivity and to emphasize any possible extended emission present,
  - adding a constant point source at the LS I+61°303 position with the observing session average flux density level of 78 mJy in order to have a more accurate picture of the sky area mapped, and
  - including zero space flux density level parameter of 0.2 Jy from single dish maps.

In this way, the 6 cm map of Figure 5.3a could be finally produced. Figure 5.3b corresponds exactly to the same field as it appears in the optical from the digitized version of the Palomar Observatory Sky Survey (POSS).

## 5.4.2 Arcminute extended radio sources in the field of LS I+61°303

As it can be seen in the image from compact array configuration data, in Figure 5.3a, our main result here is that no significant emission closer than 1' to LS I+61°303 is detected. The map  $4\sigma$  upper limit is  $0.076 \text{ mJy beam}^{-1}$ , corresponding to a limiting surface brightness of about  $0.43 \mu\text{Jy arcsec}^{-2}$ . Nevertheless, several clumps of extended emission are certainly detected around LS I+61°303, at an angular separation between 2'-4'. We have labeled the most prominent of them as A, B, C

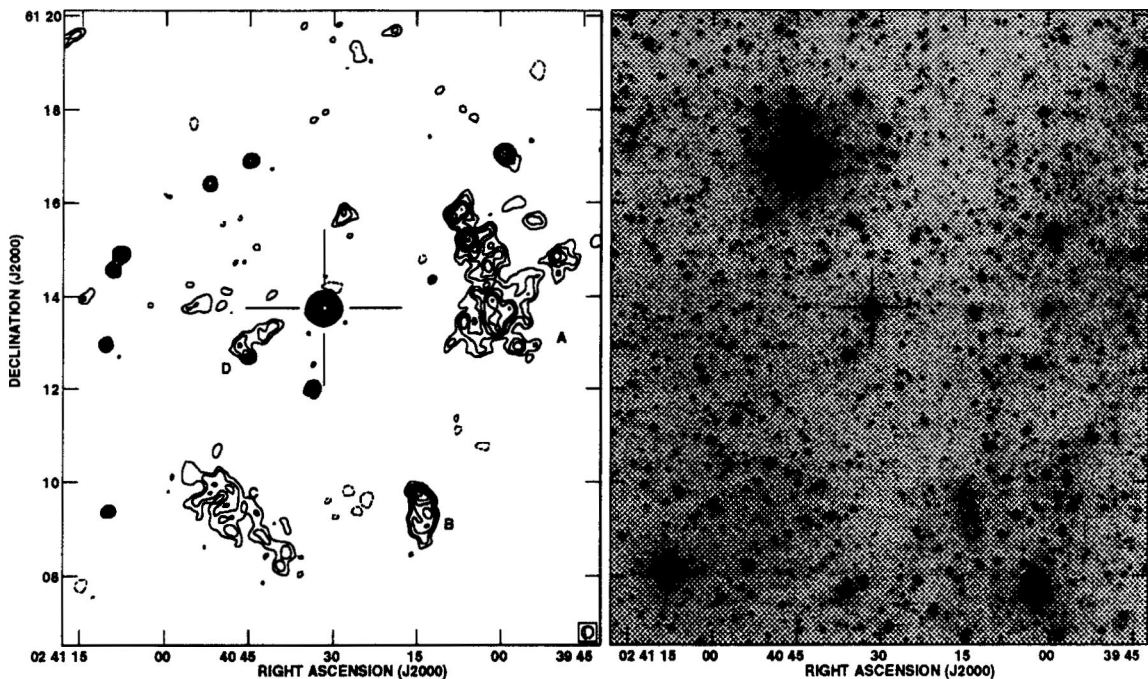


Figure 5.3: a) Combined map obtained by concatenating the runs of 1993 September 9 and 13 and using the procedure described in section 5.2. The synthesized beam is  $15'' \times 15''$ . Contours are  $-4, 4, 5, 6, 7, 8, 9, 10, 12, 15, 20, 50, 100, 200, 500, 1000, 2000, 4000$  and  $6000$  times  $19 \mu\text{Jy beam}^{-1}$ , the rms noise. b) The same field in the optical from the digitized version of the POSS.

and D, in order of increasing right ascension. Their observed parameters are given in Table 5.3. The flux densities in this table include the correction for primary beam response. The primary beam corrected map is quite noisy at the location of some of these extended features, but all of them are still clearly evident. The presence of A, B, C and D is also evident in the maps made using each 1993 September observing data set separately.

### 5.4.3 The nature of the extended radio sources detected

What is the physical nature of these VLA sources? Given their apparent circular clustering around LS I+61°303 one possible interpretation is that they are part of a supernova remnant (SNR). Up to now, there are only two cases known of association between a Be star and a SNR (Hughes & Smith, 1994), both in the Small Magellanic Cloud. However, several arguments conspire immediately against a SNR origin:

Table 5.3: Observational data for the extended sources in the vicinity of LS I+61°303

Source	$\alpha(\text{J2000})^a$	$\delta(\text{J2000})^a$	Angular Size	$S_{6\text{cm}}$ (mJy)
A	02 <sup>h</sup> 40 <sup>m</sup> 06 <sup>s</sup>	+61°15'2	3'2×1'1	15.6 ±0.5
B	02 <sup>h</sup> 40 <sup>m</sup> 15 <sup>s</sup>	+61°09'7	1'3×0'7	4.4 ±0.3
C	02 <sup>h</sup> 40 <sup>m</sup> 39 <sup>s</sup>	+61°08'2	3'3×1'2	13.4 ±0.6
D	02 <sup>h</sup> 40 <sup>m</sup> 45 <sup>s</sup>	+61°12'7	1'2×0'6	0.9 ±0.1

<sup>a</sup> The position given corresponds to the peak of radio emission.

- (i) The round shape centered on LS I+61°303 may be an illusion due to the decay of the primary beam sensitivity.
- (ii) Assuming a typical non-thermal index, a plot of the A, B, C and D surface brightness in the 1 GHz  $\Sigma, D$  diagrams of Green (1991), implies that a SNR two orders of magnitude more sub-luminous than average would be required.
- (iii) None of the extended radio sources in Figure 5.3a has any evident counterpart in the ROSAT X-ray image of the same field obtained by Goldoni & Mereghetti (1995), while SNRs are usually X-ray emitters.

The situation is more clear at optical wavelengths from a comparison of the map in Figure 5.3a with the original print of the corresponding POSS plate, reproduced in Figure 5.3b. The extended radio sources A and C seem to trace the outer limits of some optical nebulosity that is part of the nearby giant HII regions W4 and W5, respectively. Source B is also coincident with an optical nebula surrounding a group containing a few stars, which is probably a HII region as well. These coincidences suggest that A, B and C are likely to be thermal free-free radio sources.

Source D is also possibly of thermal origin, but we believe deserves some additional comments. It does not have any evident optical counterpart and its elongated appearance, pointing towards the LS I+61°303 position, does resemble a radio jet lobe. The separation between the photocenter of source D and LS I+61°303 is about 2' (equivalent to 1.2 pc if located at 2.0 kpc). This is in the same range as the radio jets of 1E 1740.7–2942 and GRS 1915+105. However, no opposite D counterpart is detected.



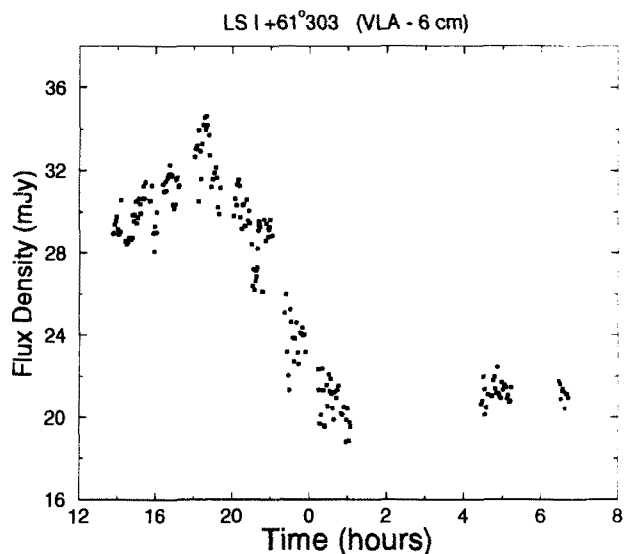


Figure 5.4: Flux variation of the 6 cm observation of LS I+61°303 with the VLA on 8/9 June 1992.

#### 5.4.4 Long temporal structural stability

The arcsecond extended emission associated to some of the galactic compact sources presented in the introduction of this chapter may show structural variations perceptible within about the order of 5 to 7 days (like 1E 1740.7–2942 with superluminal motions) to the order of a month or few months (like SS 433). The two sessions from where we obtained arcminute scale images of LS I+61°303 were separated only four days in time. Therefore, in order to check whether the detected extended weak emission surrounding LS I+61°303 presented any structural variations in larger time scales we decided to obtain a deep image from data taken far apart in time from the September 1993 runs.

For that matter, we made use of the VLA observations taken in June 1992 when the array was acting as one of the antennas of the VLBI experiment presented in section 4.3 of Chapter 4. Details of the observation, calibration and reduction procedures have been described in such section. We just stress here that these VLA data were taken at 6 cm and in the same hybrid CnD configuration as in September 1993. Therefore, they were suitable to compare the results of their deconvolution with the image obtained from the observations we have just presented.

In this occasion, the light curve of the source tracked by the VLA presented a variation of approximately 50% in about 12 hours as shown in Figure 5.4. Therefore, to remove the effects of time variability we decided to apply the same strategy as we

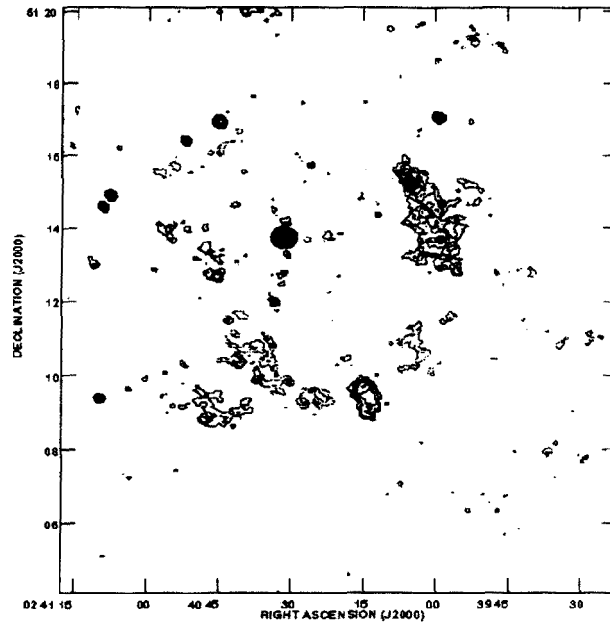


Figure 5.5: 6 cm radio map obtained from the June 1992 VLA data using the procedure described in Section 5.4.4. The synthesized beam is  $8''.5 \times 6''.5$  with a position angle of  $77.3^\circ 3$ . Contours are  $-5, -4, -3, 3, 4, 5, 6, 7, 8, 9, 10, 12, 15, 20, 50, 100, 200, 500, 1000$ , and  $1200$ , times  $20 \mu\text{Jy beam}^{-1}$  (rms noise).

did to the September 1993 runs: the data set was divided in 22 pieces of about 30 minutes each. For any individual one, a map was processed from where LS I+61°303 flux density and BG 0237+61 clean components were determined and removed. After linking all of them together the final map was computed. The obtained image is plotted in Figure 5.5. This is almost identical within the error levels and the reduction indeterminations to the map obtained with independent data and 14 months a part in time in the section described above.

In conclusion, the faint structure detected around LS I+61°303 does not show any significant variation in a lapse of time of about 1 year. This fact helps also to strongly suspect that such weak radio emission is not related to our target source. Perhaps the item labeled in Table 5.3 as D seems to have different morphologies in the two epochs. The comparison of D in the two maps can suggest that in June 1992 this structure is somehow disrupted while in September 1993 it has been (again) formed. Nonetheless, this could be a fake effect due to the noisier map obtained for the first epoch.

## 5.5 Spectral index analysis

In order to really test the true thermal nature of the A, B, C and D sources reported here, a good spectral index measurement should be necessary. This would require obtaining sensitive matching beam data at a different wavelength that is currently not available. However, we attempted to estimate spectral indices using the 20 cm (i.e. L band) VLA data obtained by Taylor et al. (1996) and analyzed in Chapter 3 (section 3.2) of the present work.

We remind the data were taken during 10 different observing sessions spanned in an orbital cycle in August/September 1992 simultaneously with 6 cm and X-ray data of the source (see Figure 3.1). In case we could obtain a sensitive enough image with these data to compare with the one we had at 6 cm, that would allow us to obtain an estimated map of the spectral behaviour between these frequencies of the zone mapped.

We followed a procedure similar as we presented in section 5.2, although in this case the runs had been in separated days each of them with a duration of about half an hour. From session to session the source presented strong brightness differences as it is characteristic of its radio luminosity periodic variability. In addition, we had to have into account the fact, at this band, that the source BG 0237+61 presented a flux density of about 300 mJy, therefore, it was much brighter than LS I+61°303. Therefore, we self-calibrated the sessions in phase using as input model a map with two sources: one at the center with the LS I+61°303 flux density for that session and the other at the position of BG 0237+61 and its flux. We couldn't make use of the session corresponding to the 10th day since the configuration of the VLA had changed from D to A. Maps for every one of the days were performed and the corresponding LS I+61°303 and BG 0237+61 clean components subtracted. The resulting uv-data were concatenated to obtain a single set of data, equivalent to a 4.5 hours run, where the variations of LS I+61°303 and BG 0237+61 had been minimized. Because of the introduction of a spurious periodic pattern by short baselines, robust weight was applied and  $uv$  distances shorter than 0.15  $k\lambda$  were edited out

The map obtained is displayed in Figure 5.6a (contour image). Structures newly detected at 6 cm also appear at 20 cm although the signal to noise achieved in this case is very poor and much smaller than the sensitivity of the maps at 6 cm.

The resolution of the image is also much worse at L band than at C band, which makes no possible the computation of an spectral map from them. Therefore, to achieve a similar resolution we proceeded to degradate the 6 cm image so the two beams of the maps matched reasonably well. For that matter we convolved the 6 cm map beam with a tapering function, such that the resulting beam was  $62'' \times 55''$ , with a position angle of  $-65^\circ$ , similar in area and axis orientation to the beam  $71'' \times 50''$ , and position angle of  $-63^\circ$  corresponding to the 20 cm image. The resulting 6 cm map is plotted in Figure 5.6b. The noise level for the degradated map at 6 cm is  $0.034 \text{ mJy} \times \text{beam}^{-1}$ , whereas at 20 cm the noise level is  $\sim 40$  times larger ( $1.4 \text{ mJy} \times \text{beam}^{-1}$ ). This fact makes impossible to know whether it may exist some 20 cm emission at comparable levels with the 6 cm one that we do not detect because of the noise.

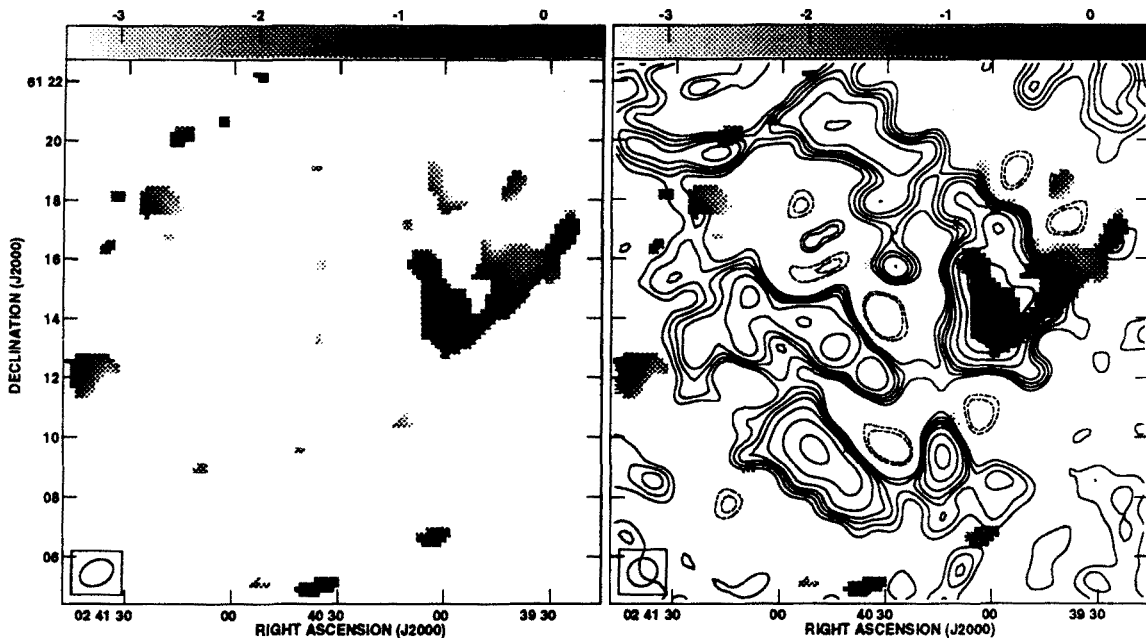


Figure 5.6: a) Contour map at 20 cm from the August/September 1992 monitoring campaign, using the procedure described in section 5.5. The primary beam is  $71'' \times 50''$ . Contours are  $-3, -2, 2, 3, 4, 5, 6, 8, 12, 18, 26, 36$  times  $1.4 \text{ mJy} \times \text{beam}^{-1}$ , the rms noise. b) Contour map at 6 cm from the same data as the image in Figure 5.3a with the beam degradated to a similar size as the map in a). Contours are  $-4, -3, 3, 4, 5, 6, 8, 12, 18, 26, 36$  times  $0.034 \text{ mJy} \times \text{beam}^{-1}$ , the rms noise. The grey scale spectral map computed from the two images is superposed to both contour maps in a) and b).

Although because of the poor sensitivity of the 20 cm image an spectral index map has no meaning, for instructive purposes we have marked over the contours of

the two images, using a grey scale, the result of spectral index measurement in the common detected areas. We think only the peak of radio source A in Figure 5.3 shows a significantly non-thermal spectral index, suggesting that this compact feature may be a background extragalactic object.

## 5.6 Other compact radio sources in the LS I+61°303 vicinity

Several more compact radio sources are also evident in the maps of Figures 5.3a and 5.5. Their positions and 6 cm flux densities are listed in Table 5.4. In addition to LS I+61°303, source number 5 is the only one clearly having a stellar optical counterpart. Its radio position is coincident within  $0''.7$  with that of SAO 12383. This is a O9.5I star, also catalogued as V482 Cas, which was detected as an X-ray source by Goldoni & Mereghetti (1995) and no detection at radiowavelengths of this source has been reported before the publication of our map. In these kind of sources both the X-ray and radio emission are likely to be originated in its stellar wind. Using the formulation of Felli & Panagia (1981) for free-free emitting envelopes, the observed flux density of SAO 12383 implies a stellar wind mass loss of  $5 \times 10^{-6} M_{\odot} \text{ yr}^{-1}$  assuming a wind velocity of  $10^3 \text{ km s}^{-1}$ .

Source 2 is also coincident within  $2''$  with an anonymous POSS object. However, its appearance in the POSS plates is not fully star-like, suggesting that it is a background extragalactic object. Possibly, the same statement applies to the rest of sources in Table 5.4. A search in several star catalogues and the POSS plates yielded negative results for all of them. The extragalactic origin interpretation can be additionally justified from source count analysis (Condon, 1984). Using the formulation of Rodríguez et al. (1989), the number of background extragalactic sources with  $0.1 \text{ mJy} \leq S_{6\text{cm}} \leq 100 \text{ mJy}$  expected in a 6 cm VLA primary beam is  $\sim 8$ . This is fully consistent with the 8 radio sources in Table 5.4 without stellar optical counterpart identified.

Table 5.4: Compact radio sources in the vicinity of LS I+61°303

Source	$\alpha$ (J2000)	$\delta$ (J2000)	$S_{6\text{cm}}$ (mJy)
1	02 <sup>h</sup> 39 <sup>m</sup> 59 <sup>s</sup> .50	+61°17'03".1	1.23 ±0.03
2 <sup>a</sup>	02 <sup>h</sup> 40 <sup>m</sup> 12 <sup>s</sup> .09	+61°14'22".7	0.09 ±0.02
3 <sup>b</sup>	02 <sup>h</sup> 40 <sup>m</sup> 31 <sup>s</sup> .67	+61°13'45".6	variable
4	02 <sup>h</sup> 40 <sup>m</sup> 33 <sup>s</sup> .69	+61°12'02".5	0.23 ±0.03
5 <sup>c</sup>	02 <sup>h</sup> 40 <sup>m</sup> 44 <sup>s</sup> .95	+61°16'55".7	0.33 ±0.03
6	02 <sup>h</sup> 40 <sup>m</sup> 52 <sup>s</sup> .23	+61°16'26".2	0.30 ±0.03
7	02 <sup>h</sup> 41 <sup>m</sup> 07 <sup>s</sup> .76	+61°14'54".2	0.51 ±0.04
8	02 <sup>h</sup> 41 <sup>m</sup> 09 <sup>s</sup> .38	+61°14'34".4	0.35 ±0.04
9	02 <sup>h</sup> 41 <sup>m</sup> 09 <sup>s</sup> .89	+61°09'23".0	0.68 ±0.04
10	02 <sup>h</sup> 41 <sup>m</sup> 10 <sup>s</sup> .71	+61°12'58".5	0.32 ±0.04

Optical identifications: <sup>a</sup> POSS object, <sup>b</sup> LS I+61°303, <sup>c</sup> SAO 12383.

## 5.7 Extended radio emission from independent low resolution data

The previous deepest search for extended radio emission in LS I+61°303 was that of Frail et al. (1987) at 408 and 1420 MHz. Their resolution was between 1'-3' and they found that LS I+61°303 is actually surrounded by a 47' × 27' extended emission feature (EEF), with an integrated flux density of  $\sim 10$  Jy at both frequencies. The uncertainty in their spectral index determination did not allow to discriminate between a thermal or non-thermal emission mechanism. They concluded that the most likely interpretations of the EEF are either thermal emission from nearby HII complexes or a non-thermal surrounding nebula similar to that of Cir X-1. However, in contrast with the case of Cir X-1, the EEF in the maps of Frail et al. (1987) did not exhibit any clear structure or evidences of collimation.

Since the largest scale structure visible in our VLA data is  $\sim 5'$ , these observations alone do not allow us to address the Frail et al. (1987) EEF issue. This feature, however, can be better studied by using the DRAO data from Normandeau et al. (1997). A sub-image of this modern survey is shown in the map of Figure 5.7 of an area of about  $1.5^\circ \times 2^\circ$  centered around LS I+61°303. Here, the EEF feature

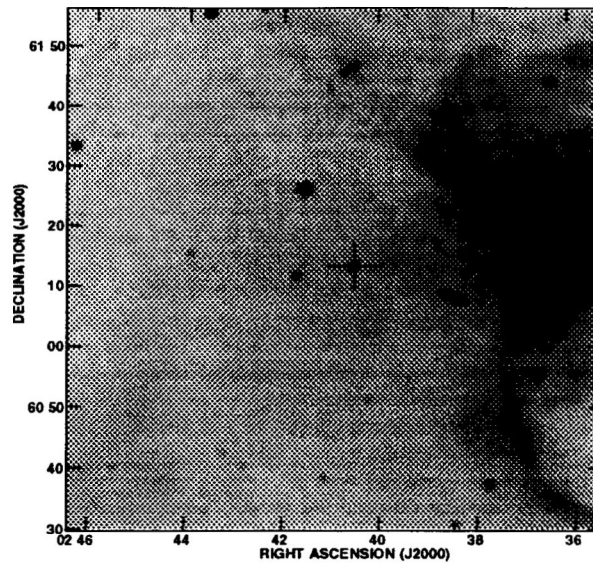


Figure 5.7: Radio map of the LS I+61°303 region at 6 cm wavelength from the survey data of Normandeau et al. (1997). The central cross indicates the position of LS I+61°303. The brightest emission on the right corresponds to filamentary loop structures of the W4 giant HII region.

appears to consist of a region with steady negative gradient in brightness towards the SE direction. The DRAO image also clearly suggests that the EEF might be part of filaments belonging to the giant HII complex W4 (Wendker & Altenhoff 1977). Furthermore, on arcminute scales, there is no indication in Figure 5.7 of special enhancement, clustering or shell-like morphology around LS I+61°303. All these facts together provide further support to our previous statement that the extended emission detected with the VLA is likely to be of free-free thermal emission nature.

## 5.8 Conclusions

The analysis of several VLA monitoring sessions has revealed several clumps of extended radio emission within a few arcminutes from the REXRB LS I+61°303. Among this extended sources only the one labeled as D in Figure 5.3 could be associated to it. The association is however doubtful, but the data available up to now do not allow us to completely reject such hypothesis. The most likely interpretation is that all these structures correspond to free-free radio sources mainly associated to nearby HII regions. This implies that no extended or jet-like radio features, in the arcminute range, are present around LS I+61°303 up to a surface brightness limit of

$0.43 \mu\text{Jy arcsec}^{-2}$ . From VLA data in A configuration, a similar upper limit of  $0.9 \text{ mJy arcsec}^{-2}$  has been obtained for extended radio structures at arcsecond angular scales.

The apparent lack of extended radio structures in LS I+61°303 could have two quite different explanations. First, jets and extended radio emission do exist in LS I+61°303, but they are below our current sensitivity or extending at angular scales not yet explored. Or, second, the outburst mechanism of LS I+61°303 is such that radio emission is restricted close to the binary system and ejection of radio emitting electrons well outside the orbital volume is not relevant. Obtaining very sensitive maps with resolution intermediate between that of VLA and VLBI (e.g. MERLIN) would help to further test the first option. In fact, VLBI observations of LS I+61°303 (Chapter 4) have often suggested that 10-20% of the total flux density is not contained in milli-arcsec structures. It is therefore conceivable that this missing flux density could be lying at the yet unexplored  $\lesssim 0.1$  scales.

As a by-product of our observations, we have also detected up to 9 previously unknown weak compact radio sources in the field of LS I+61°303, with 6 cm flux densities between 0.2-1.2 mJy. One of them appears to be the radio counterpart of the early type star SAO 12383, while the others are most likely to be extragalactic objects.



# Bibliografy

- [1] Condon J.J., 1984, ApJ 287, 461
- [2] Falcke H. & Biermann P.L., 1996 A&A 308, 321
- [3] Felli M., Panagia N., 1981, A&A 102, 424
- [4] Fender et al., 1997, *Proced. IAU Colloq.* 164
- [5] Frail D.A., Seaquist E.R., Taylor, A.R., 1987, AJ 93, 1506
- [6] Frail D.A., Hjellming R.M., 1991, AJ 101, 2126
- [7] Goldoni P., Mereghetti S., 1995, A&A 299, 751
- [8] Green D.A., 1991, PASP 103, 209
- [9] Gregory P.C., Taylor A.R., Crampton D., Hutchings J.B., Hjellming R.M., et al., 1979, AJ 84, 1030
- [10] Hjellming R.M., Johnston K.J., 1981, ApJ 246, L141
- [11] Hjellming R.M., Han X., 1995, in *X-Ray Binaries*, Cambridge Astrophysics Series, 26, 308, W.H.G. Lewin, van Paradijs J. & van den Heuvel E.P.J. Eds.
- [12] Hughes J.P., Smith R.C., 1994, AJ 107, 1363
- [13] Jones D.L., Tingay S.J., Jauncey D.L., Preston R.A., Reynolds J.E., Meier D.L., Murphyl D.W., Tzioumis A.K., McKay D.J., Kesteven M.J., Lovell J.E.J., Campbell-Wilson D., Ellingsen S.P., Gough R., Hunstead R.W., McCulloch P.M., Migenes V., Quick J., Sinclair M.W., Smits D., 1997, *Vistas in Astronomy*, 41, No. 1, 27
- [14] Massi M., Paredes J.M., Estalella R., Felli M., 1993, A&A 269, 249

- [15] Mirabel I.F., Rodríguez L.F., Cordier B., Paul J., Lebrun F., 1992, *Nat* 358, 215
- [16] Mirabel I.F., Rodríguez L.F., 1994, *Nat* 371, 46
- [17] Molnar L.A., Reid M.J., Grindlay J.E., 1988, *ApJ* 331, 494
- [18] Normandeau M., Taylor A.R., Dewdney P.E., 1997, *ApJSS* 108, 279
- [19] Preston R.A., Morabito D.D., Wehrel A.E., Jauncey D.L., Batty M.J., Haynes R.F., Wright A.E., Nicolson G.D., 1983, *ApJ* 268, L23
- [20] Rodríguez L.F., Myers P.C., Cruz-González, I., Terebey, S., 1989, *ApJ* 347, 461
- [21] Rodríguez L.F., Mirabel I.F., Martí J., 1992, *ApJ* 401, L15
- [22] Schalinski C.J., Johnston K.J., Witzel A., et al., 1995, *ApJ* 447, 1995
- [23] Stewart R.T., Caswell J.L., Haynes R.F., Nelson G.J., 1993, *MNRAS* 261, 593
- [24] Strom R.G., van Paradijs J., van der Klis M., 1989, *Nat* 337, 234
- [25] Taylor A.R., Young G., Peracaula M., Kenny H.T., Gregory P.C., 1996, *A&A* 305, 817
- [26] Taylor A.R., Kenny H.T., Spencer R.E., Tzioumis A., 1992, *ApJ* 395, 268
- [27] Tingay S.J., Jauncey D.L., Preston R.A., Reynolds J.E. et al., 1984, *Nature* 374, 141
- [28] Vermeulen et al., 1993, *A&A* 270, 177
- [29] Wendker H.J., Altenhoff W.J., 1977, *A&A* 54, 301

# Chapter 6

## Extended emission in Cygnus X-3

### 6.1 Introduction

#### 6.1.1 Cygnus X-3 sub-arcsecond radio emission

The radio counterpart of Cygnus X-3 has been widely observed at sub-arcsecond scales through both VLBI, VLBA<sup>a</sup> and MERLIN<sup>b</sup> experiments, essentially after strong intensity outburst events. All these observations coincide in reporting the detection of a source expanding in the North-South direction with inferred velocities of about  $0.3c$  (Geldzahler et al., 1983, Spencer et al., 1986, and Schalinski et al. 1995) and about  $0.16c$ – $0.31c$  (Molnar et al. 1988). However, it has been difficult to obtain clear images of its radio morphology, and the reported speed results are mainly based on the lapse of time that takes to the source to become resolved after it has undergone through a major flare event or series of them. Double sided jets have been predicted through visibility fitting models by Molnar et al. (1988). On the other hand, Schalinski et al. (1995) obtained the best representation of their visibility data with a three component model: a central core and two opposite weaker components with a separation of about 30 mas each away from the center and an alignment axis of about  $30^\circ$  from North to East. Due to the weak flux density that the source shows in its quiescent state, the high resolution observations have tended to be scheduled after outbursts episodes, and most attempts to image the source in quiescence have

---

<sup>a</sup>Very Long Baseline Array of NRAO

<sup>b</sup>Multi-Element Radio Linked Interferometer Network, University of Manchester

not been reported to be successful just until very recently, in coincidence with the composition of this memoir. The Cygnus X-3 quiescent state observations were taken at 2 cm with VLBA by Newell et al. (1997). During the integration time the source also experienced two of its characteristic mini-flares. The authors reported both contractions and expansions at apparent superluminal velocities of the very inner radio-source core.

It is not yet known whether the expanding components detected during the past years are plasmons associated to the development of a strong outburst or are part of a continuous jet, although theoretical models seem to support the collimated jet interpretation. For example, the Cygnus X-3 giant radio flare detected in September 1972 and monitored over a wide range of frequencies has been well modeled assuming continuous particle injection into a twin jet geometry at the early stages of the flare onset (Martí et al. 1992).

### 6.1.2 Cygnus X-3 arcsecond radio emission

Concerning *larger angular scales of the field around Cygnus X-3*, up to very recently, the only published map was that by Strom et al. (1989) with resolutions of few arcseconds, performed at 6 cm wavelength by the Westerbork Synthesis Telescope. The authors report the discovery of a weak double radio-source of about 4.5 mJy, symmetrically distributed with respect to the compact radio core of Cygnus X-3. Their map is reproduced in Figure 6.1. The total size of this large structure is estimated to be  $\sim 6$  arcseconds (corresponding to 0.35 pc at the Cygnus X-3 distance). An interesting result of this image is that the double structure elongation is approximately aligned in the North-South direction with an opening angle of the components with respect to the core of  $\sim 75^\circ$ . The fact that the position angle of the lobes is roughly aligned with the elongated sub-arcsecond morphology observed in the central core indicates that very probably this extended weak radio source is associated with the REXRB Cygnus X-3. If that is the case, a plausible explanation for the existence of the lobes could be that they are driven by the accumulated energetic particles produced during flaring episodes in the core. Although Cygnus X-3 has been monitored with arcsecond resolving instruments before and after Strom et al. discovery, their observations have been the only ones reporting a positive detection of extended emission for a long time. Therefore, such Cygnus X-3 extended features remain still very poorly studied. This is very likely due mostly to the masking effects

produced by the strength and variability of the central core together with the low surface brightness of the extended emission. Nonetheless, it could be possible as well that these outer lobes are not permanent features, being many times arduous to detect. Variations of extended lobes associated to REXRBs have been previously reported for other sources (e.g., 1E 1740.7-2942, Mirabel et al. 1992).

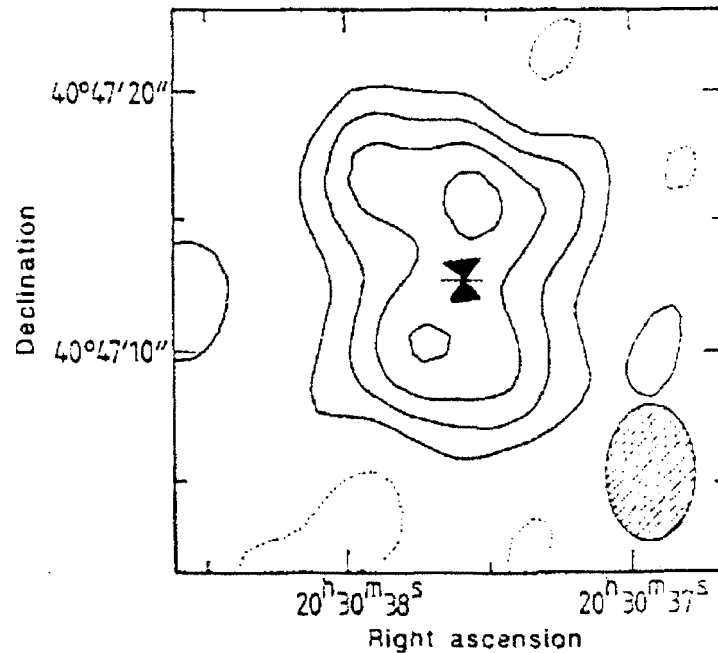


Figure 6.1: Map of the extended radio emission of Cygnus X-3 according to Strom et al. (1989). Contours levels are -0.21, 0.21, 0.42, 0.63, and 0.84 mJy per beam. The central core has been removed and the synthesized beam is  $3.5 \times 5.3$  arcseconds.

### 6.1.3 Objectives

From the facts quoted above, it is clear that the connection of possible lobes with sub-arcsecond structures deserves further attention. For instance, the VLBI observations of Molnar et al. (1988) during low level flares are consistent with milli-arcsecond jets, expanding at  $0.25c$  and with a wide opening angle of  $\sim 80^\circ$ . On the contrary, a VLBI observation after one major flare in 1986 seems to indicate better collimated structures, with position angle close to the North-South direction (Hjellming, 1988).

Having considered all these issues, we carried out a deep 3.5 cm Very Large Array B configuration observation of Cygnus X-3 aimed to study its associated extended radio emission. Our idea was that a successful detection of the extended lobe, or even of some part of it, with improved arcsecond resolution would certainly help to better understand the core-lobe connection. In particular, we think it is important to look for evidence indicating if the breadth of the Cygnus X-3 radio lobes is caused by an intrinsically broad beam or, alternatively, by a narrower beam that changes often its direction, as observed in SS433. Based on the model of Martí et al. (1992), the broad beam alternative should be preferred. In this context, the example of the REXRB Circinus X-1 has been very instructive. At low resolution, its radio core was found to be surrounded by a non-thermal parsec scale radio nebula (Haynes et al., 1986). However, when observed with sufficiently high resolution (Stewart et al., 1993), the Circinus X-1 radio nebula turned out to consist of collimated radio jets, ejected from the central core and curved because of the source transverse motion. So, it would not be surprising if the observations revealed evidences of arcsecond jet-like morphology in Cygnus X-3, although perhaps not so well collimated.

## 6.2 VLA observations and results

The Cygnus X-3 observations were carried out in 1995 November 6 with the VLA at frequency of 8.4 GHz in B configuration. Calibration and data editing was performed using also the AIPS package of NRAO. As it can be seen in Figure 6.2 the flux density of Cygnus X-3 changed from 220 mJy to 170 mJy along the 6.5 h of observation.

The mapping process was done after phase self calibrating and removing the source variability, by subtraction of a point source model with the Cygnus X-3 flux density as a function of time. Afterwards, a constant point source with the average flux density was added. The resulting synthesized map is shown in Figure 6.3, where one can see a marginal detection of *arcsecond radio jets* with position angle of  $\sim 35^\circ$ .

## 6.3 Discussion

Although the detection in Figure 6.3 is not beyond doubt ( $\sim 4\sigma$  level), it is remarkable that the position angle ( $\sim 35^\circ$ ) of the apparent radio jets is quite close to that

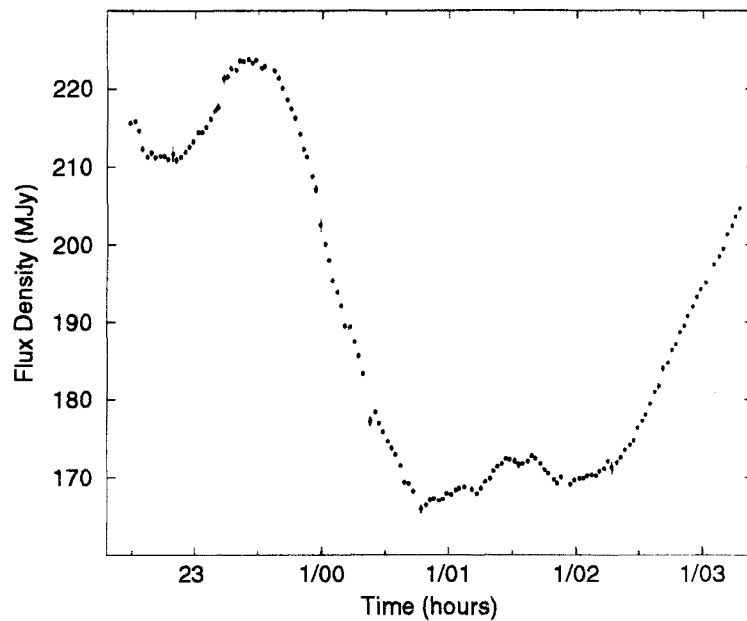


Figure 6.2: Flux density variations of Cygnus X-3 at 8.4 GHz during the 6 hours run on November 6 1995.

of the elongated structures seen in the recent VLBI model maps by Schalinski et al. (1995) (shown in Figure 6.4). Furthermore, it is striking that this position angle is also almost the same as seen in the nearly contemporaneously MERLIN map by Newell et al. (1997) that shows clear sub-arcsecond extended components. Such coincidences give strong support the reality of our marginal detection, suggesting that both the arcsecond ‘radio jets’ of our map and the Strom et al. (1989) map double radio source may be a direct manifestation of accumulated energetic particles produced by the continuous bursting activity in the central object. The opening angle of  $\sim 10^\circ$  roughly estimated from Figure 6.3 would indicate that the breadth of the Cygnus X-3 radio lobes is not caused by an intrinsically broad beam. Instead, the alternative should be a narrower beam that changes often its direction, as observed in SS433, although this is difficult to reconcile with the relatively narrow range of position angles seen in VLBI and MERLIN elongated features.

In any case, it is clear that all these interesting issues should be addressed only after a *reliable confirmation of the arcsecond radio jets* is obtained and with a much higher SNR. This fact motivated us to apply for observation time of the field around Cygnus X-3 with the Very Large Array in different conditions than the observations presented here. By using the information on peak flux density and jet angular scale provided by the map in Figure 6.3, we were now in a position to select the most suitable frequency and VLA configuration to do it. In our 3.5 cm map of Cygnus X-

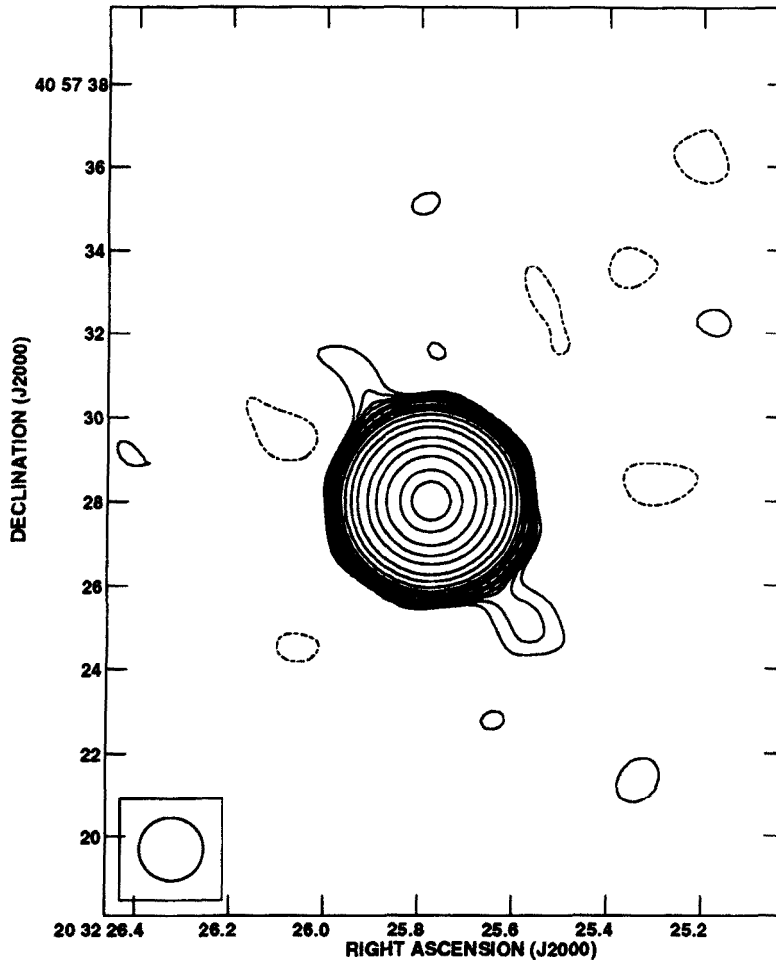


Figure 6.3: VLA map of Cygnus X-3 at a 3.5 cm wavelength in B configuration. The position angle of the marginally detected elongated emission seen is  $\sim 35^\circ$ . Contours are  $-3, 3, 4, 5, 6, 8, 10, 15, 20, 30, 50, 100, 200, 500, 1000, 2000, 4000$  and  $6000$  times  $0.026 \text{ mJy beam}^{-1}$ , the rms noise in the map. The synthesized beam is  $1''.54 \times 1''.51$  with position angle  $66^\circ$ , corresponding to natural weight with a taper of  $120 \text{ k}\lambda$ .

3, the radio jets are at a level of  $\sim 0.1 \text{ mJy beam}^{-1}$ , with the HPBW being  $1.5''$  because of strong tapering required to emphasize them. Assuming that the emission mechanism is synchrotron radiation, the detection could be very much improved by observing at a lower frequency with similar angular resolution. We thought a reasonable choice could be the 6 cm wavelength in B configuration of the VLA. This provides a comparable HPBW of  $1.8''$  for a naturally weighted map. For a typical non-thermal spectral index of  $-0.7$ , a 6 cm peak flux density of  $\sim 0.2 \text{ mJy beam}^{-1}$  is expected in the jets. Of course we are implicitly assuming here that the arcsecond jets are, at least, a year lasting or perhaps permanent features. This assumption seems reasonable considering the arcsecond angular scales involved. At the 10 kpc



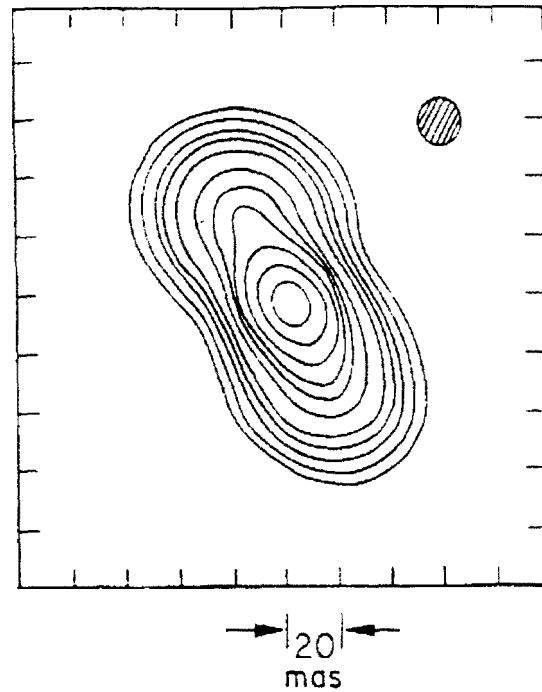


Figure 6.4: Model fit by Schalinski et. al (1995) of the 6 cm VLBI observations of Cygnus X-3 performed on 15/16 October 1985 during a strong outburst decay.

distance of Cygnus X-3 and for typical velocities of  $\sim 0.3c$ , the dynamical time scale is of the order of few years. The proposal to observe the source with the VLA, configuration B, at 6 cm was accepted and the observations were carried out on May 4th 1997, during the very final stages of the writing process of this document. Therefore results will have to wait to be reported elsewhere as a continuation of this work.



# Bibliografy

- [1] Geldzahler B.J., Johnston K.J., Spencer J.H., Klepczynski W.J., Jostres F.J., et al., 1983, ApJ 273, L65
- [2] Haynes R.F., Komessaroff M.M., Little A.G., et al., 1986. Nat 324, 233
- [3] Hjellming R.M., 1988, in *Galactic and Extragalactic Radio Astronomy*, Eds. Verschuur & Kellermann, Springer Verlag, 381
- [4] Martí J., Paredes J.M., Estalella R., 1992, A&A 258, 309
- [5] Mirabel I.F., Rodríguez L.F., Cordier B., Paul J., Lebrun F., 1992, Nat, 358, 215
- [6] Molnar L.A., Reid M.J., Grindlay, J.E., 1988, ApJ 331, 494
- [7] Newel S.J., Spencer R.E., Garret M.A., 1977, Vistas in Astronomy 41. 57
- [8] Schalinski C.J., et al., 1995, ApJ 447, 752
- [9] Spencer R.E., et al., 1986, ApJ 309, 694
- [10] Strom, R.G., van Paradijs, J., & van der Klis, M., 1989, Nat 337, 234
- [11] Stewart R.T., Caswell, J.L., Haynes R.F., Nelson, G.J., 1993, MNRAS 261. 593

